Development and Characterization of Stable Low-cost Salt Hydrate-based Phase Change Materials for Thermal Energy Storage Applications

A Dissertation Presented for the
Doctor of Philosophy
Degree
The University of Tennessee, Knoxville

Damilola Olayinka Akamo
May 2023

DEDICATION

This dissertation is dedicated –

To the glory of God,
the source of life and wellspring of wisdom.

To my best friend and wife,
Oromidayo Racheal Tunji-Ajayi,
for her never-ending prayers and emotional support.

In loving memory of my grandmother,
Olubunmi Cecilia Agbebiyi,
who inspired and supported my interest in life.

To my beloved mother,
Olawunmi Omotunde Akamo,
for strong and unwavering support through life's journey.

ACKNOWLEDGEMENTS

I would like to thank my advisors and mentors, Dr. Kyle R. Gluesenkamp, Dr. David Keffer and Dr. Orlando Rios for their guidance, and support. I would also want to extend my gratitude to the members of my dissertation committee, Dr. Katharine Page, and Dr. David Harper, without whom this work would not have been possible.

By providing me with funding for this research and my education, I am very appreciative to the Oak Ridge National Laboratory (ORNL) Building Technologies Research and Integration Center and the U.S. Department of Energy's Building Technologies Office. Also, I had the opportunity to work at ORNL and accomplish much due to the support of several talented people including Dr. Navin Kumar, Dr. Yuzhan Li, Dr. Tim J. LaClair, Dr. Kai Li, Dr. Monojoy Goswami, Dr. Samuel Graham, Dr. Xiaobing Liu, Dr. Jason Hirschey, Dr. Tugba Turnaoglu, Dr. Vera Bocharova, Dr. Lingshi Wang, Sara Sultan, among others.

The University of Tennessee Knoxville's Bredesen Center for Interdisciplinary Research and Graduate Education and Institute for Advanced Materials & Manufacturing are also acknowledged for their support, contributions, and provision of research facilities. My gratitude also goes out to my colleagues at University of Tennessee: Dr. Nitish Bibhanshu, Dr. Dayton Kizzire, Dr. Lu Yu, Dr. Na Gong, Dr. Haneul Jang, Dr. Hyojin Park, Dr. Zach Sims, Max Neveau, Collin Pekol, Michael Thompson, Emma Counce, Reece Emery, and John Rayle. Special thanks to Dr. Akinola Oyedele, Dr. Oluwafemi Oyedeji, Dr. Quan Vuong, and Dr. Valerie Garcia-Negron for their immense, support, advice, and encouragement throughout my doctoral program.

The support of my friends and family means the world to me. I found solace and motivation in my daily discussion and interactions with them. Also, I would like to thank all my collaborators for their help and fruitful research communications. I am indeed grateful for the beautiful experiences and notable accomplishments during my doctoral program.

ABSTRACT

Energy storage technologies are gaining attention due to rising utilization of renewable energy sources. One of the viable energy storage technologies is thermal energy storage (TES) in which system stores and releases thermal energy for various uses. Applications for TES systems include building systems, space heating and cooling, and refrigeration. Several TES systems use phase change materials (PCMs) to operate near-isothermally owing to phase change latent heat. Inorganic salt hydrate PCMs are popular because to their inexpensive cost, high energy density, and near ambient phase transition temperature. However, salt hydrate PCMs have phase separation, low thermal conductivity, and supercooling issues that reduce their long-term energy storage capacity and reliability. This work explores the synthesis, characterization, and property enhancement mechanisms of low-cost salt hydrate PCMs using various additives. Using empirical approach, dextran sulfate sodium (DSS) polyelectrolyte was found to stabilize sodium sulfate decahydrate (SSD) over repeated thermal cycles, compared to other additives. Atomistic simulation was used to unravel the stabilization mechanism at the molecular level. Findings show that there is an electrostatic interaction between SSD and the DSS polyelectrolyte which keeps the salt hydrate in domains that prevent phase separation, ultimately leading to improved thermal stability. The low thermal conductivity of salt hydrates has limited their practical application in TES. This work explored the enhancement of the properties of calcium chloride hexahydrate PCM using strontium chloride hexahydrate, graphene nanoplatelets (GNP) and cellulose nanofiber (CNF). Findings showed the amphiphilicity of CNF aids the dispersion of GNP thereby forming a compact PCM composite with improved thermal conductivity and thermal cycling stability. Salt hydrate PCMs are also attractive for near-ambient TES applications due to their suitable phase change temperature. This work further explored the synthesis and development of salt hydrate based eutectic PCMs with high heat storage capability and favorable phase change temperature for potential applications in near-ambient TES. Overall, this work provides promising methods to improve the properties and performance of salt hydrate PCMs by utilizing polyelectrolytes and bio-based nanocellulose, and eutectic approach for thermal energy storage applications.

TABLE OF CONTENTS

CHAPTER 1 INTRODUCTION AND LITERATURE REVIEW 1

1.1 Classification of LHS Systems 4

1.2 Salt hydrates Phase Change Materials 6

1.2.1 Mechanism of phase change in salt hydrate PCMs 7

1.2.2 Selection criteria and applications of salt hydrate PCMs 11

1.2.3 Technical Challenges and opportunities with PCMs 14

1.3 Research Problem and Research Question 17

1.4 Research aims and Objectives. 18

1.5 U.S. Department of Energy (DOE) thermal energy Storage program targets 18

1.6 Research scope 21

1.7 Organization of the thesis 21

CHAPTER 2 EMPIRICAL APPROACH TO STABILIZE LOW-COST SALT HYDRATE PHASE CHANGE MATERIALS USING POLYELECTROLYTE ADDITIVES 23

2.1 Introduction 25

2.2 Materials and Methods 27

2.2.1 Sample Synthesis 27

2.2.2 Characterization 28

2.3 Results and Discussions 30

2.3.1 Phase stability of the modified PCMs 30

2.3.2 Structural properties of the modified PCMs 32

2.3.3 Rheological properties of the modified PCMs 35

2.3.4 Thermal properties of the modified PCMs 44
2.4 Summary 51
CHAPTER 3 IDENTIFICATION OF STABILIZATION MECHANISMS IN SALT HYDRATE SYSTEMS BY DEXTRAN SULFATE SODIUM POLYELECTROLYTE..... 53
3.1 Introduction 55
3.2 Methods 58
3.2.1 Experimental setup 58
3.2.2 Molecular dynamics simulation set up and force field. 59
3.3 Results and Discussions 60
3.3.1 Thermal and structural properties of SSD and SSD-DSS obtained from experiment 60
3.3.2 Atomic structure of SSD from MD simulation 64
3.3.3 Role of Dextran sulfate sodium 67
3.3.4 Interfacial thickness and mobility characterization 70
3.3.5 Energetics. 73
3.4 Summary 76
CHAPTER 4 PERFORMANCE ENHANCEMENT METHODS FOR LOW-COST SALT HYDRATE PHASE CHANGE MATERIALS USING CELLULOSE AND CARBON MATERIALS…. 77
4.1 Introduction 79
4.2 Materials and Methods 82
4.2.1 Materials 82
4.2.2 Methods 82

4.3 Results and Discussion 85
4.3.1 Determination of the optimum amount of nucleating agent 85
4.3.2 Utilization of CNF and GNP in the synthesis of PCM composites 87
4.3.3 Microstructure Characterization of the PCM composites 88
4.3.4 Rheology of the PCM composites 91
4.3.5 Crystal Structure and chemical Structure characterization 94
4.3.6 Thermal Cycling Stability Characterization of PCM composites 96
4.3.7 Thermal Conductivity Characterization of PCM composites 99
4.4 Summary 101
CHAPTER 5 TAILORING OF THERMAL PROPERTIES OF LOW-COST SALT HYDRATE PHASE CHANGE MATERIALS USING EUTECTIC MIXTURES 103
5.1 Introduction 105
5.2 Materials and Methods 106
5.2.1 Materials synthesis 106
5.2.2 Characterization 108
5.3 Results and discussion 108
5.3.1 Determination of the eutectic point 108
5.3.2 XRD Characterization 111
5.3.3 Chemical Structure Characterization 114
5.3.4 Thermal Cyclic Stability of the Eutectic Mixture 114
5.4 Summary 116
CHAPTER 6 CONCLUSIONS AND RECOMMENDATIONS 117
6.1 Conclusions for each chapter 117

6.1.1 Empirical Approach to stabilize Low-Cost Salt Hydrate Phase Change Materials Using Polyelectrolyte Additives 117
6.1.2 Identification of Stabilization Mechanisms of Dextran Sulfate Sodium Polyelectrolyte in Salt Hydrate Systems using Atomic Scale Techniques 118
6.1.3 Performance Enhancement Methods for Low-Cost Salt Hydrate Phase Change Materials Using Cellulose and Carbon Materials Mixtures 118
6.1.4 Tailoring Of Thermal Properties of Low-Cost Salt Hydrate Phase Change Materials Using Eutectic Mixtures 119
6.2 Impact and Significance of this thesis 119
6.3 Limitations of the study 121
6.4 Recommendation for Future work 122
LIST OF REFERENCES 125
APPENDICES… 143
A. SUPPLEMENTARY DATA FOR CHAPTER 2 143
B. SUPPLEMENTARY DATA FOR CHAPTER 3 147
AUTHOR'S LIST OF PUBLICATIONS 156
VITA…… 158

LIST OF TABLES

Table 1.1 Comparison of various classes of PCM [9] 8
Table 1.2. Thermophysical properties of common salt hydrate PCMs for TES applications [11]13
Table 1.3. Performance target for next-generation thermal energy storage materials [38] 20
Table 2.1. Additives evaluated in this study for long-term stability enhancement of sodium sulfate decahydrate 29
Table 2.2. Flow and Viscoelastic behaviors of the base material and PCM mixtures..... 38
Table 2.3. Phase change properties of pure SSD, with different additives..... 46
Table 2.4. DSC Data for thermal cycling test of SSD-DSS-Borax composite 50
Table 3.1. Interfacial parameters for the oxygen atoms in SSD 72
Table 3.2. Difference in interaction energy between the components at 290 K and 330 K 75
Table 4.1. The compositions of composite PCMs containing CCH, SCH, CNF, and GNP..... 83
Table 4.2. Thermal properties of pure Calcium Chloride Hexahydrate and its composite PCMs 98
Table 5.1. Table 1: Composition and thermal properties of the PCM mixtures..... 110
Table 5.2. Thermal cycling data for SSD-SCD Eutectic PCM mixture 115

LIST OF FIGURES

Figure 1.1. Temperature-energy plots of sensible and latent heat storage system [11]..... 3
Figure 1.2. Thermal energy storage materials classification system[14]..... 5
Figure 1.3. Key design properties of salt hydrate PCMs for thermal energy storage [2]. 12
Figure 1.4. Sample phase diagram of sodium sulfate and water showing incongruent melting at 30 to 32 °C due to presence of additional phases [11][35]..... 15
Figure 1.5. Thermal cycling process showing the phase separation behavior of SSD [34] 15
Figure 1.6. Comprehensive materials cost for near-ambient PCMs [39] 20
Figure 2.1. Visual inspection of viscosity and miscibility of sodium sulfate decahydrate with different thickeners and stabilizers. 31
Figure 2.2. XRD Patterns of pure SSD, and SSD-based PCM mixtures. 33
Figure 2.3. ATR-IR Spectra of additives and PCM mixtures (a) SPA (b) PPA (c) CNF (d) PSS (e) DSS (f) SSD (g) SSD-SPA (h) SSD-PPA (i) SSD-CNF (j) SSD-PSS (k) SSD-DSS 34
Figure 2.4. Flow test results of SSD and other SSD-based PCM mixtures..... 37
Figure 2.5. Rheological characterization of pure SSD and SSD-based PCM mixtures (a) Amplitude sweep test. (b) Frequency sweep test. [the solid symbols represent storage modulus (G'), while outlined symbols are used for the loss modulus (G'')]. 40
Figure 2.6. Change in complex viscosity over the temperature range of 8─40 °C during 2 cycles for (a) Pure SSD (b) SSD-DSS (c) SSD-SPA 42
Figure 2.7. (a) Energy storage capacity (ESC) of pure sodium sulfate decahydrate (SSD) and SSD-based mixtures measured over 10 cycles (b) Comparison of thermal energy storage capacity vs viscosity values of SSD, and other mixtures after 10 cycles (c) ESC of SSD-DSS mixtures with various concentration of DSS over 10 cycles (d) Amplitude sweep test of pure SSD and SSD-DSS mixtures with various concentration of DSS. Inset plot shows increase in cross-over strain with corresponding increase in DSS concentration..... 45
Figure 2.8. (a) Schematic illustration of the stabilization mechanism of DSS on SSD due to electrostatic interaction and possible stearic effect. Particle size distributions of (b) Pure SSD (c) SSD-DSS composite (d) DSC thermograms of SSD-DSS-Borax through

150 thermal cycling tests. The curves are identical from cycle 1 to cycle 50 indicating the thermal stability of the PCM composite. 49
Figure 3.1. Molecular structure of dextran sulfate sodium polyelectrolyte 57
Figure 3.2. Simulation box snapshot (a) initial system with perfect crystal of SSD (bottom), (b) system at 290 K using the Gromos potential showing some degree of crystallinity, (c) system at 330 K using the Dreiding potential with loss of crystal structure in SSD. Color legend: (SSD – Yellow: S, Red: O, Purple: Na, White: H; DSS – Blue: H, Red: Carbon, Light Yellow: O, White: H, Deep Yellow: S, Pink: Na) 61
Figure 3.3. (a) DSC plot showing the melting and freezing temperatures of SSD (b) Neutron PDF data for SSD and SSD-DSS mixture obtained from NOMAD at 290 K (c) PDF data for SSD at 290 K, and 333 K (d) PDF data for SSD-DSS mixture at 290 K and 333 K 63
Figure 3.4. PDF data for SSD─DSS mixture obtained from MD simulations for Dreiding at 290 K, and Gromos at 330 K. 65
Figure 3.5. Simulated PDF Data for SSD using two different potentials. (a) S_h-S_h PDF at 290 K (b) O_h-O_h PDF at 290 K; (c) S_h-S_h PDF at 330 K; (d) O_h-O_h PDF at 330 K. The symbol, S_h, corresponds to sulfur atoms in the hydrate. The symbol, O_h, corresponds to oxygen atoms in the water of hydration. 66
Figure 3.6. PDF Data illustrating the interaction of atoms in the polyelectrolyte and salt hydrate (a) S_p-O_h at 290 K (b) O_p-O_h at 290 K (c) S_p-S_h at 290 K (d) S_p-O_h at 330 K (e) O_p-O_h at 330 K (f) S_p-S_h at 330 K. Subscript h represents the atoms in the salt hydrate while p represents the atoms in the polyelectrolytes. 68
Figure 3.7. Distribution of oxygen atoms (water) along position normal to the interface. Water of hydration migrates towards the DSS polyelectrolyte and forms an aqueous film of 1nm. 71
Figure 3.8. Comparison of Mean Square Displacement plots of the system at 290 K and 330 K for both the Dreiding and Gromos interaction potentials. 74
Figure 4.1. Cooling data showing the effect of the concentration of SCH on the supercooling of CCH 86

Figure 4.2. Schematic of the property enhancement mechanism of CNF and GNP on CCH phase change material 89
Figure 4.3. Thermal properties of CCH-based composite (a) Change in energy storage capacity of CCH-SC composites in 10 cycles (b) DSC curves of CCH-SC composites. 89
Figure 4.4. Microstructure characterization of additives and PCM composites (a) Pure CCH (b) CNF (c) GNP (d) CCH-$SC_{1.0}$ (e) CCH-$SCG_{1.0}$ (f) CCH-$SCG_{2.0.}$ Visual observation of PCM composites (g) freshly prepared sample (h) sample after 50 hours..... 90
Figure 4.5. Rheology Characterization of CCH-based PCM mixtures (a) Flow test (b) Amplitude sweep test (c) Crossover strain as a function of CNF concentration (d) Frequency sweep test. Closed symbols in (b) and (d) represent storage modulus, G' while open symbols represent loss modulus, G". 92
Figure 4.6. Crystal Structure and Chemical Structure characterization of PCM mixtures (a) XRD patterns of CCH-based PCM composites and their components (b) FTIR spectra of CCH-based PCM composites and their components 95
Figure 4.7. Thermal cycling measurement of PCM mixtures (a)Energy storage capacity of PCM in 10 cycles using DSC (b) Energy storage capacity of PCM in 70 cycles using T-History method (c)Line plot of energy storage capacity of CCH-$SCG_{1.0}$ in 50 cycles using DSC, inset shows the overlay of the DSC thermograms over 50cycles to show stability (d)Heating and cooling (inset) curve of CCH-$SCG_{1.0}$ in 70 cycles using T-History method. 97
Figure 4.8. Thermal conductivity of CCH and CCH-based PCM composites: the influence of GNP concentrations 100
Figure 5.1. PCM composition of sodium sulfate decahydrate and sodium carbonate decahydrate in varying concentration in the melted state 107
Figure 5.2. Diagrams of melting points determined by differential scanning calorimetry for $Na_2SO_4{\cdot}10H_2O$ (SSD), $Na_2CO_3 \cdot 10H_2O$ (SCD), and their combinations. A unique melting peak was seen for the 50wt% SCD (BSH5) sample, showing a distinct melting point. 109
Figure 5.3. Phase Diagram of SCD+SSD, □ , eutectic temperature; x, melting temperature 112
Figure 5.4. XRD patterns of pure SSD, SCD, and BSH5. 113

Figure 5.5. ATR-IR spectra of pure SSD, SCD, and BSH5. 113
Figure 5.6. Melting enthalpy curves showing thermal cyclic stability test for BSH5 115

CHAPTER 1
INTRODUCTION AND LITERATURE REVIEW

Global economic development is accelerating at a fast pace, creating a significant need for a reliable supply of energy especially in the building sector. For instance, commercial and residential building energy use accounts for 20% of the global energy consumption and this is projected to increase by 2.1%/year to 2040 [1]. For a long period of time, energy generated from fossil fuels met and supported human requirements. However, fossil fuel supplies are finite, and because their prices fluctuate, the availability of a steady supply of energy is exceedingly unpredictable. Additionally, increased reliance on traditional fossil fuels is wreaking havoc on the environment, owing to the release of toxic gases and contaminants into the air, which contributes to current global warming and climate change challenges. These essential challenges have spurred policymakers, engineers, and scientists worldwide to develop renewable energy technologies in order to avoid environmentally damaging solutions and to ensure global energy savings, cost reductions, energy security, and environmental advantages. It is necessary to overcome the imbalance between supply and demand that exists because of the unpredictable and variable characteristics of renewable sources of energy, including solar energy to ensure the viability of these sources. This continues to be a challenge [2][3].

Among the significant solutions in this regard is thermal energy storage (TES), a technology that enables the independent collection of thermal energy from a variety of different renewable and non-renewable sources; as a result, momentarily available energy is converted to permanently accessible energy [4]. For instance, TES devices can store solar thermal energy during the peak hours of the sun and used during off-peak/night hours leading to reduction in energy wastage and improvement in energy efficiency [5]. Generally, TES systems can be realized using three kinds of approaches which include sensible heat storage (SHS), latent heat storage (LHS), and thermochemical heat storage (THS). SHS materials such as water, sand, mineral oil, concrete and rock are capable of storing thermal energy without going through a phase change [6], [7]. During peak energy input or charging periods, energy is stored by varying the temperature of the storage medium (either liquid or solid). The amount of storage is dependent on the material's thermophysical parameters, such as specific heat, density, volume, and temperature differences of the storage medium as demonstrated by the following equation 1.1:

$$Q\ (SHS)\ =\ \int_{T_1}^{T_2} m\, c_p\, dT \qquad (1.1)$$

where Q denotes energy stored as sensible heat; m denotes the total mass of the storage medium in kilograms; and c_p denotes the specific heat capacity of the material in kJ/kg. T_2 and T_1 are the final and initial temperatures, respectively, in K.

THS system is predicated on a reversible chemical process [8]. The quantity of heat released or absorbed in such a reaction is equal to its enthalpy. As illustrated in Equation 1.2, forward endothermic reactions absorb heat during the charging phase and use the thermal energy obtained to dissociate a chemical reactant (X) into products (Y) and (Z). Reactants (Y) and (Z) undergo a reverse exothermic reaction during the discharge process, resulting in the creation of (X) and the release of heat. Both reactions produce compounds that may be kept at either ambient or working temperatures. The thermal energy stored in thermochemical materials is represented in equation 1.3 below:

$$X + \Delta H \leftrightarrow Y + Z \qquad (1.2)$$

$$Q\ (THS) = n \cdot \Delta H \qquad (1.3)$$

where n represents the number of moles of reactant X and ΔH is the reaction enthalpy (kJ/mol).

The LHS system is predicated on the storage and release of heat by phase changes in the storage medium, such as solid–solid, solid–liquid, or liquid–gas. The energy that a substance absorbs during a phase change is referred to as the latent heat of fusion or vaporization, depending on the phase involved. Due to the widespread accessibility of storage materials, better energy storage per unit volume, reduced energy losses, and nearly isothermal operation of thermal storage/retrieval, LHS systems are regarded as the most promising and attractive approach for storing thermal energy [9]. The temperature–energy curves for SHS and LHS are shown in Figure 1.1. The thermal storage process for SHS system is dependent on their specific heat capacity and temperature difference for pure SHS, whereas the overall heat storage process for LHS systems includes three processes (SHS of solids, phase change LHS, and SHS of liquids), hence, the LHS systems can store heat 5 to 14 times better than the SHS system [10]. The thermal energy stored in LHS materials is represented in equation 1.4 below:

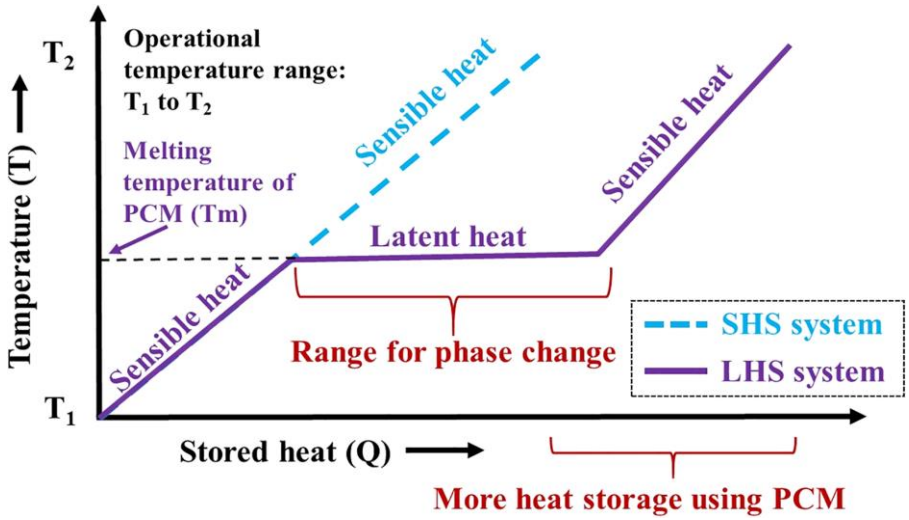


Figure 1.1. Temperature-energy plots of sensible and latent heat storage system [11]

$$Q\ (LHS)\ =\ \int_{T_1}^{T_m} mc_p, solid\ phase\ dT\ +\ \Delta H\ +\ \int_{T_m}^{T_2} mc_p, liquid\ phase\ dT \qquad (1.4)$$

where T_1, T_m, T_2 are the initial temperature, melting temperature, and final temperature of operation respectively; c_p, *solid phase*, and c_p, *liquid phase* are the specific heat capacity of the solid phase and liquid phase respectively; ΔH denotes the latent heat.

1.1 Classification of LHS Systems

The precise temperature control provided by LHS systems allows for the efficient storage and extraction of thermal energy. To compensate for intermittent or irregular thermal sources (like solar heating) or shift peak loads, LHS systems provide a mechanism for decoupling thermal energy supply and demand over time and space [12]. Phase change materials (PCMs) are generally used as media for LHS system. Depending on the application, PCMs can store and release thermal energy through solid-liquid, solid-gas, liquid-gas, and solid-solid phase transition. Thermal conductivity, high latent heat per unit volume, and thermal stability are all desirable features of PCMs that are safe to employ in systems or devices [13]. These desirable properties have made LHS systems receive a strong interest in the field of renewable energy [14], specifically in energy-efficient buildings [15], solar thermal energy storage [16], hot water systems [17], air conditioning systems [18], cold storage [19], thermal management for power batteries [20] and electronics [21], residential heating [22], food packaging [23], and waste heat recovery [24]. In recent decades, substantial research has been conducted to characterize the many types of PCMs across a broad range of melting temperatures and melting enthalpy. These materials are classified based on phase change form in Figure 1.2.

Generally, PCM are classified as inorganic (salt hydrates, metals, and salt), organic (fatty acids, paraffin), and eutectic (combinations of PCMs with sharp melting point). Organic PCMs, such as paraffin, fatty acids, oil, and wax are mostly obtained from the food and hydrocarbon industries. They are inexpensive, straightforward to utilize in thermal applications, have a minimal environmental impact, and are abundant in natural sources. They have historically been one of the most widely utilized commercial PCMs. With a long history of usage in thermal devices and a higher level of material durability when subjected to repeated thermal cycling. Also, they melt congruently, have good nucleation properties and are non-corrosive [25].

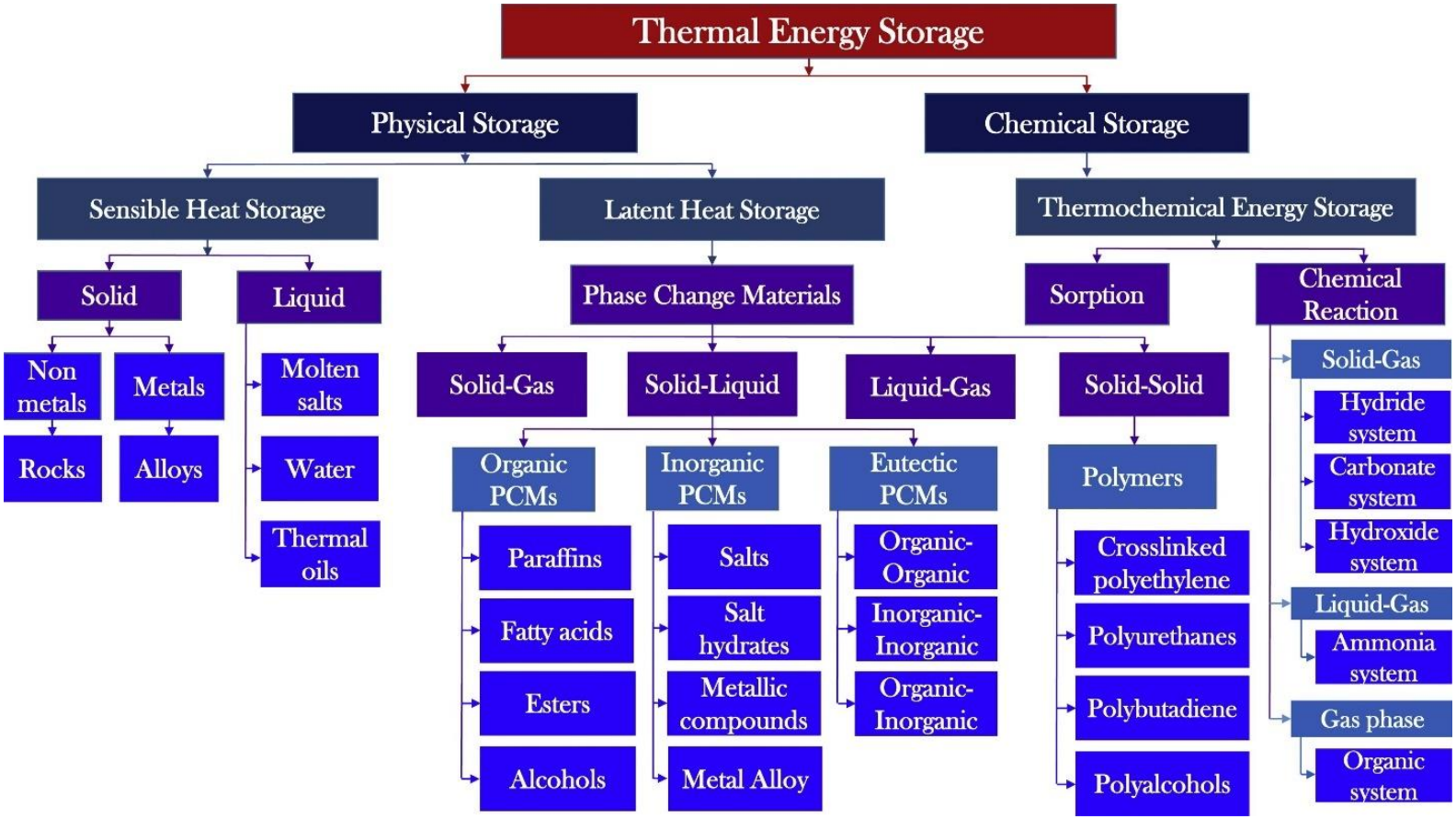


Figure 1.2. Thermal energy storage materials classification system[14]

Organic PCMs are often a combination of long-chain hydrocarbons such as paraffin [C_nH_{2n+2}, with n being an integer] and nonparaffin compounds including esters, amides, ketones, sugars, dienes etc. Hence, the range of melting point is dependent on the length of carbon chain and other constituents of the organic PCMs [26]. However, organic PCMs have poor thermal conductivity and highly inflammable. This reduces their use in TES applications. Inorganic PCMs are composed of salts, salt hydrates, salt-metal combinations, and alloys in which the atoms are held together by ionic bonds. Typically, they consist of alkali metal salts containing anions such as oxides, hydroxides, sulfates, chlorides, nitrates, chlorates, and carbonates. Inorganic PCMs have a wider phase change temperature range, a higher volumetric energy storage capacity, a higher thermal conductivity, are less expensive, and are nonflammable when compared to organic PCMs [9]. Anhydrous salts coupled with water molecules in a stoichiometric ratio can occasionally form hydrated salts with crystalline structure (based on the level of hydration). As a result, the salt hydrate comprises of salt and water molecules mixed in a specific ratio. The chemical interaction inside the crystal structure allows for precise positioning of water molecules within the crystal structure. When a salt hydrate is heated over its melting point, the hydrated water molecules are liberated.

Eutectic PCMs are made up of two or more different materials in a predetermined proportion and temperature condition, which confers the unusual feature of congruent melting and freezing on them. This implies they have sharp melting point lower than the constituent materials [27]. Frequently, the crystal structures of eutectic mixes are identical to those of their components which means the mixing of the constituent PCMs is not chemical process. Among the classes of PCMs discussed above, inorganic PCMs especially salt hydrates are widely used for TES applications based on the comparative advantages they offer as shown in Table 1.1.

1.2 Salt hydrates Phase Change Materials

Salt hydrates are salt-water compounds with the general formula $AB\cdot nH_2O$. Salt hydrates undergo reversible solid-liquid phase transitions via hydration and dehydration. The transition temperatures of the majority of these salt hydrates range from 5 to 130 °C. Due to their high volumetric energy storage capacity (86–328 kJ/kg and 350 MJ/m^3), superior thermal conductivity (0.7 W/m.K) to organic PCMs, low volume change during phase transition, low toxicity,

nonflammability, compatibility with containers, and low cost, salt hydrates have been extensively investigated and are the most significant category of PCMs [28].

1.2.1 Mechanism of phase change in salt hydrate PCMs

Phase change is the mechanism by which latent thermal energy is stored. In salt hydrates, the phase transition process is equivalent to the melting and freezing of the material. However, in salt hydrates, this can be accomplished through dehydration and hydration, or by partially hydrating and partially dehydrating the salt hydrates. For an inorganic salt, AB absorbing or releasing heat, Q during phase change, the following equations depicts the possible phase change mechanisms [11]:

Dehydration: $AB \cdot nH_2O \xrightarrow{Q\ (\downarrow)} AB + nH_2O$ (1.5)

Hydration: $AB + nH_2O \xrightarrow{Q\ (\uparrow)} AB \cdot nH_2O$ (1.6)

Partial Dehydration:

$AB.nH_2O \xrightarrow{Q\ (\downarrow)} AB + mH_2O + (n-m)H_2O\ (m < n)$ (1.7)

Partial Hydration: $AB + nH_2O \xrightarrow{Q\ (\uparrow)} AB \cdot pH_2O + (n-p)H_2O \quad (p < n)$ (1.8)

To convert salt hydrate (AB · nH$_2$O) to solid anhydrous salt phase (AB) and liquid water, heat must be absorbed by the salt hydrate (Equation 1.5). When the binary phase is cooled, the released fusion heat transforms it into a solid salt hydrate (Equation 1.6). In real situation, the water required for hydration is inadequate to create the salt hydrates, hence a lower hydrate is formed (Equations 1.7, and 1.8) [29]. The melting characteristics of salt hydrates can be separated into three classes based on the mechanism described above. Based on the mechanism explained above, salt hydrates can be divided according to their melting behavior into three groups:

Table 1.1 Comparison of various classes of PCM [9]

Classification	Organic PCMs		Inorganic PCMs		Eutectics
	Paraffins	Fatty acids	Salt Hydrates	Metallic	
Formula	C_nH_{2n+2} (n>11)	$CH_3(CH_2)_{2n}\cdot COOH$	$AB\cdot nH_2O$	-	-
Melting point	-12 to 135 °C	-7 to 187 °C	-33 to 120 °C	29.8-125 °C	-30.6 to 93 °C
Latent heat	60-269 J/g	125-250 J/g	86-328 J/g	25-90.9 J/g	100-267 J/g
Thermal conductivity	0.2 W/m.K	0.2 W/m.K	0.7 W/m.K	40.6 W/m.K	0.680 W/m.K
Key features	1. As chain length increases, the melting point and latent heat increase. 2. The most commonly utilized PCMs	1. Unlike paraffins, each substance has its own set of characteristics. 2. There is a wide range of latent heat and melts.	1. Alloys of inorganic salts and water 2. A higher enthalpy of phase change	1. It is not seriously utilized because of its heavier weight.	1. During phase change process, there is no phase segregation. 2. A mixture of two or more inorganic or organic components, or both

Table 1.1 Continued

Classification	Organic PCMs		Inorganic PCMs		Eutectics
	Paraffins	Fatty acids	Salt Hydrates	Metallic	
Advantages	1. Safe, chemically stable, and non-corrosive 2. Minimal supercooling or phase separation tendency. 3. Hight latent heat of fusion. 4. Compatible with metal containment 5. More affordable and readily available	1. High latent heat 2. Sharp phase change 3. Fatty acids melt and freeze easily. 4. Absence of supercooling	1. High volumetric energy storage capacity 2. Good thermal conductivity 3. Modest change in comparison to others 4. Increased density 5. Easily accessible and inexpensive 6. Sharp melting point	1. Thermal conductivity is high. 3. High volumetric energy storage capacity	1. Good conductivity 2. High volumetric energy storage
Disadvantages	1. Inadequate thermal conductivity and density 2. Unsuitable for use in a plastic container 3. High volume expansion, flammable and volatile 4. Sharp melting point is not well-defined	1. Poor conductivity 2. Low flash point; 3. Unstable at elevated temperatures; very flammable. 4. Toxic and mildly corrosive 5. Two to three times the price of paraffins	1.Corrosion damage to metallic containments 2. Phase Separation 3. Instability at high temperatures 4. Supercooling 5. Slightly poisonous	1.Low specific heat capacity 2. Expensive 3. Low fusion heat per unit mass	1. Low specific heat of fusion

Table 1.1 Continued

Classification	Organic PCMs		Inorganic PCMs		Eutectics
	Paraffins	Fatty acids	Salt Hydrates	Metallic	
Enhancement methods	1. Insertion of fins in the TES system. 2. The incorporation of high thermally conductive compounds 3. Incorporating flame retardants	1. Compounds that act as a fire retardant 2. Additives that improve thermal conductivity	1. Additives that act as nucleating and stabilizing agents 2. Stirring Mechanically 3. Excess water usage 4. Encapsulation of PCM		

- Congruent melting behavior: The anhydrous salt is completely dissolved in the hydration water at the salt hydrate's melting point or throughout the hydration process.
- Incongruent melting behavior: The anhydrous salt is insoluble in the hydration water at the salt hydrate's melting point or during the hydration process.
- Semi-congruent melting behavior: At the salt hydrate's melting temperature or during hydration, just a trace quantity of anhydrous salt is converted to salt hydrate or salt hydrate with less water.

1.2.2 Selection criteria and applications of salt hydrate PCMs

Several material characteristics, including physical, thermal, chemical, and kinetic properties, as well as price, ready accessibility, reliability, safety, and scalability are considered essential selection factors for PCMs for each thermal energy storage application. The key design properties for PCMs are depicted in Figure 1.3. Apart from their availability and affordability, the primary attributes of salt hydrate PCMs are their physical, thermal, kinetic, and chemical characteristics [30]. These features demonstrate the suitability and usability of salt hydrate PCM for certain TES applications [31].

A) **Thermal Properties**

Salt hydrate PCMs desirable for TES applications should have the thermal properties as follows: high phase change enthalpy, congruent melting behavior, and high thermal conductivity. Phase transition temperature is an important metric for the selection of salt hydrate PCMs for particular TES application. The phase change temperature should be compatible with the cooling and heating temperatures used for charging-discharging cycle of the TES device. Also, high energy storage density of the PCM aid in the storage system's weight and form factor minimization. The salt hydrate PCM's high heat conductivity permits quick charging and draining of the storage system. Table 1.2 illustrates some of the salt hydrates commonly used in TES applications with their respective thermal properties.

B) **Chemical Properties**

Desirable salt hydrate PCMs for TES applications must have the following chemical properties: low phase separation during repeated thermal cycling, nontoxicity, non-flammability, and compatibility with containing systems. The compatibility of materials (i.e., corrosiveness and

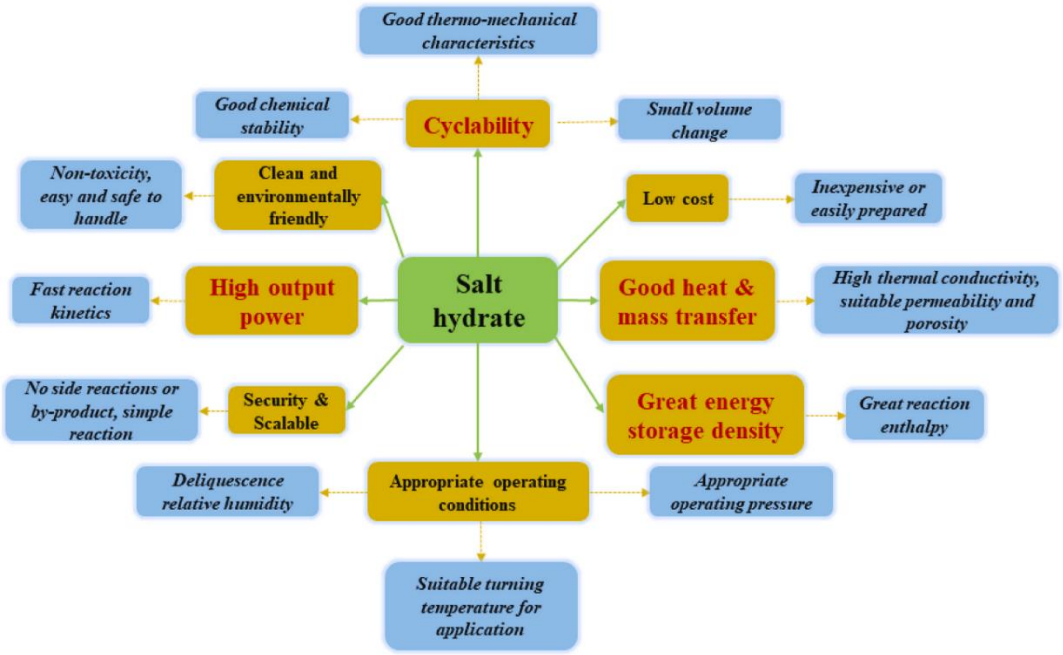


Figure 1.3. Key design properties of salt hydrate PCMs for thermal energy storage [2].

Table 1.2. Thermophysical properties of common salt hydrate PCMs for TES applications [11]

Salt Hydrates	Melting point (°C)	Latent heat (J/g)	Specific heat capacity (J/g.K)		Density (Kg/m^3)		Thermal conductivity (W/m.K)	
			Solid	Liquid	Solid	Liquid	Solid	Liquid
$CH_3COONa{\cdot}3H_2O$	58	264-267	1.77	2.9	145	-	0.43	0.34
$Na_2SO_4{\cdot}10H_2O$	32.4	238	1.92	3.26	1460	1330	0.514	0.589
$Na_2CO_3{\cdot}10H_2O$	32-36	246.5	1.92	3.26	1442	-	0.514	0.224
$Na_2HPO_4{\cdot}12H_2O$	35	280	1.70	1.95	1520	1440	0.514	0.476
$Na_2S_2O_3{\cdot}\ 5H_2O$	48-49	201-210	1.46	2.39	1750	1670	0.76	0.38
$Zn(NO_3)_2{\cdot}\ 6H_2O$	36	134	1.34	2.26	1954	1828	-	0.464
$CaCl_2{\cdot}\ 6H_2O$	29.8	171	1.42	2.10	1800	1562	1.088	0.54
$CaBr_2{\cdot}\ 6H_2O$	34	115.5	-	-	2190	1956	-	-
$CaCl_2{\cdot}\ 4H_2O$	44.2	99.6	1.25	2.13	1680	1500	0.626	0.45
$MgCl_2{\cdot}\ 6H_2O$	117	169	1.72	2.82	1569	1450	0.694	0.57
$Mg(NO_3)_2{\cdot}\ 6H_2O$	89.3	167	1.84	2.51	1636	1550	0.611	0.49
$Mn(NO_3)_2\cdot 6H_2O$	25.3	148	-	-	1600	1738	-	-
$KF{\cdot}\ 4H_2O$	19	231	1.84	2.39	1450	1450	-	-
$LiClO_3{\cdot}\ 3H_2O$	8	253	-	-	1720	1530	-	-
$Ba(OH)_2\cdot 8H_2O$	78	266	1.17	2.44	2070	1937	1.255	0.653

- means Not reported

chemical reactivity) between PCM and containment structures is critical throughout the selection process of the salt hydrate PCM. The toxicity and flammability of PCMs are also critical considerations in the selection process, depending on the application.

C) **Kinetics**

A desirable salt hydrate PCM for temperature control application must have fast, steady, reversible, and dependable kinetics. This ensures that heat extraction and absorption during repeated thermal cycling is effective. Also, a desirable salt hydrate PCM shows higher nucleation rate and an adequate crystallization rate, this makes supercooling minimal and substantial amount of heat is released during the freezing process. Hence, it is a critical factor to consider for short term thermal energy storage application requiring rapid release and absorption of heat for temperature control applications.

1.2.3 Technical Challenges and opportunities with PCMs

Numerous issues are discussed in the literature about the application of salt hydrates in TES devices and systems. These include the following:

(1) phase separation over repeated temperature cycles,

(2) supercooling as a result of bad nucleation characteristics,

(3) Low thermal conductivity, and

(4) Limited options for near-ambient applications. These technical challenges have limited the widespread application of salt hydrate PCMs in thermal energy applications [32].

For instance, when sodium sulfate decahydrate (SSD) PCM is thermally cycled, phase separation occurs, resulting in a significant loss of melting enthalpy over lengthy freeze/melt cycles [33]. When SSD is heated, the composition follows the vertical line corresponding to a mass fraction of 43% Na_2SO_4, as illustrated in Figure 1.4. When the transition temperature of 32 °C is attained, two distinct phases emerge: solid anhydrous Na_2SO_4 and a liquid suspension with approximately a 32 percent mass fraction of Na_2SO_4. The densities of these two stages are vastly different. Because the residual anhydrous salt does not dissolved in water entirely, salt solution including undissolved anhydrous salt emerges. [34]. The anhydrous salt particles settle to the bottom due to the density difference between the anhydrous salt and the salt solution, resulting in a mixture with phase segregation, as shown in Figure 1.5. As a result, when the phase-separated mixture is frozen, it cannot be entirely restored to SSD.

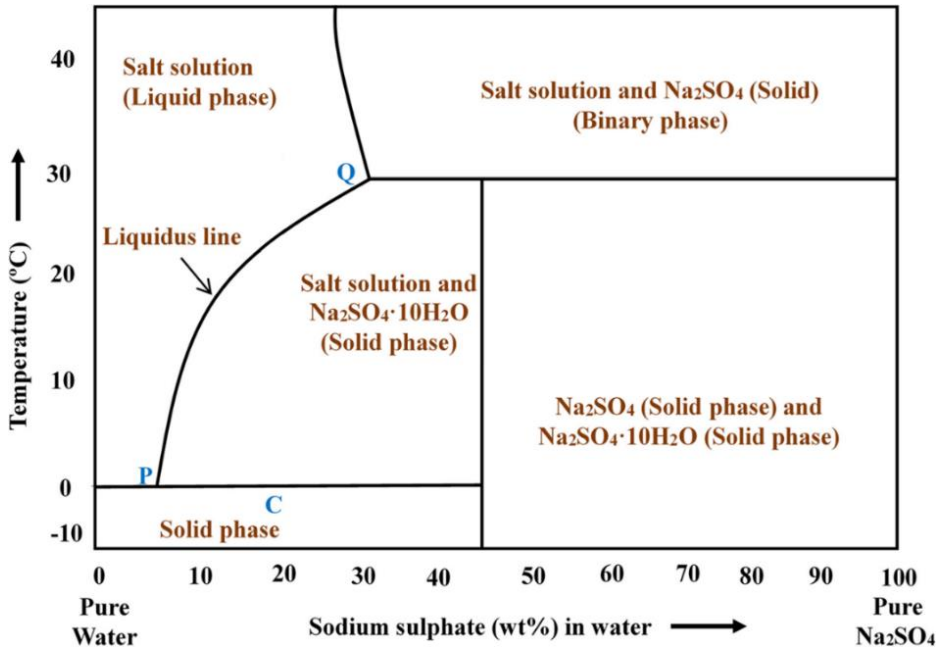


Figure 1.4. Sample phase diagram of sodium sulfate and water showing incongruent melting at 30 to 32 °C due to presence of additional phases [11][35]

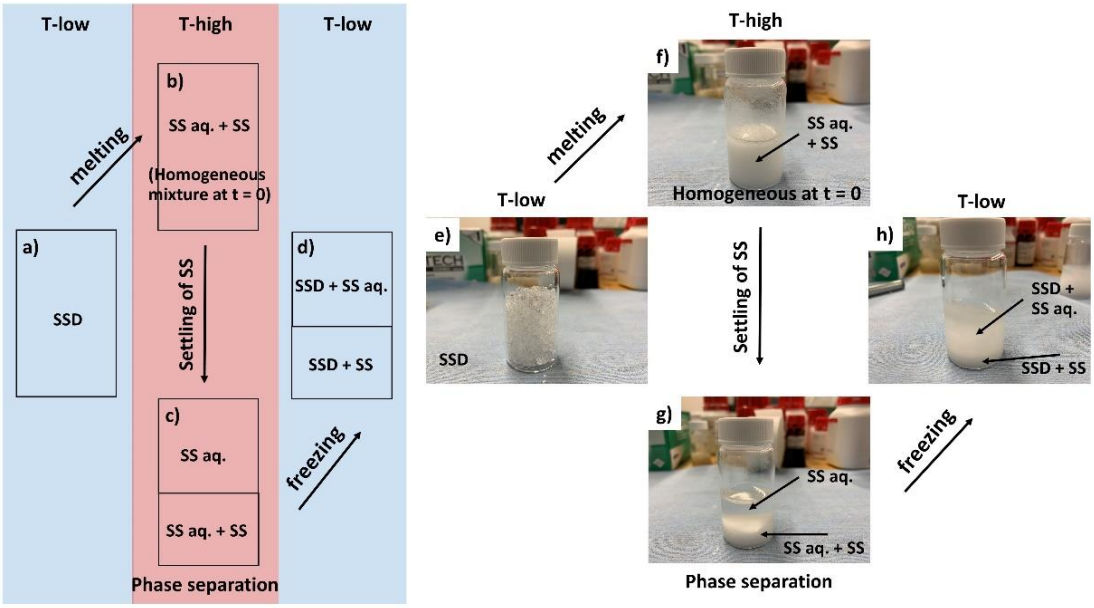


Figure 1.5. Thermal cycling process showing the phase separation behavior of SSD [34]

Consequently, the latent heat of the freezing process is less than the latent heat of melting because lesser material goes through the freezing process. This is because the material loses its ability to store thermal energy over time when it is heated and cooled. If phase separation is not mitigated, significant loss in energy storage capacity over repeated thermal cycling would be observed, thereby limiting the use of PCMs for long-term TES applications.

In the same vein, numerous experimental approaches have been explored for the prevention of phase separation and the enhancement in the properties of PCMs to make them readily available and dependable for diverse TES application. However, little insight is known on the behavior of these materials at the atomic level. The use of advanced atomic techniques such as molecular dynamics simulations, and scattering techniques could unravel new understanding of the processing-structure-property-performance relationships in these materials. Another major challenge of salt hydrate PCM is significant supercooling and the unpredictability of nucleation during repeated thermal cycling. During the solidification process, salt hydrate PCMs remain in the liquid state even when they are cooled to their phase transition temperature [36]. This can lead to insufficient time for solidification or additional energy requirement to trigger nucleation. Hence, the supercooling phenomenon in salt hydrates can have a major influence on energy extraction during solidification, impacting TES system performance and dependability.

As much as the PCMs have attractive volumetric energy storage density, they also have inherent low thermal conductivity. This could be a challenge in developing TES systems with fast charging and discharging rate. Specifically, the materials show slow heat transfer rates during the charging and discharging processes which could limit the overall thermal performance of the TES system. [37] Furthermore, most of the low-cost salt hydrate PCMs available have phase change temperatures above the room temperatures. This limits the options and alternatives of PCMs required for near-ambient applications, especially the integration with heat pump for comfort cooling and heating.

With the major challenges discussed above, there are opportunities to enhance the functional integrity of salt hydrates for TES applications in this regard. This could be accomplished by the careful selection and incorporation of effective additives such as thickening agents and stabilizers to mitigate the phase separation problems in salt hydrate over repeated thermal cycling. Also, addition of nucleators could enhance low supercooling degree in the system. Furthermore,

the use of advanced atomistic techniques could provide critical insight into the atomic structure and properties of PCMs which could be relevant in addressing the critical limitations of salt hydrates for TES systems. The development of new PCMs with good stability and suitable phase change temperatures for near-ambient thermal energy storage applications would enable the widespread use of salt hydrate PCMs as viable materials for the thermal engineering community.

1.3 Research Problem and Research Question

It is established in the contemporary literature that several challenges have limited the reliability of PCMs for thermal energy storage applications. These key technical challenges include phase separation and excessive supercooling. Phase separation is a typical issue with salt hydrates PCMs that undergo incongruent melting, resulting in the salt failing to properly rehydrate throughout a melt-freeze cycle, leading to significant loss of energy storage capacity after repeated thermal cycles. Supercooling happens when the PCM is cooled below its equilibrium melting point but does not nucleate or freeze. Further cooling will finally result in the phase transition. However, this process leads to inconsistent nucleation which is not a desirable property of PCMs for various applications of interest. To efficiently harness the potential of salt hydrates PCMs, these challenges must be addressed through the development of PCMs with desirable stability and minimal supercooling. This has led to these fundamental research questions:

- *What are the viable approaches for stabilizing salt hydrate PCMs for long-term use in thermal energy systems? Can we identify effective process or materials that enhance the properties of low-cost salt hydrate PCMs, especially sodium sulfate decahydrate for TES applications?*
- *What is the atomistic mechanism by which additives (such as polyelectrolytes) stabilize salt hydrates? Can we deduce the chemical basis for the stabilization of low-cost salt hydrate PCMs utilizing effective stabilizers such as polyelectrolytes?*
- *Is it possible to enhance the thermal performance of PCMs by developing composites using effective additives which could serve as thermal conductive medium or dispersant in the PCM matrix?*
- *Is it possible to engineer low-cost congruent salt/water based PCMs with phase change temperature $\leq 25^{\circ}$ C for human thermal comfort and buildings applications?*

1.4 Research aims and Objectives.

The overarching aim of this study is to address the technical challenges with the utilization of salt hydrate PCMs through the development and characterization of stable salt hydrate phase change materials with enhanced performance for temperature control and thermal energy storage applications. This also extends to the investigation of the structure, properties, and important mechanisms in salt hydrate PCMs at the atomic level. To achieve this aim, the main tasks or objectives of this study include:

Objective 1: Conduct experiment to determine the best approaches to mitigate phase separation and enhance stability using selected list of low-cost salt hydrate PCM with various additives and characterize the performance of these selected PCM mixtures after repeated thermal cycling (addresses phase separation problem).

Objective 2: Perform computer simulation to provide fundamental understanding of the stabilization mechanism of salt hydrate PCMs with effective additives or stabilizers (addresses phase separation problem).

Objective 3: Develop composite PCMs based on the low-cost salt hydrate PCM, cellulose nanofibrils, and graphene nanoplatelets, and characterize the structure and stability of these materials for long-term energy storage (addresses incongruent melting, supercooling, and low thermal conductivity problems).

Objective 4: Develop eutectic PCMs with phase change temperature $\leq 25\,°C$ based on the mixture of two low-cost salt hydrate PCMs (especially $Na_2SO_4{\cdot}10H_2O$ and $Na_2CO_3{\cdot}10H_2O$) and characterize the optimum concentration for the eutectic mixtures (addresses limited options for near-ambient temperature applications).

1.5 U.S. Department of Energy (DOE) thermal energy Storage program targets

This work is funded by the U.S. Department of Energy Building Technology Office (BTO) and the mission of BTO is to expedite the commercialization and usage of next-generation energy storage technologies for building applications via research, development, demonstration, and deployment (RDD&D) of thermal storage systems. This study supports the efforts of BTO through the research and development of low-cost high performing materials with size and weight for easy deployment in building. As a path forward towards the achievement of the mission, certain

characteristics and performance targets have been highlighted for the selection of suitable PCMs as shown in Table 1.3 [38]. A major metric to consider is the cost target. Generally, the cost of energy storage by PCMs is determined by dividing the price of the PCM per unit mass by its enthalpy of solid-liquid phase change, which is expressed in terms of cost (US dollars) per unit latent heat energy storage as shown in Equation 1.9:

$$\text{Cost of Energy Storage, C} = \frac{\text{price per unit mass (\$/kg)}}{\text{melting enthalpy (kWh/kg)}} \tag{1.9}$$

For a composite material including salt hydrates A, B, and other additives without latent heat, C & D, the cost is expressed as:

$$\text{Cost for PCM composite, } C_{comp} = \frac{p_A c_A + p_B c_B + p_C c_C + p_D c_D}{p_A \Delta H_A + p_B \Delta H_B} \tag{1.10}$$

Where c_A is the bulk cost of the material A in \$/kg. ΔH is the latent heat or enthalpy of salt hydrate in kWh/kg, p_A is the mass fraction of material A, relative to total mass, m_T which could be expressed in term of density, ρ and volume, V as:

$$\text{Partal mass, } p_A = \frac{m_A}{m_T} = \frac{\rho_A V_A}{\rho_A V_A + \rho_B V_B + \rho_C V_C + \rho_D V_D} \tag{1.11}$$

Hirschey et al. [39] reported a comprehensive cost analysis of various classes of PCMs (Figure 1.6). It was found that salt hydrate PCMs had the lowest costs, favorable melting enthalpy, (100-290 J/g), and competitive volumetric energy density, making them suitable for thermal energy storage in applications ranging from buildings to transportation systems. When we consider the cost target of \$15 /kWh set for the utilization of materials thermal energy storage applications, it is important to select salt hydrates with lower costs, suitable phase change temperature, and melting enthalpy.

Table 1.3. Performance target for next-generation thermal energy storage materials [38]

Metric Description	Metric
Phase Change Temperature	Achievable range of transition temperatures
Large-scale availability and low price	< \$15 /$kWh_{thermal}$
Energy density	> 100 kWh/m^3
Thermal reliability	> 90% after 5, 000 cycles
No phase separation	Minimized
Supercooling	Minimized; < 2 °C

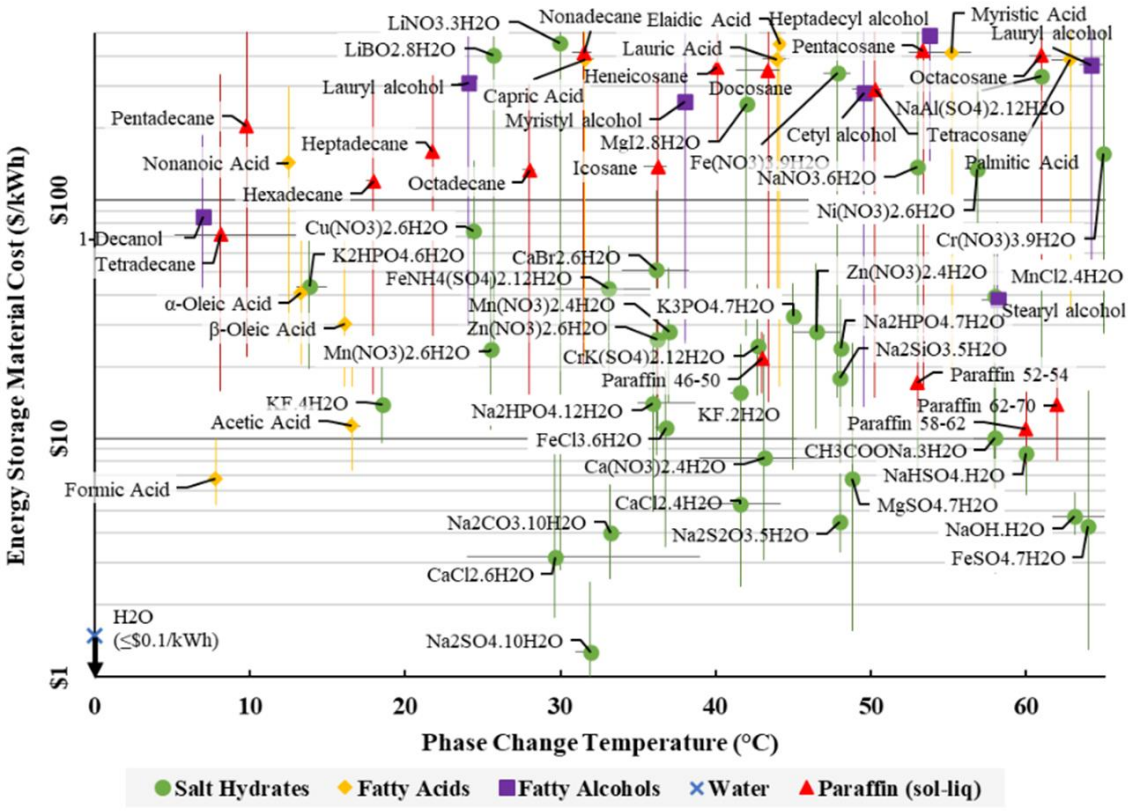


Figure 1.6. Comprehensive materials cost for near-ambient PCMs [39]

Examples of salt hydrate PCMs that are considered in this study include sodium sulfate decahydrate, sodium carbonate decahydrate, and calcium chloride hexahydrate. However, these salts require enhancement mechanisms to improve their thermal energy storage performance. This study involves the use of several additives such as nucleators, thickeners, stabilizers, and thermal conductivity enhancer to correct inherent problems in salt hydrate PCMs. As a result, the following salt hydrate and additives were selected for this study:

- Inorganic PCMs: Sodium sulfate decahydrate, Calcium chloride hexahydrate, Sodium carbonate decahydrate
- Thickeners and Stabilizers: Sodium Polyacrylate, Potassium Polyacrylate, Cellulose Nanofiber, Dextran sulfate sodium, Poly (sodium 4-styrenesulfonate), hydroxyl ethyl cellulose, carboxyl methyl cellulose, silica fume, and graphene nanoplatelets
- Nucleators and other additives: Borax, and strontium chloride hexahydrate

1.6 Research scope

The scope of this study is focused on inorganic salt hydrate PCM candidates capable of meeting thermal energy storage requirements and exhibiting the appropriate range of phase change temperatures for near ambient thermal energy storage applications. As a result, PCM with phase transition temperatures between 20 and 40 °C is sought. Also, other selection criteria include low cost, high latent heat capacity, material stability, and compatibility.

1.7 Organization of the thesis

The results and information obtained from this dissertation to address the research objectives will be organized as follows:

- Chapter 2: stabilization by additives. This chapter discusses the different approaches for mitigating phase separation in low-cost salt hydrate PCMs such as sodium sulfate decahydrate. Several additives to prevent phase segregation in PCM mixtures are tested. Furthermore, the effects of these additives on the structural, thermal, and rheological properties of PCMs are explored. The successful mitigation of phase separation would enhance the reliability and durability of PCMs for long-term TES applications.
- Chapter 3: polyelectrolyte stabilization mechanism. This chapter presents both theoretical and experimental perspectives on the stabilization of sodium sulfate decahydrate PCMs

using polyelectrolytes. The atomistic mechanism of the interaction between dextran sulfate sodium and sodium sulfate decahydrate are investigated using molecular dynamics simulations and total scattering techniques. The use of advanced atomistic techniques can provide key understanding of the structure-property relationships of salt hydrate PCMs at the atomic level. This insight could help in the designing high-performing salt hydrate PCMs for TES applications.

- Chapter 4: performance enhancement by additives. This chapter discusses the performance enhancement of low-cost salt hydrate PCMs using effective additives. The section presents the development of a composite salt hydrate phase change material based on $CaCl_2 \cdot 6H_2O$, strontium chloride hexahydrate (SCH), cellulose nanofibrils (CNF), and graphene nanoplatelets (GNP). SCH serves as nucleation enhancer, CNF serves as dispersant and thickener, while GNP serves as the thermal conductivity enhancer in the composite PCM. The structure, rheology, and long-term stability of this PCM for thermal energy storage applications are investigated. This work provides an effective approach to reducing supercooling and enhancing the thermal performance of low-cost salt hydrate PCMs for TES applications.
- Chapter 5: binary eutectic mixture development. This chapter presents the development of binary salt hydrate PCM based on mixing sodium sulfate decahydrate and sodium carbonate decahydrate. The optimum concentration for the eutectic mixture is evaluated, and the chemical structure, phase change temperature, and thermal stability of the PCM mixtures during repeated thermal cycles are investigated. This work provides PCM options for near-ambient thermal energy storage applications, especially for human comfort cooling.
- Chapter 6: conclusions. This chapter highlights the detailed summary of all the prior research discussed in chapters 2, 3 and 4. Also, the unique contributions and impact of this thesis are discussed extensively, and the recommendations for further research are highlighted.

CHAPTER 2

EMPIRICAL APPROACH TO STABILIZE LOW-COST SALT HYDRATE PHASE CHANGE MATERIALS USING POLYELECTROLYTE ADDITIVES

This chapter highlights the work done to address the phase separation problems in salt hydrate PCMs using various additives. This is necessary to stabilize the energy storage capacity and improve the reliability of PCMs for repeated thermal cycling in TES applications.
It includes an extended draft version of the of article accepted for publication in a scientific journal.

Acknowledgements: This work was sponsored by the U. S. Department of Energy's Building Technologies Office under Contract No. DE-AC05-00OR22725 with UT-Battelle, LLC

Chapter Abstract

The phase change material (PCM) sodium sulfate decahydrate ($Na_2SO_4 \cdot 10H_2O$, SSD) is capable of storing thermal energy. Nonetheless, phase separation and unreliable energy storage capacity (ESC) restrict its use. To address these concerns, eight different polymer additives─sodium polyacrylate (SPA), carboxymethyl cellulose (CMC), Fumed silica (SiO_2), potassium polyacrylate (PPA), cellulose nanofiber (CNF), hydroxyethyl cellulose (HEC), dextran sulfate sodium (DSS), and poly(sodium 4-styrenesulfonate) (PSS)─were used to explore several stabilizations mechanisms. Using these additives that are compatible with SSD, the structural, thermal, and rheological properties of SSD were investigated. Ten cycles of thermal cycling revealed that the ESC of a pure SSD decreased from 217 J/g to 135 J/g. The addition of thickeners, SPA, PPA, and CNF did not improve the ESC since, after 10 cycles, the mixes degenerated to 135 J/g. During 10 and 150 melt-freeze cycles, DSS-modified PCM mixtures displayed higher stability with ESC values of 210 J/g and 145 J/g, respectively. In comparison to pure SSD, which had a viscosity of 0.02 Pa. s, samples containing CNF, SPA, PPA, PSS, and DSS had viscosities of 1,351 Pa s, 1,120 Pa s, 96 Pa s, 79 Pa s, and 1 Pa s, respectively. This indicates that DSS did not substantially affect the viscosity of SSD during stabilization. Dynamic light scattering demonstrated that DSS decreases SSD particle size and electrostatically suspends salt particles in a stable homogeneous solution, hence preventing phase separation. Using polyelectrolyte-salt hydrate mixtures for thermal energy storage applications, this work suggests a viable strategy for enhancing the thermal stability of salt hydrate PCMs.

2.1 Introduction

In a bid to reduce mismatch between energy supply-demand created by urbanization, labor productivity, industrialization and the depletion of conventional fossil fuels, research and development of technologies with steadier, efficient, and stable energy are gaining important attention [40]. Latent heat thermal energy storage systems (LHTESS) are proving to be one of the promising means of storing energy for short-term or long-term use in heating, ventilation and air conditioning (HVAC) devices in commercial and residential buildings [41]. Phase change materials (PCM) have shown enormous potential for LHTESS. PCMs are desirable for many applications, especially in buildings and power generation. In buildings, the use of PCMs can smooth temperature fluctuations, reduce the peak load, and increase the thermal inertia of the building; and can flexibly be incorporated either passive or active systems [42].

Salt hydrate PCMs is a highly desirable material for heat storage applications due of their low cost, high volumetric energy storage capacity, relatively low melting point, small temperature glide, and wide availability [43]. However, a majority of salt hydrate PCMs suffer from phase separation after successive melt-freeze cycle and supercooling that reduces the energy storage capacity. Several methods have been adopted to solve the phase separation problem, such as, mechanical agitation of the PCM container [44], physical and/or chemical micro encapsulation of PCM, and addition of polymeric or other highly viscous materials as stabilizer. These additives have shown promise to prevent phase separation in PCM by limiting the diffusion rate and distance between the salt and water molecules during incongruent melting [45].

In thermal energy storage (TES) applications, sodium sulfate decahydrate (SSD), $Na_2SO_4 \cdot 10H_2O$ (Glauber's salt) is of particular interest due to its low cost and non-flammability. However, SSD suffers from severe phase separation (dissociation of anhydrous salt from water during melting and difficulty in recombining during freezing), and supercooling (unpredictable freezing) which reduces its thermal storage capacity after successive melt/freeze cycles [46]. Supercooling in SSD can be reduced through the addition of nucleators such as sodium tetraborate (borax) in varying concentrations to trigger the crystallization of SSD in a timely and consistent manner [11]. To prevent phase separation, it is important to constrain water and the anhydrous salt to appropriate positions to enable easy dissociation and combination after phase change

processes. Several studies have utilized high absorbent materials which increase the viscosity of salt hydrate and reduces phase separation. Early investigations by Marks et al. [12] on the thermal stability of attapulgite clay thickened SSD exhibited 320 thermal cycles. Calorimetric measurement have shown a decline in energy storage capacity of neat SSD from 238 J/g to ~63 J/g after 40 cycles, while the thickened SSD showed a decline from 202 J/g to 105 J/g after the 200th cycle [47]. Ryu et al [45] observed that 2.9 wt% super-absorbent polymer (SAP) thickeners on SSD prevented phase separation for more than 300 cycles at energy storage capacity of 227 J/g on the first cycle. Gok and Paksoy [48] investigated the effect of gelation on SSD with polyacrylamide and gelatin gels and showed that with 10 wt% gelatin and polyacrylamide 113 J/g and 180 J/g of energy storage capacity can be achieved respectively.

Several other thickening mechanisms have also been reported in earlier studies. Li et al [49] investigated the effect of 2 wt% carboxyl methyl cellulose (CMC) and 5 wt% octyl phenol polyoxyethylene ether (OP-10) thickened SSD in 7 wt% expanded graphite (EG). They reported the initial energy storage capacity of 114 J/g with less than 9.16% degradation over 50 cycles using DSC analysis. Dong et al [50] reported that SSD with 9 wt% EG was able to achieve an energy storage capacity of 230 J/g in the initial cycle but reduced to 186 J/g after 500 cycles. Alkan et al [51] investigated the encapsulation of SSD in hydrophilic polyvinyl alcohol (PVA) to reduce phase separation, and reported an energy storage capacity of 248.7 J/g with 9 wt% PVA. Similarly, Zhang et al [52] showed that microencapsulated SSD in a silicon dioxide shell could achieve energy storage capacity of 125.6 J/g the initial cycle and then reduced to 100.9 J/g after 100 cycles. From this discussion, it is evident that most of the literature on thickening agents on salt hydrate composites were focused on preventing phase separation, either by addition of thickeners or by encapsulating the salt with polymers. There has been little or no discussion on rheological properties that can have profound impact on the thermodynamical behavior of the thickened salt hydrate PCMs. Rheological properties, such as viscosity, storage, and loss moduli, of PCM composites can drastically alter the stabilization, phase separation and supercooling in salt hydrates PCMs. Hence, there is an immediate need to fully understand the correlation between rheological properties to the fundamental mechanism of long-term stability and reliability of thickeners and stabilizers used in salt hydrate systems [41]. This will enable better PCM design, tunability, and performance enhancement.

For long term SSD performance, a superior stabilizing agent may be polyelectrolytes which stabilize particles in aqueous solutions via steric and/or electrostatic interactions. Low-cost polyelectrolytes are ubiquitous as additives in nanotechnology applications to stabilize nanoparticles in aqueous or organic solvents [53] . However, little research has been done on using this approach to obtain stability in salt hydrate PCMs including SSD. Recently, Li et al. [34] reported the stabilization of SSD using dextran sulfate sodium (DSS), a sulfonated polyelectrolyte which provided stability enhancement of the thermal properties of SSD up to 150 cycles. In the present work, we tested eight different additives as stabilizing materials to improve the long-term thermal energy storage stability of SSD. We develop a thorough understanding of the thickening and stabilization mechanisms by investigating the thermodynamic properties of the PCM mixtures containing SSD and one of the eight stabilizing agents. The thickeners investigated in this study are sodium polyacrylate (SPA) [54], cellulose nanofiber (CNF) [55], potassium polyacrylate (PPA) [56], hydroxyl ethyl cellulose (HEC) [57], carboxyl methyl cellulose (CMC) [58]; fumed silica [59], dextran sulfate sodium (DSS) [34] and poly(sodium 4-styrenesulfonate) (PSS) [60]. The structural and rheological properties of SSD with each thickener are investigated in detail. The correlation between rheological properties with the stabilization mechanisms are examined as a function of different thickening agents. It is observed that the rheological property changes due to the addition of additives affects the key thermodynamical characteristics of SSD, including cyclic stability, phase change temperature, and latent heat. This work provides a pathway to the design and selection of additives for improving the performance of salt hydrate PCMs in thermal energy storage applications.

2.2 Materials and Methods

The ACS reagent sodium sulfate decahydrate ($Na_2SO_4 \cdot 10H_2O$, SSD), was obtained from Sigma Aldrich. Table 2.1 illustrates all the different additives used in this study. All materials were utilized as received.

2.2.1 Sample Synthesis

To overcome the difficulties of phase separation in SSD, various mixtures were prepared by mixing SSD with the additives in a mass ratio 95.2:4.8 respectively. Due to the high sensitivity of SSD to relative humidity (RH), the samples were synthesized in a glove box with controlled

temperature (22 ^{o}C) and relative humidity (RH > 85%). Afterwards, the mixtures with thickeners were stirred vigorously to achieve miscibility at high viscosity and those containing polyelectrolyte additions were ultrasonicated (thin solution) while they were kept in a thermostatic water bath at 50 °C for 1 hour, until the SSD melted completely. The mixture was allowed to cool naturally to room temperature and stored in a sealed glass vial.

2.2.2 Characterization

2.2.2.1 Structural properties

X-Ray Diffraction Characterization: To determine the structure of the SSD-based mixtures, X-ray diffraction (XRD) was used. The XRD patterns of the SSD-based mixtures were studied using the PANalytical Empyrean XRD diffractometer to identify the crystal structure of the samples. The X-ray voltage was 45 kV and the tube current was 40 mA, with a Cu anode with a Kα of 1.54 Å. XRD data were collected at a scan rate of 1°/min over a 2θ range of 5° to 90°.

Attenuated total reflectance infrared spectroscopy (ATR-IR): To determine the chemical structure of the salt hydrate samples, their respective ATR-IR spectra were acquired with a PerkinElmer Frontier Fourier transform infrared (FTIR)/near-infrared (NIR) spectrometer equipped with a diamond ATR attachment and a spectral resolution of
2 cm^{-1} in the 4000–600 cm^{-1} range.

2.2.2.2 Thermal Properties

The thermophysical properties of the samples, including phase change temperature, latent heat, and supercooling were analyzed using a differential scanning calorimeter (DSC 2500, TA Instruments) with a 50 mL/min nitrogen purge. 10–20 mg of each sample was hermetically sealed in an aluminum DSC pan and thermally cycled between -40 and 50 °C at a ramp rate of 5 °C/min. The melting temperature and phase change enthalpy of the PCM samples were determined using the heating scans. Supercooling was determined by comparing the temperature at which freezing initiated during a cooling scan with the melting temperature determined from the preceding melting scan.

Table 2.1. Additives evaluated in this study for long-term stability enhancement of sodium sulfate decahydrate

Additive	Feature	Product	Manufacturer
Fumed silica (Si 200)	Particle size ~ 12 nm	Aerosil® 200	Evonik
Sodium polyacrylate (SPA)	Particle size ~ 90-850 μm	432784	Sigma Aldrich
Potassium polyacrylate (PPA)	≥99.5 purity	470302	Ward's Chemical
Carboxymethyl cellulose (CMC)	≥99.5 purity	Walocel	Dow Chemicals
Hydroxyethyl cellulose (HEC)	60% bio-based carbon	Cellosize	Dow Chemicals
Cellulose nanofiber (CNF)	Fiber width ~50nm	Freeze Dried	University of Maine
Dextran Sodium Sulfate (DSS)	M_W ~500,000; ≥98 purity	0198	VWR Chemicals
Poly(sodium 4-styrenesulfonate) (PSS)	M_W ~70000	243051	Sigma Aldrich

M_w – Molecular weight

2.2.2.3 Rheological properties

The rheological properties of the PCM were measured using a rotational rheometer (ARES-G2; TA Instruments), with a parallel plate geometry of 40 mm diameter. The molten PCM samples were loaded in between the plates with a gap of 1 mm. To avoid water evaporation from the samples, a solvent trap was used. The viscosity was measured as a function of shear rate from 0.1 to 100 s^{-1} and the samples were tested in shear rate-controlled mode at 40 °C. Amplitude sweep test was conducted to confirm the linear viscoelastic region at a constant angular frequency (1 Hz) and the range of strain was from 0.005% to 100%. The neat SSD and SSD-based mixtures were investigated with oscillatory tests, by measuring the storage (G') and loss (G'') moduli as a function of the frequency (0.1–10 Hz) at an applied fixed strain of 1%. During the measurement, the temperature was held constant at 40 ^{o}C to ensure the SSD remained melted. Also, a temperature ramp test was done in situ as the samples were subjected to a temperature ramp from 40 °C to 8 °C for two successive cycles to observe the change in the rheological properties of the samples during the thermal cycling test.

2.3 Results and Discussions

2.3.1 Phase stability of the modified PCMs

The effectiveness of the 8 different additives on the viscosity and miscibility of sodium sulfate decahydrate was visually inspected first as presented in Figure 2.1. Different thickeners exhibited different thickening efficiency (thin or thick) and compatibility with sodium and sulfate ions from the molten SSD (homogeneous or inhomogeneous). Based on visual observations, only samples with SPA, PPA, CNF, and DSS and PSS showed miscibility and resulted in a homogenous mixture. Therefore, we investigated only these 5 samples and pure SSD were further evaluated for the energy storage capacity, melting and freezing behavior in a DSC set-up.

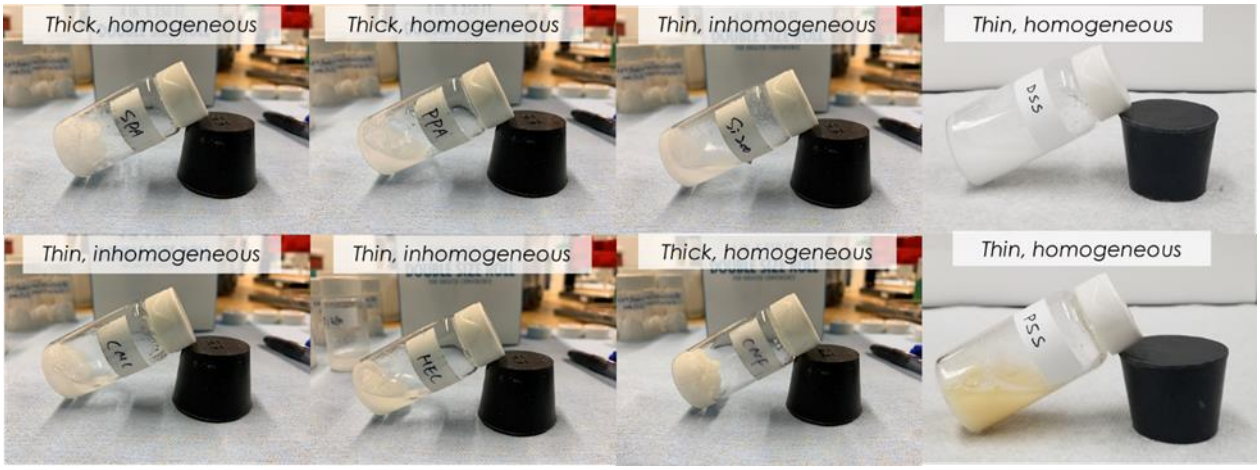


Figure 2.1. Visual inspection of viscosity and miscibility of sodium sulfate decahydrate with different thickeners and stabilizers.

2.3.2 Structural properties of the modified PCMs

2.3.2.1 XRD Characterization

The XRD patterns in Figure 2.2 show the crystalline structures of six different PCM samples. The pure SSD showed characteristic peaks at 2θ = 16.2°, 18.6°, 23.2°, 26.2°, 27.32º, 27.9°, 31.5°, 35.7°, and 43.1° [61]. The diffraction peaks of SSD at 16.2, 18.6, 27.32, and 27.9 degrees correlate to the crystal planes (200), (021), (131), and (104), respectively [62]. Furthermore, in all the diffractograms of the composite samples (Figure 2.2b-f), the peak intensities were lower than the intensity of pure SSD, this is due to the coating of the crystalline SSD by the negatively charged hydrogel films of SPA, and PPA, DSS, and PSS. The presence of crystalline peaks of pure SSD in the samples signifies that the interaction between SSD and the additives is a physical interaction, in particular electrostatic interactions, i.e., no chemical reaction occurs. The reduced intensity, broad peak in Figure 2.2d of SSD-CNF sample at 16.5°, and 22.6° suggests the appearance of reduced crystallinity and possible preferential crystal orientation of the mixture due to the long aspect ratio of CNF [63]. These peaks correspond to the (110), and (200) crystal planes, which were typical of cellulose type I structure [64]. The (110) and (200) crystal planes also represent the presence of both hydrophilic and hydrophobic surfaces in CNF [63].

2.3.2.2 ATR-IR Analysis

Figure 2.3 shows the ATR-IR spectra used to characterize the base material and PCM mixtures. Figure 2.3a displays the ATR-IR spectra of SPA polymer. The peak at 1170 cm^{-1} indicates the carboxylic stretching. C=O symmetric vibration and the -CH bending vibration is represented by 1404 and 1451 cm^{-1} peaks [65]. The peak at 1559 cm^{-1} corresponds to C=O anti-symmetric stretching, whereas the peak at 1702 cm^{-1} is C=O stretching. 2935 cm^{-1} is asymmetric -CH_2 bond stretching, whereas 3256 cm^{-1} is OH stretching [66]. Figure 2.3b shows the ATR-IR spectra of PPA polymer. The peaks at 1323 cm^{-1} and 3346 cm^{-1} are OH stretching vibrations, while the peaks at 1398 cm^{-1} and 1541 cm^{-1} are COO- radicals, showing the presence of an acrylate group [67]. The C=O and -CH_2 asymmetric stretching peaks occur at 1660 and 2941 cm^{-1}. Also, the multi-molecular interaction of H_2O causes the 3184 cm^{-1} absorption [68].

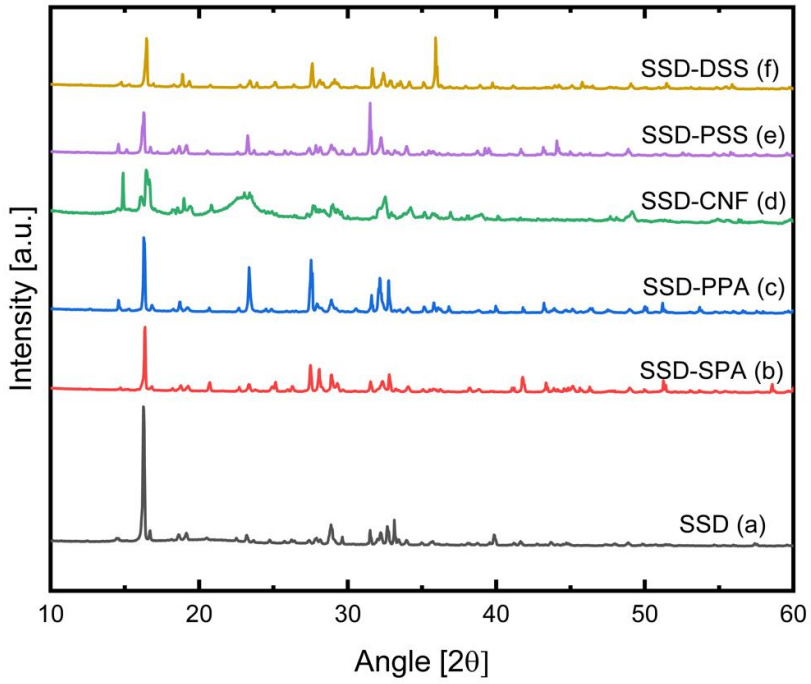


Figure 2.2. XRD Patterns of pure SSD, and SSD-based PCM mixtures.

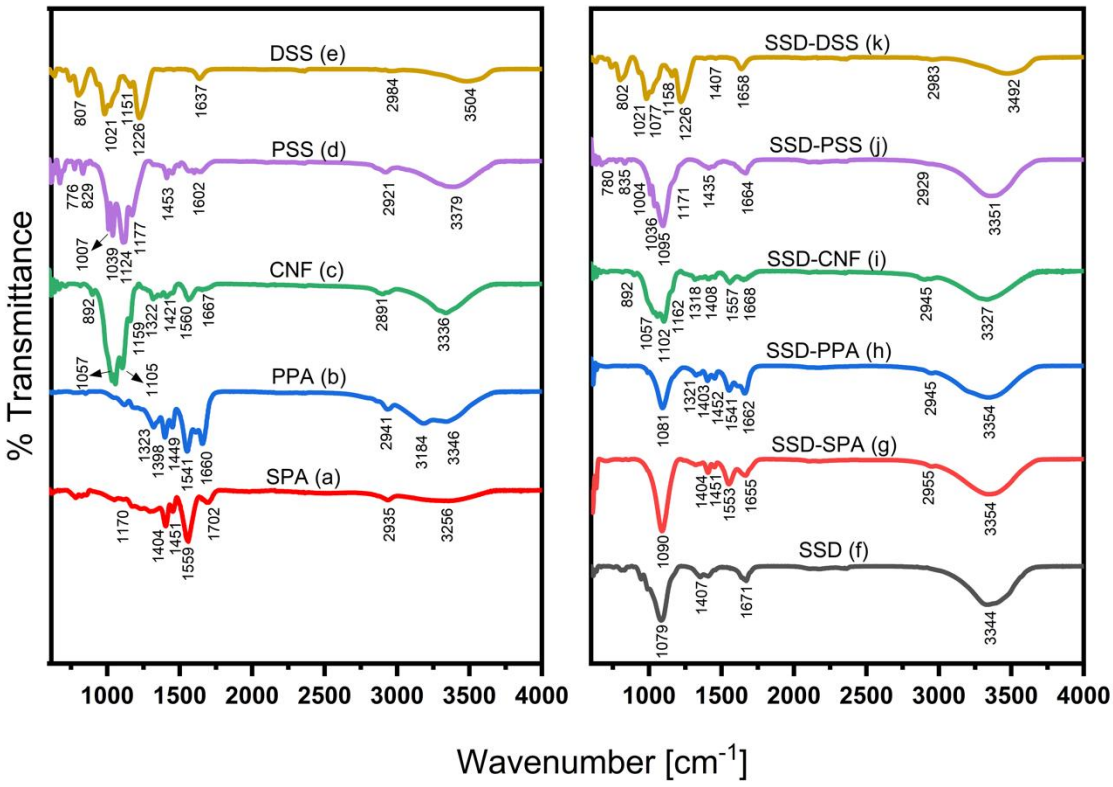


Figure 2.3. ATR-IR Spectra of additives and PCM mixtures (a) SPA (b) PPA (c) CNF (d) PSS (e) DSS (f) SSD (g) SSD-SPA (h) SSD-PPA (i) SSD-CNF (j) SSD-PSS (k) SSD-DSS

The peak at 892 cm^{-1} in CNF's ATR-IR spectrum (Figure 2.3c) is due to the β-glycosidic linkage in cellulose, while the peak at 1057 cm^{-1} is related to the C─O─C pyranose ring skeleton [69]. The absorbance at 1105 cm^{-1} is attributable to the glucose ring in cellulose, while the peak at 1159 cm^{-1} shows asymmetric stretching in C─O─C linkage [70]. CNF wagging symmetric bending and CH_2 asymmetric bending have maxima at 1322 cm^{-1} and 1421 cm^{-1}. The peak at 1560 cm^{-1} denotes the aromatic ring bond extension, while 2891 cm^{-1} is the CH stretching vibration. The peaks at 1667 cm^{-1} and 3336 cm^{-1} represent water stretching [71]. Figure 2.3d shows the PSS spectra; the absorption at 776 and 829 cm^{-1} is due to aromatic ring vibrations. 1007 cm^{-1} and 1039 cm^{-1} are S─O bond stretching peaks, whereas 1124 cm^{-1} and 1177 cm^{-1} are S bond stretching peaks [72]. 1453 cm^{-1}, 2921 cm^{-1}, and 1602 cm^{-1} are CH bending and C=C stretching peaks respectively [73]. The peak at 3379 cm^{-1} corresponds to H_2O moieties due to the hygroscopic nature of PSS [72]. Figure 2.3e displays the spectra of DSS; the peaks at 807 and 1021 cm^{-1} represent S─O─C, and C─O─C stretching vibrations of the pyranose ring, respectively [74]. The peaks 1151 cm^{-1} and 1226 cm^{-1} indicate the sulfate group and $─SO_3^-$ asymmetric vibration. 1637 cm^{-1} is the C─O─C deformation vibration, and 2984 cm^{-1} is C=H alkene stretching [75]. The peak at 3504 cm^{-1} represents the hydroxyl bonding. Figure 2.3f shows the spectrum of SSD. The peaks at 1079 and 1407 cm^{-1} represent the asymmetric and symmetric stretching vibrations of S─O in SO_4 [66]. The peaks at 1671 cm^{-1}, and 3344 cm^{-1} are ascribed to the bending vibration and stretching vibration of water. The respective base materials are well represented in the spectra of the composite materials as shown in Figure 2.3g-k without additional peaks. This further confirms the physical mixing of the baseline additive materials with SSD instead of new production formation due to chemical reaction.

2.3.3 Rheological properties of the modified PCMs

The rheological properties, flow behavior, viscosity, storage moduli (*G'*), and loss modulus (*G''*) of modified salt hydrate PCMs were measured to understand the effect of the various additives on the viscoelastic properties of the SSD salt.

2.3.3.1 Flow behavior

A flow sweep test was used to determine the influence of strain on the viscosity of the different mixtures as shown in Figure 2.4. For the pure SSD sample, the viscosity is relatively constant with

the strain rate, exhibiting Newtonian behavior. However, with the additives, shear thinning behavior was observed in the mixtures with SPA, PPA, CNF, and PSS. Viscosity follows the well-established power law as shown below in equation 2.1 [76]:

$$\eta = K\gamma^{n-1} \quad (2.1)$$

where η is the viscosity, K is the flow consistency index, γ is the strain rate, and n is the power-law index. Each individual viscosity data in Figure 4a is fitted with Equation 1, and the parameters are shown in Table 2.2. An 'n' value less than one represents the pseudoplastic and thixotropic nature of the mixtures. As can be seen that the power law index of $n < 1$, for all of the mixtures shown in Figure 2.4 (n values are listed in the figure legend), therefore, all of these PCM composites are pseudoplastic and thixotropic. As the shear rate increases viscosity decreases, the gel network in the polyacrylate based composite (red circles) slowly breaks down, leading to the further decrease in the viscosity [77]. For the CNF-based composite, the increase in the shearing of the material leads to the disintegration of the entangled fiber network thereby causing a reduction in the viscosity under continuous shearing [78].

Likewise, the PSS-based mixture undergoes a breakdown in structure, decreased viscosity, and flows in the direction of the strain under continuous increase in strain. Surprisingly, the viscosity of the DSS-modified sample (gold circles) was relatively greater than that of pure SSD and it exhibited Newtonian behavior, with constant viscosity value under increasing shear rate (Figure 2.4). The relatively smaller increase in viscosity signifies that the stabilization mechanism of the SSD mixture with DSS is likely not achieved by the same gel formation or network breaking mechanism as seen in SPA, PPA, and CNF-modified PCM composites, which change the behavior of the salt hydrate from Newtonian behavior to thixotropic behavior [34]. Considering the degree of non-Newtonian behavior of the mixtures, as the viscosity of the materials increases, the flow consistency index, K, increases. Also, as the shear thinning increases, the power law index decreases. Based on these, the degree of non-Newtonian characteristics of the PCM mixtures is categorized as SSD-CNF > SSD-SPA > SSD-PPA > SSD-PSS.

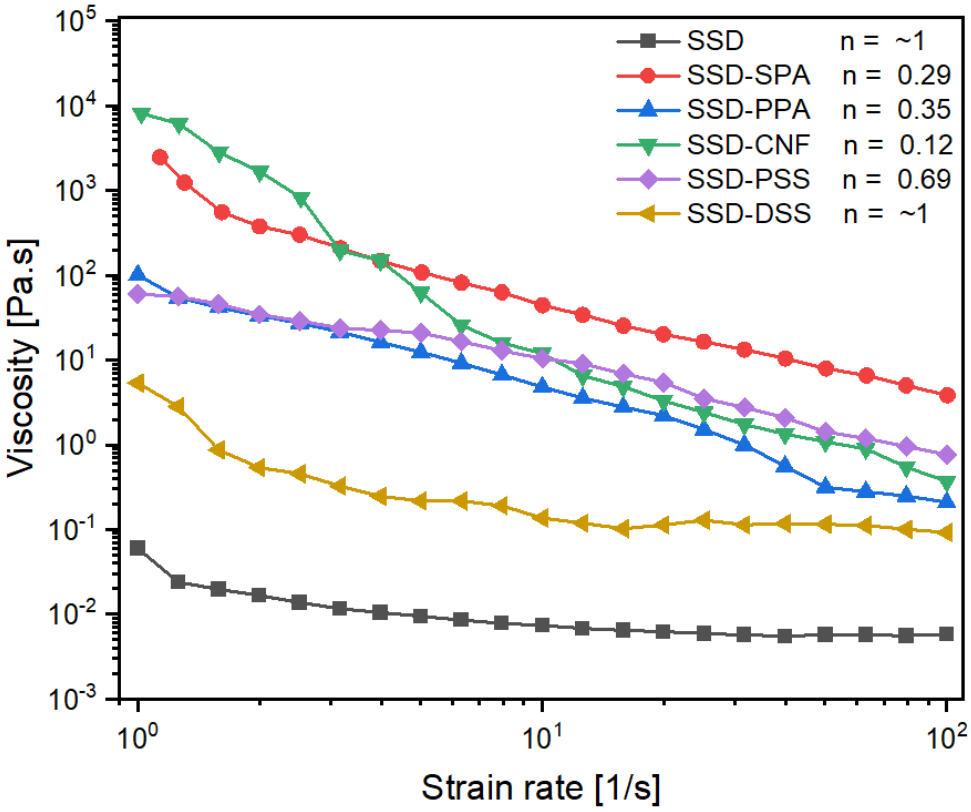


Figure 2.4. Flow test results of SSD and other SSD-based PCM mixtures

Table 2.2. Flow and Viscoelastic behaviors of the base material and PCM mixtures

Sample	Flow consistency index, K ($Pa.s^{n-1}$)	Power law index, n	Critical strain, γ_c (%)	G' at γ_c (MPa)	G" at γ_c (MPa)	Cross over strain (%)
SSD	0.02	~1	-	-	-	-
SSD-SPA	1120.60	0.607	0.2253	0.3552	0.2303	18.3073
SSD-PPA	96.90	0.650	0.1143	0.1993	0.0967	0.6442
SSD-CNF	1351.60	0.123	0.0467	2.7077	0.5073	0.3937
SSD-PSS	79.49	0.790	0.0714	1.5128	0.8277	0.6277
SSD-DSS	1.10	~1	0.1965	0.0297	0.0101	1.0016

2.3.3.2 Viscoelastic behavior

Oscillatory experiments at 40 ºC were performed to understand the viscoelastic behavior of SSD with various additives. Since material stability of PCMs is an important design parameter for targeted thermal energy storage applications, the storage (G') and loss modulus (G'') measurements could provide insight into the form stability of the PCM composites [79], as G' and G'' represent the solid- and liquid-like behaviors in amplitude and frequency sweep experiments shown in Figure 2.5a and Figure 2.5b. The critical strain, γ_c, at which the material begins to yield, which is the beginning of deviation from linear viscoelasticity, and the strain beyond which the material changes from solid-like behavior to liquid-like behavior ($G'' > G'$) is referred to as the cross-over strain. The critical stain is obtained by finding strain value of the intersection between the line drawn along the G' value at low strain values (where G' is almost constant) and the line drawn along the decreasing G' values at high strain values. This is demonstrated in the supplementary information.

The amplitude sweeps results for SSD and composites are illustrated in Figure 2.5a. Pure SSD experienced a monotonic decrease in G'' and G' even at low strain levels, and the loss modulus, G'' (outlined symbol) is higher than the storage modulus, G' (closed symbol), thereby confirming the liquid or melted state of pure SSD. Because of low G' and G" values of pure SSD, very low strain rate values are not obtained. Interestingly, the SSD-CNF composite exhibited the opposite behavior ($G' > G''$) indicating a solid-like behavior. However, the composite yielded at low strain level, $\gamma_c = 4.67 \times 10^{-2}$ before G' dropped rapidly. This might be attributed to the breakdown of the fibrillated cellulosic structure in the composite as observed earlier by Shel et al [80]. Furthermore, the relevant viscoelastic parameters including the critical strain (yield point of the material) and crossover strain (materials change from solid to liquid like behavior) of the mixtures are extracted from the amplitude sweep results as shown in Table 2.2. SSD-SPA showed the highest critical strain and crossover strain among the mixtures. This is due to the ability of SPA polymer chains to crosslink and form a strong polymeric network with the oppositely charged salt ions that does not yield easily [81]. This property can enable its use in forming a stable PCM matrix. With lower G' and G'' levels compared to the mixtures with other additives, SSD-DSS mixture has the second highest critical strain and cross-over strain.

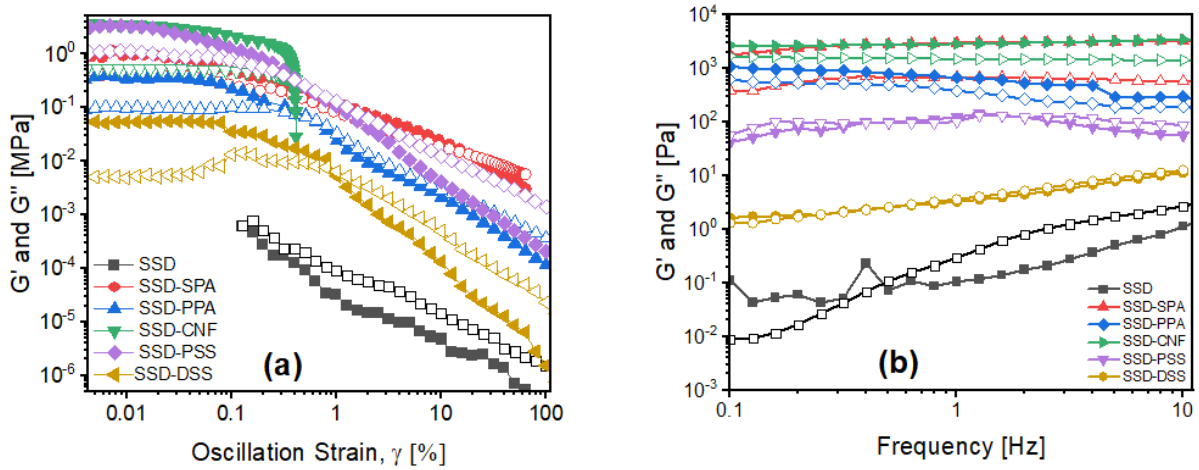


Figure 2.5. Rheological characterization of pure SSD and SSD-based PCM mixtures (a) Amplitude sweep test. (b) Frequency sweep test. [the solid symbols represent storage modulus (*G'*), while outlined symbols are used for the loss modulus (*G''*)].

SSD-PPA and SSD-PSS have intermediate G' values, but low critical strain and cross-over strain values compared to the mixtures with DSS and SPA. Figure 2.5b shows the frequency sweep *G'*, *G''* measurements of pure SSD and SSD with other additives. Mostly through the test frequency range, the storage modulus exhibits higher values than the loss modulus which represents a dominant viscous behavior. The increase in the *G'* and *G''* values of pure SSD with frequency corresponds to a well-known liquid-like relaxation behavior of the material [79]. However, other mixtures show hardly any change in the *G'* and *G''* values with frequency, which corresponds to linear viscoelastic behavior in the samples as consisten with the amplitude sweep test results (Figure 2.5a). Also, the *G'* values of the mixtures with polymeric additives (SSD-SPA, SSD-PPA, and SSD-CNF) are greater than the corresponding *G''* values over the test frequency range, signifying solid-like characteristics with elastic properties dominating over the viscous properties. In these polymeric systems, there is a formation of strong, interconnected polymeric network which restricts the movement of the polymer chains and the salt hydrate particles in the system, hence the frequency independent response [82].

2.3.3.3 Temperature ramp test

Utilizing rheology, the effect of PCM phase transition on rheological properties was evaluated to identify any potential changes that might occur through thermal cycling. To understand the effect of rheological properties on the phase transition of the PCM composites, three samples, pure SSD, SSD-DSS and SSD-SPA, were subjected to two thermal (heating and cooling) cycles between 8 – 40 °C as shown in Figure 5. It should be noted that the SSD-thickener mixtures have a nominal melting temperature of 32.4 °C. The materials were subjected to shear strain of 1% and frequency of 1Hz then the evolution of the complex viscosity was investigated. Figure 2.6a illustrates the change in complex viscosity of pure SSD between 8 and 40 °C. During the cooling step (40 °C – 8 °C), the complex viscosity of the pure salt hydrate PCM exhibited a remarkable increase. At 10 °C, and ~390 seconds, the value increased by more than five orders of magnitude. This increase is also illustrated by the sharp rise in the derivative of the complex viscosity, $\frac{d\eta}{dt}$. This suggests that at this temperature the material exhibited crystallization. However, there was an initial rise in the complex viscosity at the beginning of the heating step (8 – 40 °C), as opposed to a drop.

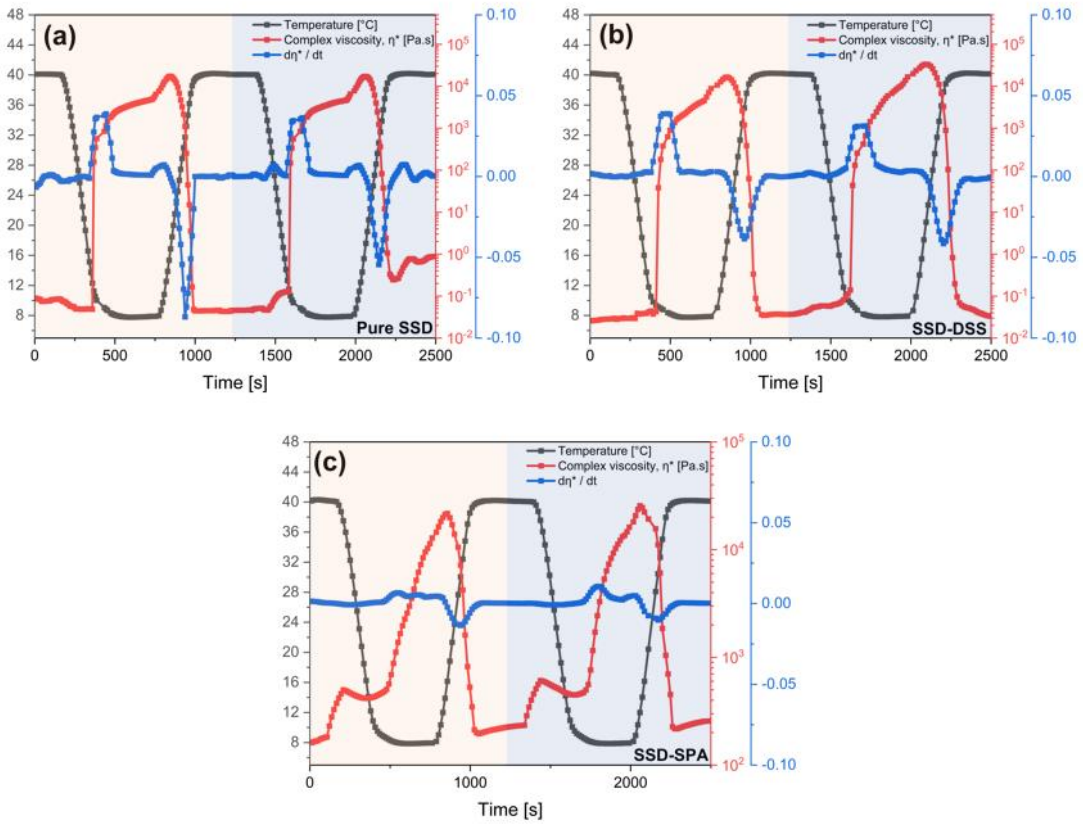


Figure 2.6. Change in complex viscosity over the temperature range of 8─40 °C during 2 cycles for (a) Pure SSD (b) SSD-DSS (c) SSD-SPA

A plausible explanation is that as oscillatory strains are applied during the freezing, there may be a tendency to break up the solid SSD particles as the freezing progresses and small particles (sub-cooled solid at 8 °C) of SSD could form. As higher temperatures are applied to the small SSD sample, initial melting will cause liquid to begin to flow into the subcooled particles, and refreezing between particles could lead to a greater overall stiffness, resulting in the increase in the complex viscosity. Continuously heating the material over its melting point resulted in a considerable reduction in complex viscosity. Also, in Figure 2.6b, the complex viscosity increased significantly when the SSD-DSS mixture was cooled from 40 °C to 8 °C, which corresponds to the rapid crystallization of the material during the cooling cycle. A change in complex viscosity of five orders of magnitude occurred at 10 °C, and ~450 seconds which is similar to pure SSD. In addition, the complex viscosity dropped proportionally when the material was heated above the melting point. This indicates that the addition of DSS does not affect the phase change temperature (PCT) and does not inhibit the rapid crystallization and release of stored energy in the PCM during discharge cycles. Figure 2.6c depicts the changes in the rheological characteristics of the SSD-SPA composite during sequential melt-freeze cycles.

Unlike pure SSD, the mixture did not exhibit a sharp transition when the material was cooled from 40 °C to 8 °C, as shown by the low magnitude of the derivative of the complex viscosity, $\frac{d\eta}{dt}$ when compared to pure SSD, and SSD-DSS. The sudden rise in viscosity at ~180s and ~1350s during the constant-temperature melting process can be attributed to the transient restructuring of the SPA polymer network after the melting of the SSD is completed. In addition, the change in complex viscosity was less than three orders of magnitude after maintaining the sample at 8 °C for an extended period of time. The smaller relative change in complex viscosity is due to the higher initial viscosity of the SSD-SPA in the melted state; the viscosity at the end of the freezing stage is very similar for all three materials. The sluggish dynamical behavior during freezing may be due to the high absorption rate and slow release of water needed for crystallization by highly hydrophilic SPA, thereby inhibiting crystallization and the proper release of energy stored in the material. The similar pattern is also found in other mixtures with polymeric thickeners, such as SSD-CNF (Supplementary information). From these discussion, it can be concluded that the thickening agents raise the viscosity of the salt hydrate PCMs substantially,

slow the diffusion of water in the sample and hence reduces the rate of freezing and heat release during the cooling cycles. In all cases, the two heating and cooling cycles are quite similar; this demonstrates the repeatability of the phase transition in PCMs, a requirement of stability of these materials [83].

2.3.4 Thermal properties of the modified PCMs

2.3.4.1 Comparing the influence of different additives on stabilizing sodium sulfate decahydrate

The influence of all five different additives on stabilizing sodium sulfate decahydrate were compared. The energy storage capacity (ESC) of pure SSD and the SSD mixtures was experimentally measured using differential scanning calorimetry (DSC) over 10 cycles shown in Figure 2.7a. The ESC of pure SSD (black curve) degraded by 38.4% (from 220 J/g to 135.44 J/g) after 10 cycles. The significant decrease in latent heat of pure SSD confirmed previous findings that pure SSD is not thermally stable salt [58], and hence additives/thickeners are required to stabilize the salt hydrate PCM.

A possible solution to decrease the phase separation and increase the thermal stability of SSD can be achieved by decreasing the diffusion length for the salt particles and limiting the settling rate of the anhydrous sodium sulfate in solution. Samples with sulfonated polyelectrolytes, DSS (gold curve), and PSS (violet curve) showed the most desirable performance with recovered energy capacity of 209.95 J/g and 183.99 J/g respectively. However, samples thickened with SPA, PPA, and CNF experienced a decline in ESC values to 132.16 J/g, 133.08 J/g, 130.47 J/g respectively, after 10 cycles.

The effective energy (E_{eff}) per unit mass of SSD was used to determine the efficacy of SSD in various mixtures and was defined as follows in Equation 2.2 [49]:

$$E_{eff} = \frac{\Delta H_{composite}}{\beta} \quad (2.2)$$

where $\Delta H_{composite}$ is the latent heat of composite/mixture; β represents the mass fraction of SSD in composites. Figure 2.7a shows that even after correcting the ESC in each mixture to the concentration of SSD, all samples with polymeric thickeners did not produce the desirable efficient energy per unit mass compared to the ESC of pure SSD, and also the E_{eff} value of the samples with sulfonated polyelectrolytes DSS and PSS are 220.54 J/g and 193.27 J/g respectively.

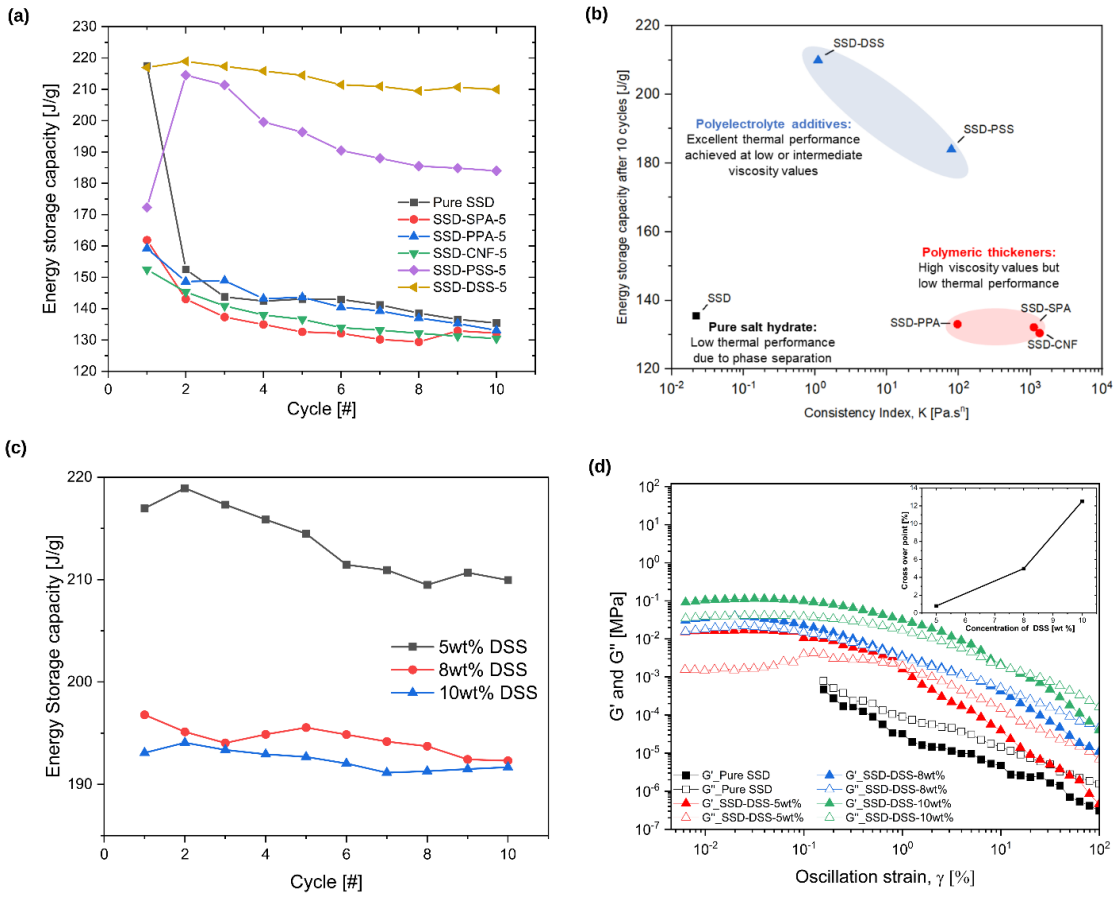


Figure 2.7. (a) Energy storage capacity (ESC) of pure sodium sulfate decahydrate (SSD) and SSD-based mixtures measured over 10 cycles (b) Comparison of thermal energy storage capacity vs viscosity values of SSD, and other mixtures after 10 cycles (c) ESC of SSD-DSS mixtures with various concentration of DSS over 10 cycles (d) Amplitude sweep test of pure SSD and SSD-DSS mixtures with various concentration of DSS. Inset plot shows increase in cross-over strain with corresponding increase in DSS concentration.

Table 2.3. Phase change properties of pure SSD, with different additives

Sample	Content of SSD, β (%)	Melting Temperature ([°C)	Energy storage capacity at 10th cycle (J/g)	Efficient energy per unit mass of SSD, E_{eff} (J/g)
SSD	100.0	32.92	135.44	135.44
SSD-SPA	95.2	34.14	132.16	138.82
SSD-PPA	95.2	32.80	133.08	139.79
SSD-CNF	95.2	35.78	130.47	137.05
SSD-PSS	95.2	34.13	183.99	193.27
SSD-DSS	95.2	34.99	209.95	220.54

The enhanced thermodynamic properties of DSS and PSS samples are due to the nature of DSS and PSS which are high molecular weight, water-soluble polyelectrolytes with numerous hydrophilic and negatively charged sulfonate groups that shows consistent rheological performances. Once these water-soluble polymers are dissolved in the SSD solution, it initiates an electrostatic interaction with SSD. The polyelectrolytes enclose the sodium sulfate particles and suspend them in the solution, thus reducing phase separation [34]. However, the degradation in energy storage capacity of the samples with thickeners (SPA, PPA, and CNF) may be due to the high ionic strength of solvated thickeners that creates imbalance in the electrostatic interactions resulting in weaker thermodynamic and rheological responses.

Also, thickened samples may diminish the rate of salt diffusion/solubility during the freezing process, hence lowering the ESC. Correlating the thermal performance to the flow consistency index, *K* of the materials obtained from the flow test as shown in Figure 2.7b, the polyelectrolyte-based PCM mixtures showed excellent thermal performance even at low viscosity values, whereas the polymeric thickened mixtures with high viscosity values all exhibited low thermal performance after 10 thermal cycles. Thus, we conclude that the physical thickening alone does not enhance the total energy storage capacity of SSD over the long run. Polyelectrolyte stabilization of SSD offers a new and promising technique for improving the thermal characteristics of SSD by electrostatic and possibly stearic mechanisms at low or intermediate viscosity.

To further understand the impact of increased concentration of DSS on the thermal and rheology performance of SSD, three concentration values of DSS, 5wt%, 8wt%, and 10wt% were added to SSD. As shown in Figure 2.7c, the increase in the concentration of DSS led to a corresponding decrease in the ESC with the ESC of 5wt.% DSS estimated as 213± 3.50 J/g as compared to 8wt% and 10wt % DSS with ESC of 194.39 ±1.37 J/g , and 192.38±0.99 J/g, respectively. The optimal concentration of DSS for higher thermal performance is 5wt%. Figure 2.7d exhibits the influence of DSS concentration on the viscoelastic behavior of the mixtures. The *G'* and *G"* values of the samples increased proportionally as the DSS concentration rose from 5wt% to 10wt%. In addition, the inset figure demonstrates a monotonic rise in cross-over strain as concentration increases.

2.3.4.2 Effect of dextran sulfate sodium salt on improving the stability of sodium sulfate decahydrate

In general, a desirable salt hydrate PCM must have a high thermal stability over repeated thermal cycling. However, this is lacking in SSD. The addition of DSS polyelectrolyte has provided a new approach to enhance the stability of SSD via polyelectrolyte stabilization. The possible stabilization mechanism is explained thus: the dissolution of DSS in aqueous solution of SSD leads to sodium cations dissociating from the DSS polyelectrolytes and the formation of negatively charged Dextran sulfate (DS) polyanions. The presence of DS polyanions results in a cloudy homogeneous solution as seen in Figure 2.1, which indicates that there is a reduction in SS particle settling rate and enhanced formation of a homogenous suspension. The formation of a homogenous suspension could be due to a significant electrostatic interaction between the SS particles and the DS polyanion that enables the eventual coating of the SS particles with the DS polyanions (Figure 2.8a), which lowers the settling rate of SS particles and keeps them suspended in the solution. Thereby resulting in increased thermal cycling stability of DSS-based PCM composite. To further understand the stabilization mechanism of DSS polyelectrolyte on the particle size of SSD, dynamic light scattering (DLS) which is a non-invasive method for determining the size of suspended particles and molecules was utilized to measure the suspended particle size of SSD and SSD-DSS systems. The particle size distribution of the materials system is usually depicted in a normal distribution. As seen in Figure 2.8b, pure SSD has a mean particle size of 31.611μm, but the SSD-DSS mixture has a mean particle size of 12.76μm (Figure 2.8c). This suggests that the addition of DSS resulted in a considerable decrease in the mean particle size of SSD. It appears that the DS polyanions served as an effective physical barrier to keep undissolved SS particles from forming big aggregates that would settle fast. Particle/aggregate size reduction and sample homogeneity resulted in DSS-modified PCM sample having a good thermal cycle stability. The stabilization mechanism based on DSS is further discussed in our recent publication [34].

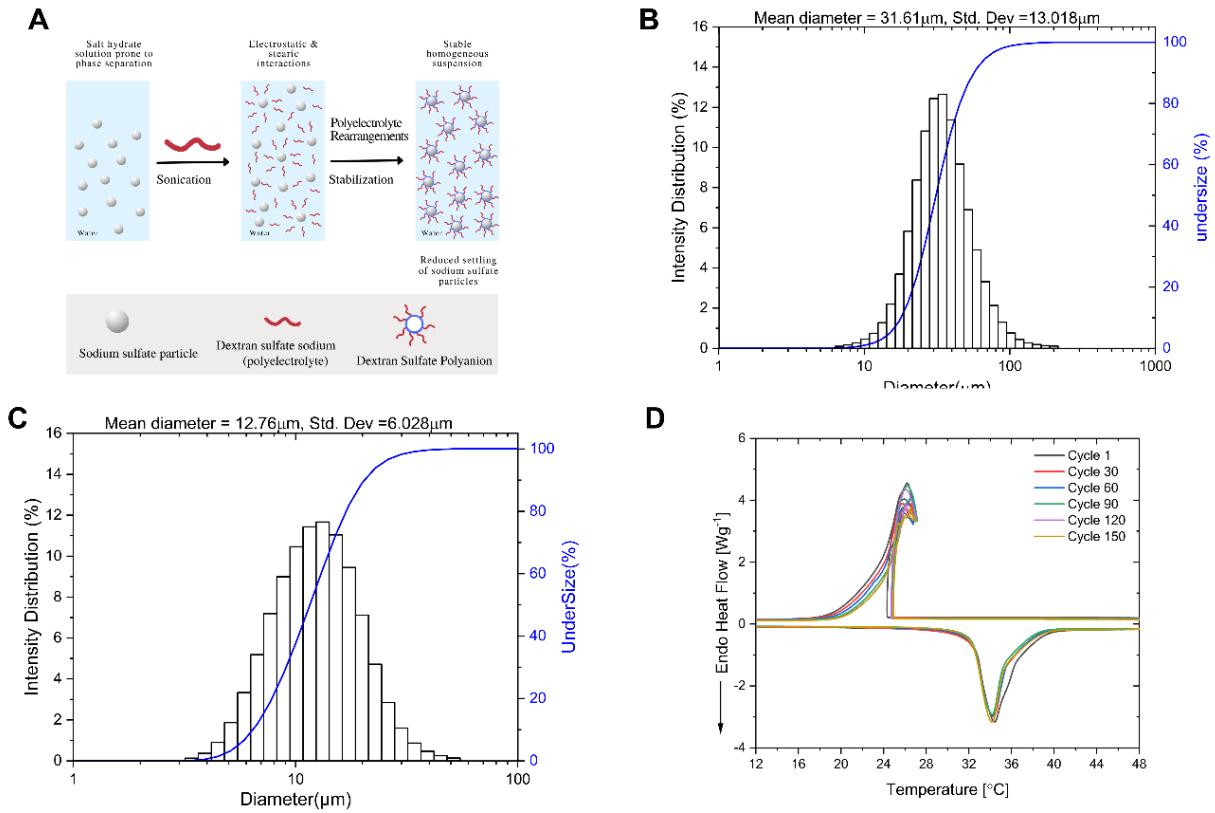


Figure 2.8. (a) Schematic illustration of the stabilization mechanism of DSS on SSD due to electrostatic interaction and possible stearic effect. Particle size distributions of (b) Pure SSD (c) SSD-DSS composite (d) DSC thermograms of SSD-DSS-Borax through 150 thermal cycling tests. The curves are identical from cycle 1 to cycle 50 indicating the thermal stability of the PCM composite.

Table 2.4. DSC Data for thermal cycling test of SSD-DSS-Borax composite

Cycle (#)	Melting			Freezing			Supercooling (°C)
	melting temperature (°C)	Mass enthalpy (J/g)	Enthalpy loss percentage (%)	Freezing temperature (°C)	Mass enthalpy (J/g)	Enthalpy loss percentage (%)	
1	34.15	189.31	-	25.34	176.23	-	8.81
10	34.04	179.04	5.42	25.74	168.92	4.15	8.30
20	34.01	179.39	5.24	25.80	170.13	3.46	8.21
30	34.01	180.27	4.78	25.83	170.73	3.12	8.18
40	33.88	179.84	5.00	25.63	172.43	2.16	8.25
50	33.89	180.04	4.90	25.90	173.10	1.78	7.99

2.3.4.3 Cyclic stability test of DSS-modified PCM composite

While phase separation is the major constraint on the widespread usage of SSD as a PCM, high degree of supercooling of salt hydrate-based PCMs is also major limitation which results in a variation of 25–40 °C or more in the freezing temperature of SSD relative to the typical melting point [46]. Based on the promising performance of SSD-DSS mixture, PCM composite based on SSD-DSS system was made by the addition of sodium tetraborate decahydrate ($Na_2B_4O_7 \cdot 10H_2O$, Borax) to decrease the degree of supercooling. The composite has SSD-DSS-Borax in a mass ratio of 90.8:4.6:4.6 respectively. The composition, energy storage capacity, and supercooling of the PCM composites are summarized in Table 2.4. It is critical to note that the energy storage capacities were measured using the DSC method, which enabled the evaluation of the thermal cycling stability of PCM samples in smaller quantities (10–20 mg).

Figure 2.8d illustrates the thermal cycling curves for up to 150 cycles. The 1st, 30th, 60th, 90th, 120th, and 150th cycles overlapped well, confirming the high thermal stability of the material. The SSD-DSS-Borax exhibited a steady melting point of 34.17 °C and energy storage capacity of 145.26 J/g after 150 cycles. This indicates that 77% of energy storage capacity was recovered after 150 cycles, the degradation in ESC is still minimal compared to the PCM mixtures with polymeric thickeners after repeated thermal cycles. Also, the addition of Borax drastically reduced supercooling to ~8°C. Although the freezing curves showed recalescence at the freezing peak. The level of recalescence can be reduced further by the use of fillers with high thermal conductivity, such as expanded graphite, which provide heat pathway and form a uniform heat flow in the PCM mixtures [84][85]. Due to the exceptional thermal stability of the SSD-DSS-Borax composite, it is a promising material for energy-efficient buildings and other thermal energy storage applications.

2.4 Summary

This work investigated the structural, thermal, and rheological behavior of SSD using different additives to improve its properties. Structural characterization using XRD and FTIR indicated no new phase after combining SSD with additives. Hence, it is confirmed that the mixing is a physical process without formation of new products in the PCM composite system. The rheological analyses showed that the polyelectrolyte additives do not significantly enhance the

viscosity of SSD compared to the polymeric thickeners, but they induce a viscoelastic effect when added to SSD to form polyelectrolyte based PCM composites. In addition, the temperature ramp tests demonstrate that the polyelectrolyte based PCM composites exhibit a comparable sharp and smooth crystallization as pure SSD. However, polymeric thickened PCMs samples undergo slow crystallization which is attributed to the poor temperature distribution and sluggish kinetics, in which hydrophilic thickeners limit the diffusion distance and compete with the salt for water required for the crystallization process. This may have a negative effect on the thermal cycling performance of PCM composites.

Thermal cycling results reveled that after 10 thermal cycles, polymeric thicker composites lost at least 40% of their energy storage capability. This shows that physical thickeners alone cannot prevent phase separation after repeated heat cycles. PCMs comprising DSS and PSS demonstrated good energy storage after 10 heat cycles with decreased phase separation. The thermal stability of the best-performing DSS-based PCM composites was tested via 150 melting-freezing cycles. Electrostatic interaction between DSS and SSD particles coats and suspends salt particles in solution, minimizing phase separation. DLS findings revealed that DSS decreased SSD particle size, which promoted the development of a stable homogeneous suspension that prevents phase separation and increases PCM thermal cycling performance for long-term energy storage applications. We have demonstrated that the physical thickening technique alone is insufficient to improve the long-term performance of SSD, thus we proposed a new path to thermal stability enhancement via electrostatic stabilization using polyelectrolyte additives with low or negligible thickening effect. The polyelectrolyte-based PCM composites could be beneficial in energy-efficient building applications.

CHAPTER 3

IDENTIFICATION OF STABILIZATION MECHANISMS IN SALT HYDRATE SYSTEMS BY DEXTRAN SULFATE SODIUM POLYELECTROLYTE

This section focuses on the identification of the stabilization mechanism of the most effective additive for stabilizing sodium sulfate decahydrate PCMs in Chapter 2. This work provides an explanation of the atomistic mechanism of stabilization of PCMs by dextran sulfate sodium polyelectrolyte, based on atomistic techniques such as neutron scattering and molecular dynamics simulations. The chapter is an article in preparation for submission to a journal.

Acknowledgements: This work was sponsored by the U. S. Department of Energy's Building Technologies Office under Contract No. DE-AC05-00OR22725 with UT-Battelle, LLC

Chapter Abstract

Sodium sulfate decahydrate (SSD) is a phase change material utilized in thermal energy storage applications, due to its inexpensive cost, large phase transition enthalpy and suitable temperature range for near-ambient applications. However, this material is plagued by phase separation leading to a considerable decrease in energy storage capacity over repeated thermal cycles. Sulfonated polyelectrolytes, such as dextran sulfate sodium (DSS), has shown great effectiveness in preventing phase separation in SSD. However, there is limited understanding of the stabilization mechanism at the atomic scale. This work investigates and provides an explanation on the stabilization mechanisms of SSD by DSS using two atomic scale techniques: neutron scattering pair distribution function analysis (PDF), and molecular dynamics (MD) simulations. Neutron scattering PDF reveal the structure evolution of the PCM samples below and above the phase change temperature. MD simulations revealed water that is part of the hydrate structure below the melting temperature leaves the hydrate crystal and enters the interfacial region between SSD and DSS. The water is stabilized at this interface by aggregating around the sulfonic acid groups attached to the backbone of the polyelectrolyte. This architecture retains water in close proximity to the dehydrated sodium sulfate, preventing phase separation and consequently stabilizing the rehydration of SSD. This work provides relevant insight in the selection and design of stable, and high-performing PCMs for applications in buildings, heating, and cooling applications.

3.1 Introduction

Energy is a critical component of scientific innovation and economic growth, which are necessary for the improvement of societies globally [86]. As non-renewable resources continue to be depleted and the global warming crisis worsens, the trend is shifting toward the usage of renewable energy sources [87][88]. Improvements in energy conversion and storage technologies are required to combat global energy challenges and reduce the effect of climate change. Currently, thermal energy storage systems are proving to be among the efficient means of storing energy for use in energy systems such as heating, ventilation, and air conditioning devices [89], solar energy storage[90], waste heat recovery [91], and power generation [92]. Phase Change Materials (PCMs), which are a type of thermal energy storage materials, have drawn the attention of many researchers due to their significant thermophysical features [9]. PCMs are particularly relevant in building applications because they can store and release energy in both the sensible and latent modes. This allows them to reduce heat flow between the building and the surrounding environment thereby leading to increased energy efficiency, flexibility, and load reduction of these thermal systems [13].

Sodium Sulfate Decahydrate (SSD), commonly known as Glauber's salt, is considered as a viable salt hydrate PCM for building system applications due to its low cost, high melting enthalpy, and suitable melting temperature [93][94]. In practice, the relevant phase change of SSD is a peritectic decomposition upon heating to yield anhydrous sodium sulfate salt and a saturated aqueous solution of Na_2SO_4 in water [95]. The irreversible phase separation occurs if the salt settles due to gravity, forming an inhomogeneous suspension. This phase separation behavior, which results in significant loss of latent heat during repeated thermal cycles, has prohibited the widespread application of SSD as a PCM [33]. Thus, minimizing phase separation in SSD, by preventing the bulk aggregation of anhydrous sodium sulfate salt, is critical for its broad adoption as a PCM for temperature control applications.

Various studies have reported the reduction of phase separation in SSD by gelling or thickening [96]. Gelling refers to incorporating a crosslinked substance (especially polymers) into the salt to form a network in which salt hydrate particles are embedded [97]. Thickening involves adding a substance to the salt hydrate that enhances its viscosity and prevents aggregation [98].

Numerous thickening and gelling agents, including attapulgite clay, micro/nano fibrillated cellulose, carboxymethyl cellulose, sodium alginate, hydroxyl ethyl cellulose, and polyacrylamide have been studied and examined [54][55][66][57]. However, the ionic strength of PCM salt solutions can severely impact the functionality of the thickeners [99]. Encapsulation of the PCMs is another proposed method to prevent phase separation [90][100][62]. However, the complexity and high cost of material preparation makes the approach less desirable [14]. Recently, Li et al. [34] reported a novel approach for the stabilization of SSD using polyelectrolyte. This was demonstrated using dextran sodium sulfate (DSS), a sulfonated polyelectrolyte that significantly improved the thermal characteristics of SSD over a 150-cycle period. Dextran sulfate sodium (DSS) is a polyelectrolyte derivative containing sodium sulfate groups (-OSO_3Na) on each repeating unit as demonstrated in Figure 3.1. It is hypothesized that DSS provides a possible electrostatic and stearic stabilization of SSD. This could be due to an electrostatic contact between the anhydrous salt particles and the DSS polyanion, which reduces the settling rate of sodium sulfate particles and maintains their suspension in solution. Also, DSS polyanions acted as a barrier, preventing undissolved anhydrous particles from aggregating, and settling rapidly [34].

Despite the extensive experimental research on PCM materials, particularly SSD, our understanding of the effect of these additives on the properties of SSD remains extremely limited at the molecular level. Sanker Deepa et al. [101] investigated the phase transition behavior of SSD in the presence of NaCl using molecular dynamics simulations. The study found that the progressive dissociation of water molecules from the salt molecule causes a phase change from hydrated to anhydrous salt across a temperature range. NaCl lowers the temperature at which phase transition occurs but increases the latent heat of melting. Results from this computational study show that when it comes to hydrated salts, hydrogen bonding capacity and ionic charge are the most important variables. So far, the atomistic mechanism of polyelectrolyte stabilization of SSD has not been reported in the literature. It is essential to acquire insight into the atomistic process behind the roles of these additives for better material design.

Herein, we investigated the atomistic mechanism of stabilization of SSD in the presence of DSS, using classical molecular dynamics (MD) simulations. Particular attention is paid to the redistribution of the water of hydration below and above the melting temperature. impact of polyelectrolyte addition on the structure and dynamics of SSD is investigated.

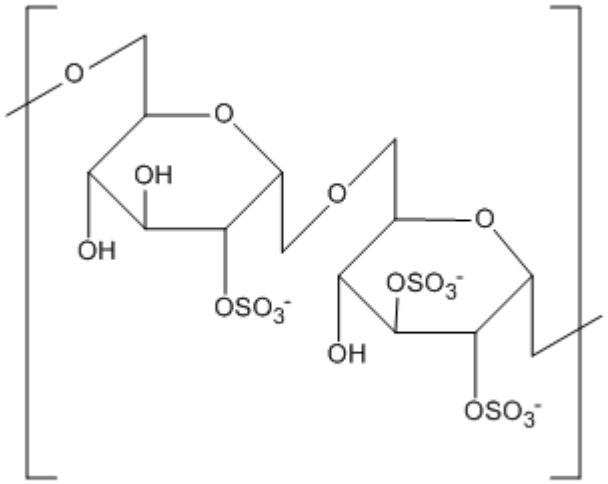


Figure 3.1. Molecular structure of dextran sulfate sodium polyelectrolyte

This work is significant because it could serve as a guide in the design and characterization of other relevant polyelectrolytes with SSD for various target applications.

3.2 Methods

3.2.1 Experimental setup

3.2.1.1 Materials preparation

As the hydrogen atom has a high incoherent scattering cross section, it was required to utilize the perdeuterated analogous salt hydrate to improve the signal-to-noise ratio of our diffraction measurements. Hence, anhydrous salt, Na_2SO_4 (Sigma Aldrich, ACS reagent, $\geq$ 99%), Deuterium oxide (D_2O) (Sigma Aldrich, 99 atom % D), and Dextran sulfate sodium polyelectrolyte (DSS) (Sigma Aldrich, M_r ~ 500000) were used to prepare the perdeuterated salt hydrate PCM mixtures. Na_2SO_4 and D_2O were mixed in appropriate weight ratio and stirred at 60 °C for 2 hours to obtain the perdeuterated salt hydrate. For the SSD-DSS mixture, 5 wt% DSS was added to the perdeuterated SSD and mixed using the same temperature and time as the perdeuterated salt hydrate.

3.2.1.2 Materials characterization

The phase change temperature of SSD was evaluated by subjecting the samples to a 50 mL/min nitrogen purge in a differential scanning calorimeter (DSC 2500, TA Instruments). Hermetically sealed aluminum DSC pans were used to conduct heat cycling between 233 K and 320 K on the sample weighing 10 to 20 mg. The phase change temperature of the PCM samples was determined using the heating scan.

To determine the nanoscale structure of the materials, two perdeuterated samples of based on pure SSD, and a mixture of SSD with DSS were analyzed using the Neutron Powder Diffraction (PDF) facility at the Spallation Neutron Source at Oak Ridge National Laboratory's Nanoscale-Ordered Materials Diffractometer (NOMAD) [102]. Neutron time-of-flight diffraction offers higher-resolution PDFs due to the greater Q range available, and neutrons are more sensitive to the light elements than X-rays [103]. Around 1.5 grams of the samples were loaded in a 6 mm V sample canister. As a final step before being loaded in the sample canister, the samples were melted. Diamond was utilized to calibrate NOMAD's detectors, while silicon was employed to create the first instrumental parameters. The scattering from the sample was normalized using a

solid vanadium rod, and the background for an empty 6 mm V sample canister was subtracted to get S(Q). Each sample was first cooled to room temperature and then ramped from 290 K to 330 K during which neutrons scans are collected. Neutrons scans were collected for 30 minutes at each temperature between 290 K and 330 K. Data analysis was done using the automated process available at NOMAD to obtain the PDF scattering data.

3.2.2 Molecular dynamics simulation set up and force field.

Classical molecular dynamics (MD) simulations were performed using the LAMMPS software [104]. These simulations require (i) stable initial configurations of all atoms and (ii) interaction potentials, which describe the potential energy and forces between all types of atoms included in the simulation. The initial structures of DSS was obtained from the literature [105] and an oligomer consisting of 12 monomers was constructed and relaxed using Avogadro [106]. The degree of sulfonation was two sulfonic acid groups per monomer. The polyelectrolyte melt was composed of 175 oligomers, resulting in 61,425 atoms. The melt was initialized with random orientations of the oligomers and equilibrated for 500 ps at 1000 K.

The crystal structure of SSD was determined using the crystallography datafile supplied by Kamburov et al. [46]. The unit cell was extended by 8 x 8 x 8 units, generating 75,776 atoms. The SSD was separately equilibrated in the NpT ensemble. Finally, the DSS molecules were placed adjacent to the SSD crystal in a monoclinic simulation box, based on the initial monoclinic crystal structure of SSD, extended in the [001] dimension to accommodate the melt. The combined system contains 137,201 atoms as shown in Figure 3.2a.

In a classical MD simulation, the interaction potential (sometimes called the force field) is an essential input. The choice of interaction potential depends upon the questions being asked and ultimately defines the physics contained within the model. For this system, a flexible model of the polymer, which includes all intramolecular degrees of freedom, including bond stretching, bond angles, dihedral torsion as well as non-bonded interactions, both of the Lennard-Jones type, and Coulombic interactions are required. For the DSS polyelectrolyte, the Dreiding potential was used. It is a generic force field that can provide an accurate forecast of the structures and dynamics of organic, biological, and main-group inorganic compounds [107].

For the interatomic potential of the SSD hydrate, simulations were performed with two different interaction potentials. First, the Dreiding potential was again used for SSD. Second, the

Gromos 54a7-FF potential for sodium and sulfate values [108] and an SPC/E model for the water molecules [109] was used. Both potentials employed a short-range cut-off of 12 Å and used the Ewald summation to evaluate long range electrostatic interactions in reciprocal space. Neither the Dreiding nor the Gromos potential were parameterized to capture the precise melt temperature of SSD. Therefore, simulations using both potentials turned out to be illustrative.

The two-phase simulation box was for SSD-DSS simulations used periodic boundary conditions in all directions, creating a infinite surface. Equilibration of the two-phase system was performed in the isobaric-isothermal (NpT) ensemble at one atmosphere to obtain the correct system density, using a Nosé-Hoover thermostat and barostat. The time step for the MD simulation was set at 1 fs. The thermostat and barostat damping parameters were 100 fs and 1000 fs, respectively. Equilibration of the two-phase system lasted 1.0 ns. Data production was performed in the canonical (NVT) ensemble. Data production lasted 0.5 ns. The results of four simulations are reported, which include two temperatures, 290 K (below melt temperature of 304.5 K) and 330 K (above melt temperature), using both the Dreiding and Gromos potentials. Snapshots of the equilibrated system at 290 K and 330 K are shown in Figure 3.2b and Figure 3.2c, respectively.

3.3 Results and Discussions

3.3.1 Thermal and structural properties of SSD and SSD-DSS obtained from experiment

The melting and freezing data of Pure SSD from the DSC experiment is shown in Figure 3.3a. The melting result showed that SSD undergoes phases transition at 305.48 K. This is consistent with the data reported in the literature [101][46]. The freezing data showed that SSD crystallized at a temperature of 270 K, which showed that the salt hydrate has high degree of supercooling. However, the phase transition temperature provides a guide for the temperature range selection considered for the experimental neutron scattering experiment and the MD simulations (290K, below melting point and 330 K, after melting point). The experimental neutron PDF data for SSD and the SSD-DSS mixture are shown in Figure 3.3b. The PDF data correlates relative atomic positions by assessing the probability of one atom's position with respect to neighboring atoms.

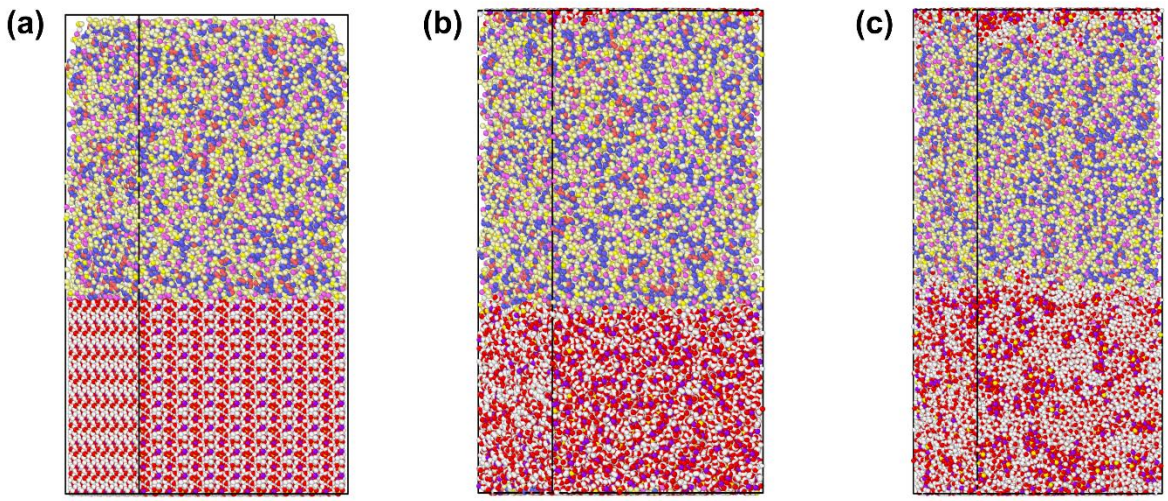


Figure 3.2. Simulation box snapshot (a) initial system with perfect crystal of SSD (bottom), (b) system at 290 K using the Gromos potential showing some degree of crystallinity, (c) system at 330 K using the Dreiding potential with loss of crystal structure in SSD. Color legend: (SSD – Yellow: S, Red: O, Purple: Na, White: H; DSS – Blue: H, Red: Carbon, Light Yellow: O, White: H, Deep Yellow: S, Pink: Na)

Each peak in the PDF data represents the atomic distance between the reference atom and other neighboring atoms. Because of this capability, the PDF could be used as a standard for determining the local atomic structure and configuration of materials [110], [111]. The PDF between atoms of type A and B, g(r), is defined as follows [112]:

$$g_{AB}(r) = \frac{1}{4\pi N_A r^2 \rho_B} \sum_{i=1}^{N_A} \sum_{j=1}^{N_B} \delta(r - r_{ij}) \tag{3.1}$$

where N_A is the total number of atoms of type A, ρ_B is the average number density of atom of type B, and r_{ij} is the distance between atoms i and j. The Dirac delta function, denoted as $\delta(r - r_{ij})$, has a value of unity when $r = r_{ij}$ and zero otherwise. The PDFs for any arbitrary AB atom type pair is only available from simulation. Experimentally, only a total PDF is accessible, in which all atoms are included, weighted by their neutron-scattering cross-sections.

In Figure 3.3b, the total PDF data for the pure SSD hydrate and the SSD-DSS hydrate-polyelectrolyte mixture are compared at 290 K. The purpose of this comparison is to demonstrate that the presence of DSS does not alter the structure of SSD at 290 K. The PDF data of the pure and mixture samples are very similar, which is expected since the SSD-DSS mixture contained 95 wt% SSD. The peak at 0.96 Å is correlated to the deuterium and oxygen bond distance in deuterated water. Furthermore, the peak at 1.57 Å is attributed to the sulfur-oxygen bond in the sulfate anion and the peak at 2.43 Å is correlated to the oxygen-oxygen distance in the sulfate anion.

In Figure 3.3c, the total PDF data for the pure SSD hydrate at 290 K and 333 K is compared. Peaks that correspond to covalent bonds remain at both temperatures, since the phase change does not correspond to the breakage of any chemical bonds. However, at the higher temperature, we observe significant loss of structure. From the combined DSC and PDF data, the loss of structure is inferred to be due to the loss of water coordination in the crystalline hydrate. In Figure 3.3d, the PDF data for the SSD-DSS mixture at 290 K and 333 K is compared.

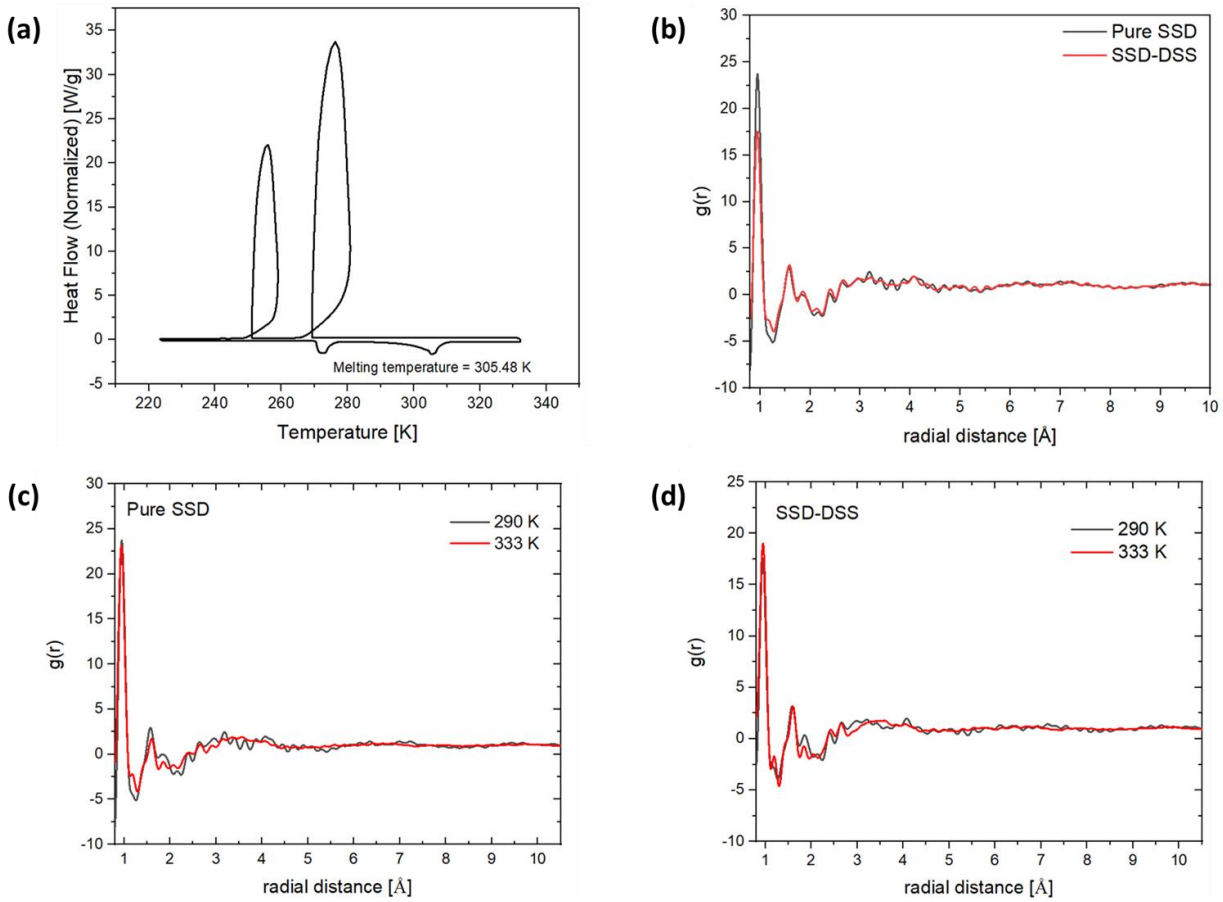


Figure 3.3. (a) DSC plot showing the melting and freezing temperatures of SSD (b) Neutron PDF data for SSD and SSD-DSS mixture obtained from NOMAD at 290 K (c) PDF data for SSD at 290 K, and 333 K (d) PDF data for SSD-DSS mixture at 290 K and 333 K

The primary purpose of showing the scattering data for the mixture is to demonstrate the similarity with that of the pure system. The presence of the polyelectrolyte has a nominal impact on the structure of the hydrate both below and above the melting temperature.

3.3.2 Atomic structure of SSD from MD simulation

To understand the structure and dynamical properties of the salt hydrate-polyelectrolyte system, the PDFs were obtained and processed from the MD simulations. First, we reproduced the total RDFs of the system at 290 K and 330 K are reported in Figure 3.4. The peaks observed in the total RDFs of the experiment for SSD-DSS mixture around 1 Å, 1.65 Å, and 3.5 Å (Figure 3.3) are also noticeable in the total RDF of the simulations. However, the peak intensity was more pronounced at 290 K compared to the 330 K, due to the loss in crystallinity with increase in temperature. Since the total RDF does not provide insight into the contributions of each atomic specie in the system, we decomposed the RDFs and compared the atomic structure of SSD salt hydrate at 290 K and 330 K based on the Dreiding potential and the Gromos potential as shown in Figure 3.5. To confirm the level of crystallinity of the salt hydrate at 290 K, the sulfur-sulfur atomic distances were plotted as shown in Figure 3.5a. To be clear, the only sulfur included in this calculation were those of the hydrate, as designated by the symbol, S_h. Also, note that the PDFs generated from MD simulation are reported to longer distances than was done for the experimental data, because from the atom specific contributions to the PDF, certain features are evident that are washed out or harder to identify in the total PDF. The S_h-S_h PDF data based on the Gromos potential showed notable sharp peaks with a notable peak at 9.55 Å, corresponding to the spacing of adjacent S atoms in the SSD hydrate unit cell.

However, the S_h-S_h PDF based on the Dreiding potential shows much less crystallinity. As noted above, neither interaction potential was developed to reproduce the SSD crystal structure or its melt temperature. It appears that the Gromos potential does a better job of retaining the SSD crystal structure at 290 K. In Figure 3.5b, the PDF of oxygen-oxygen atomic distances are shown. The only oxygen atoms used in this calculation are those in the water of hydration and are designated, O_h. Oxygen atoms in the sulfonate group or in the polyelectrolyte are not included in Figure 3.5b. The O_h-O_h PDF generated from simulations using the Gromos potential clearly show more features of crystallinity, particularly the shoulders on both sides of the first peak.

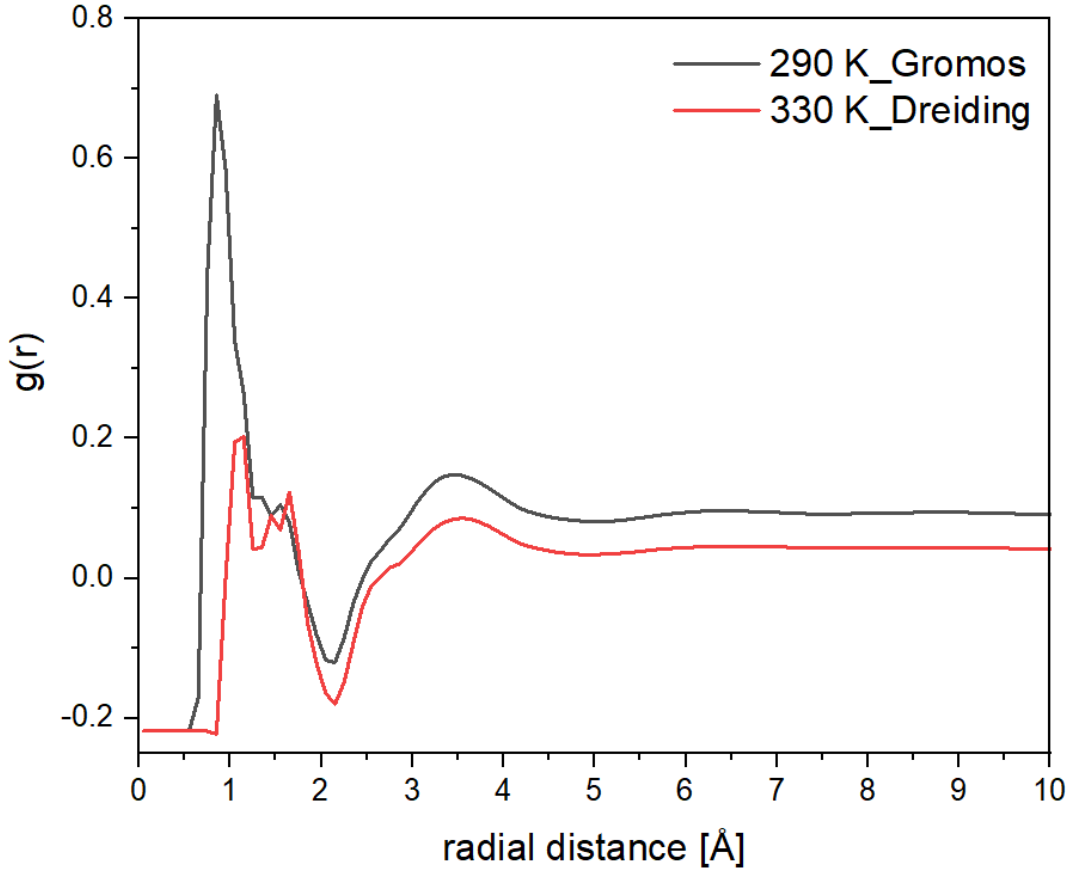


Figure 3.4. PDF data for SSD─DSS mixture obtained from MD simulations for Dreiding at 290 K, and Gromos at 330 K.

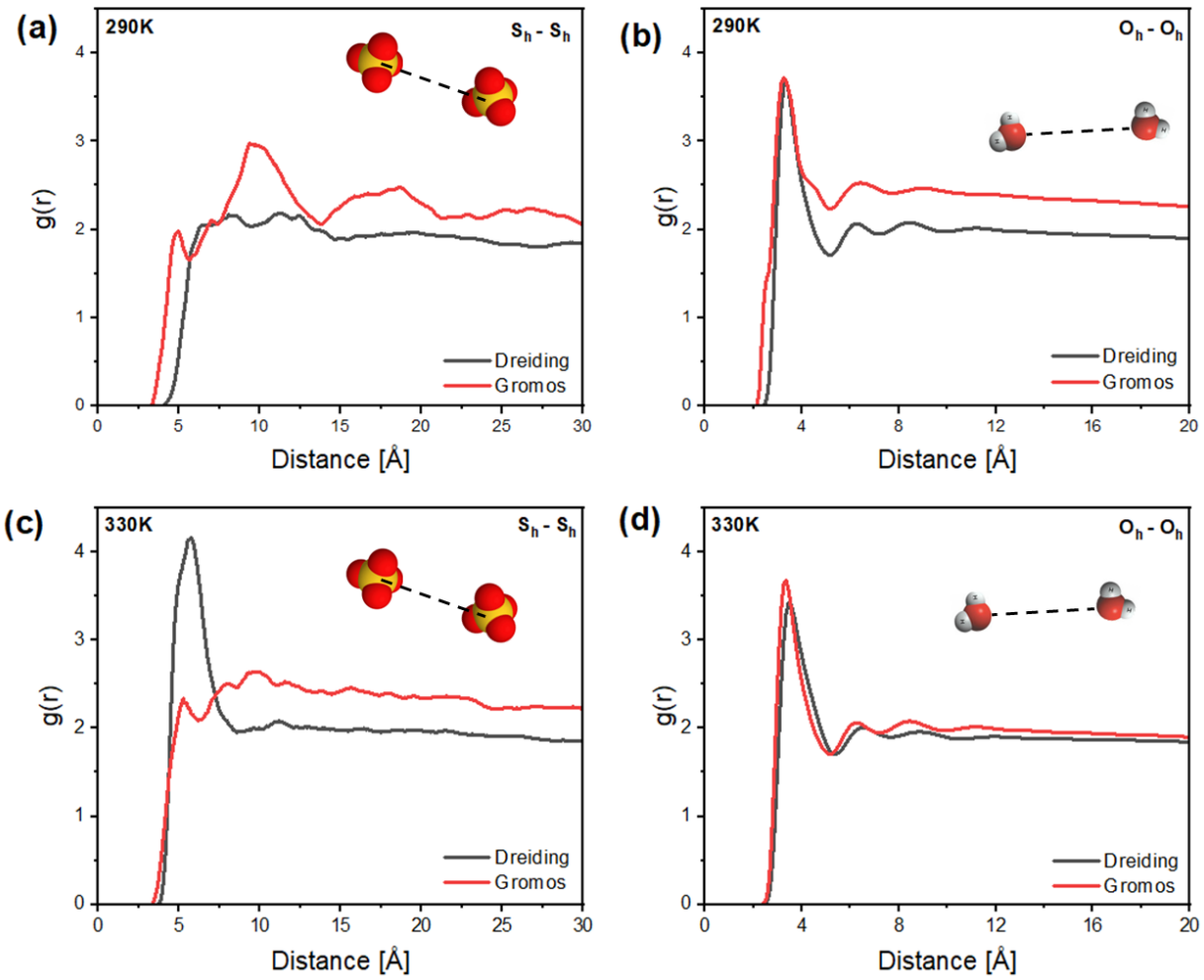


Figure 3.5. Simulated PDF Data for SSD using two different potentials. (a) S_h-S_h PDF at 290 K (b) O_h-O_h PDF at 290 K; (c) S_h-S_h PDF at 330 K; (d) O_h-O_h PDF at 330 K. The symbol, S_h, corresponds to sulfur atoms in the hydrate. The symbol, O_h, corresponds to oxygen atoms in the water of hydration.

The O_h-O_h PDF generated from simulations using the Dreiding potential shows a much more liquid-like structure. In Figure 3.5c, the S_h-S_h PDFs for simulation at 330 K for both potentials are shown. By comparing the S_h-S_h PDFs for the Gromos potential at 290 K (Figure 3.5a) and 330 K (Figure 3.5c), one can see that the crystallite has lost much of its structure but has not completed the phase transformation structure. On the other hand, the S_h-S_h PDF for the Dreiding potential shows an almost completely liquid-like state at 330 K. The O_h-O_h PDFs at 330 K, shown in Figure 3.5d corroborate this observation.

Based on this observation, we conclude that the Gromos potential does a better job of capturing the SSD hydrate structure at 290 K and the Dreiding potential does a better job of describing the disordered SSD liquid at 330 K. Neither potential captures the 304.5 K phase transition temperature perfectly. In classical MD, simulations reflect the goodness of the interaction potential. In this case, we are compelled to use two different interaction potentials to describe the SSD phases below (Gromos) and above (Dreiding) the melt temperature. For the practiced eye, accustomed to looking at PDFs, one may note that these PDFs do not approach the asymptote of unity at long distances. The difference in asymptote arises because the simulation system is a two-phase system and the hydrate occupies only approximately half of the simulation volume, which skews the normalizing density in equation (3.1).

3.3.3 Role of Dextran sulfate sodium

To understand the stabilization mechanism of DSS on SSD, it is important to investigate the interaction between the atoms present in the two components in the simulation box, especially at the interface between SSD and DSS. To describe these interactions, the PDFs were generated involving the sulfur atom of the sulfonic acid group on the polyelectrolyte, designated, S_p, and oxygen atoms in the backbone of the polyelectrolyte, designated O_p. The S_p-O_h PDF characterizes the aggregation of the water of hydration, O_h, with the polyelectrolyte sulfonic acid group. The O_p-O_h PDF characterizes the potential aggregation of the water of hydration, O_h, with the polyelectrolyte backbone. The S_p-S_h PDF characterizes the aggregation of the hydrate sulfur, S_h, with the polyelectrolyte sulfonic acid group, S_p. These three PDFs are shown in Figure 3.6 for simulations at both 290 K and 350 K, using both the Gromos and Dreiding potentials. In these figures the Gromos simulation at 290 K represents the best model of SSD in the solid hydrate phase and the Dreiding simulation at 330 K represents the best model of liquid SSD.

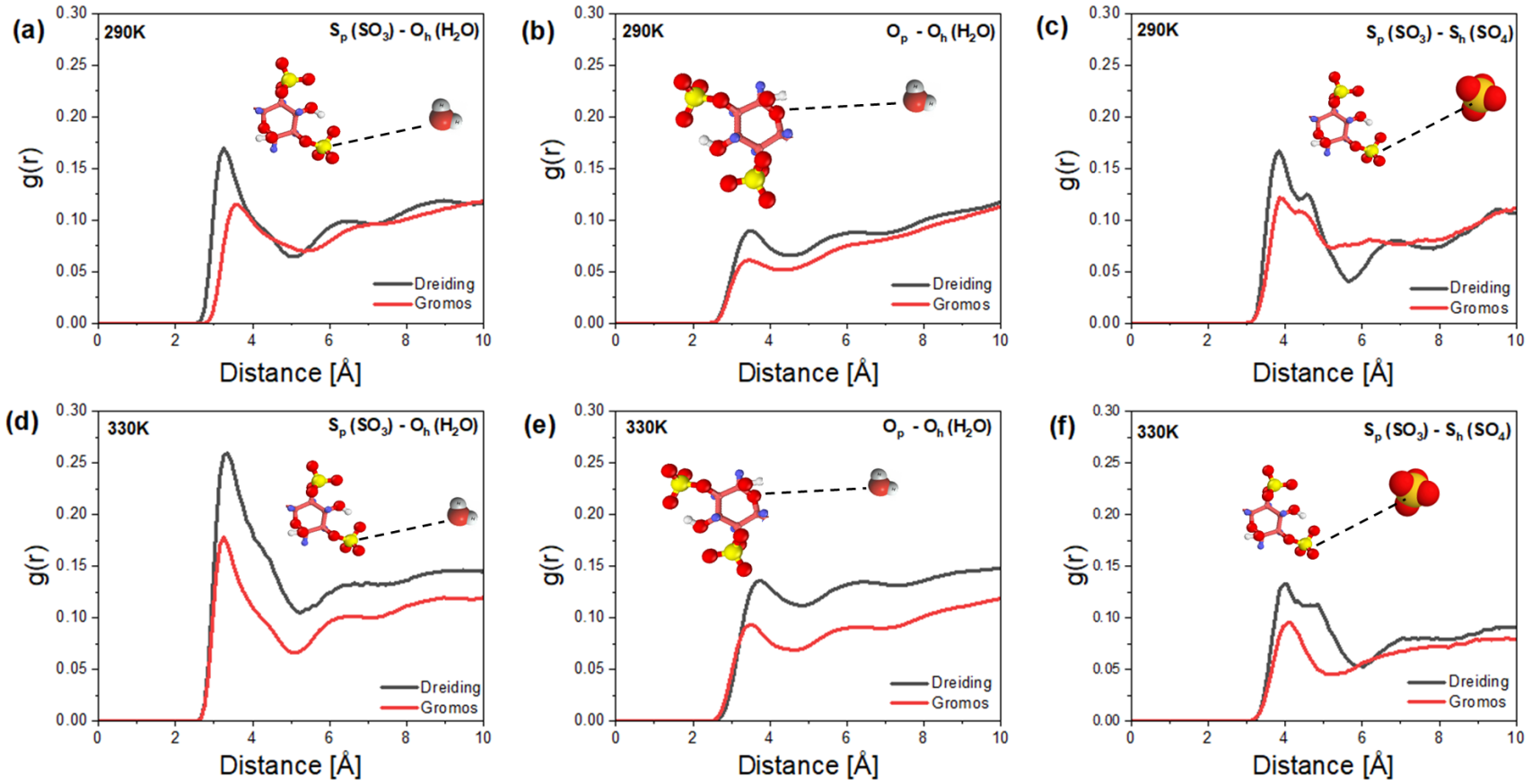


Figure 3.6. PDF Data illustrating the interaction of atoms in the polyelectrolyte and salt hydrate (a) S_p-O_h at 290 K (b) O_p-O_h at 290 K (c) S_p-S_h at 290 K (d) S_p-O_h at 330 K (e) O_p-O_h at 330 K (f) S_p-S_h at 330 K. Subscript h represents the atoms in the salt hydrate while p represents the atoms in the polyelectrolytes.

In Figure 3.6a, and 3.5d, the S_p-O_h PDF is shown at 290 K and 330 K respectively. Two consequences of these PDFs are immediately clear. First, at both temperatures, the more liquid-like state described by the Dreiding potential predicts significantly more water aggregation around the sulfonic acid group of the polyelectrolyte. Second, for both potentials, as the temperature increases, the amount of water around the sulfonic acid group increases. A more detailed inspection shows that at 290 K, the water molecules cluster around sulfonic acid group at 3.25 Å. The second hydration layer was around 6.25 Å at 290 K, as revealed by the Dreiding potential; some offset of 3.65 Å, and 6.95 Å was observed with the Gromos potential. Interestingly at 330 K, the PDF peak intensity increased in the intensity as shown in Figure 3.6d. This information paints a picture of water leaving the dissolved hydrate and entering into the interface between the SSD and DSS. However, the water does not diffuse deeply into the polyelectrolyte. It remains near the interface and aggregates around the sulfonic acid groups. The observation of localized aqueous domains centered on sulfonic acid groups tethered to polymer backbones is not new. In fact, the atomic-scale distribution of water in Nafion fuel cell membranes, is described by aggregation of water molecules around the sulfonic acid groups tethered by sidechains to the polymer backbone. See, for example, Cui et al. [103].

In Figure 3.6b and 3.5e, the O_p-O_h PDF is shown at 290 K and 330 K respectively. As was the case for the sulfonic acid group, the Dreiding potential shows more water around the O in the polyelectrolyte backbone compared to the Gromos potential, and the amount of water increases with temperature, as the hydrate becomes less stable. However, the extent of increase in water with temperature is less than that observed around the sulfonic acid group, indicating that the highly polar acid groups provide better electrostatic anchors around which water preferentially aggregates. In Figure 3.6c and 3.5f, the S_p-S_h PDF is shown at 290 K and 330 K respectively. Interestingly, we do not observe aggregation of sulfur from the hydrate sulfate and the polyelectrolyte sulfonic acid group with increasing temperature. Rather, the degree of association diminishes with temperature. It appears that the redistribution of the water of hydration forms a thin film between the sulfate anions and the sulfonic acid groups.

It is important to state that the concentration ratio of the polyelectrolyte and salt hydrate in the MD simulation system is 50:50. With adequate quantity of DSS in the PCM composite, phase separation was mitigated by the polyelectrolyte which keeps water of hydration in aqueous

domain. However, Li et al[113] showed that the presence of 5 wt% DSS in the PCM composite was not able to fully mitigate phase separation in SSD; this could be because the polyelectrolyte was saturated with the water of hydration with inadequate electrostatic effect to keep them in domain. This could reconcile the observation from the simulation and experiment.

3.3.4 Interfacial thickness and mobility characterization

To characterize the structure at the interface between SSD and DSS, relevant interfacial parameters were calculated using the distribution of the oxygen atom in the hydrating water, O_h, along the axis normal to the plane of the interface in simulation. The resulting water density profile is shown in Figure 3.7. The most immediate observation from this plot is the significant difference in the amount of water in the more solid-like SSD (Gromos) compared to the more liquid-like SSD (Dreiding). The solid SSD has a higher plateau of water density. In the liquid SSD, that water has clearly moved to the interface between SSD and DSS. In both cases the ability for water to penetrate into the DSS is very limited. The difference in the water density as a function of temperature is slight, but the Dreiding potential in particular shows that in the liquid state, more water moves to the interface with increasing temperature. This observation is consistent with the notion of a water of hydration forming a local film between the SSD and DSS, which is stabilized by aggregating around the sulfonic acid groups present at the interface.

The interfacial thickness can be determined by fitting the density profile to a functional form of the hyperbolic tangent [114]:

$$D_i\,(\mathrm{z}) \;=\; 0.5\,D_{i,bulk}\left[\frac{1-\;2\tanh(\mathrm{z}-z_0)}{d}\right] \tag{3.2}$$

where $D_{i,bulk}$ is the parameter related to the bulk plateau density, z_0 is the position of the Gibbs dividing surface, and d is the interfacial thickness. The interfacial fitting results are reported in Table 3.1. The parameter related to the interfacial thickness, d showed a higher value in all the cases for the liquid-like state compared to the solid-like state. The thickness of the water film can be estimated by examining the change in the position of the Gibbs dividing surface between the solid-like and liquid-like simulations. This thickness is nominally 1 nm.

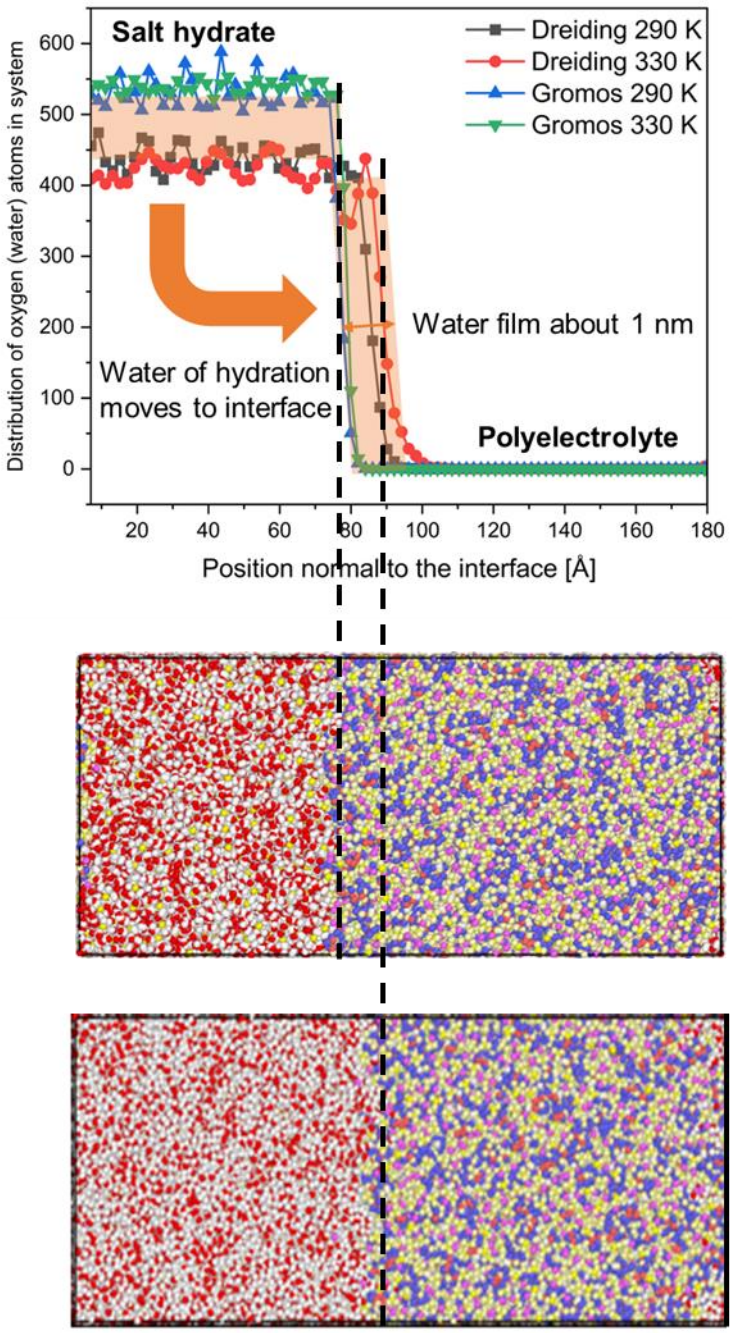


Figure 3.7. Distribution of oxygen atoms (water) along position normal to the interface. Water of hydration migrates towards the DSS polyelectrolyte and forms an aqueous film of 1nm.

Table 3.1. Interfacial parameters for the oxygen atoms in SSD

Force Field	Temperature	D_i	Z_0	t
Dreiding	290 K	218.47	85.63	6.64
	330 K	208.67	89.43	7.14
Gromos	290 K	263.72	77.23	4.70
	330 K	261.90	78.94	3.21

The mobility of atoms can be explored by calculating the mean square displacement (MSD). The MSD is relevant in the determination of the transport and diffusion characteristics of materials system [115]. The MSD in an equilibrium system is usually constant, thus we can get it by averaging the position data. Over time, this may be used to calculate how far the particle's position has moved from its initial reference point according to the equation [116]:

$$MSD_A(\tau) = \langle |\vec{r}_i(t+\tau) - \vec{r}_i(t)|^2 \rangle \quad (3.3)$$

The MSD of atoms of type A is an auto-correlation function of the elapsed time, τ, and is based on the position of all atoms of type A. The angled brackets in equation (3.3.) represent an ensemble average of all atoms, i, of type A and all time origins, t.

The MSD is plotted in Figure 3.8. We observed that the MSD increases with temperature. However, magnitude of the ultimate MSD is less than 1.5 $Å^2$. Ultimately, the water molecules on average have not moved any significant distance. This observation is consistent with a simulation where the water molecules do not diffuse deep into the surrounding polyelectrolyte. It is a result consistent with the density profile shown above. Of note, the MSD is traditionally used to generate self-diffusivities via the Einstein relation. In this simulation, the Einstein relation is not used to calculate diffusion coefficients because it is valid only in a long-time limit, and the very small values of the MSD reported here do not correspond to this limit.

3.3.5 Energetics.

In an effort to understand the thermodynamics of the phase change, we decomposed the non-bonded contributions (i.e. Lennard Jones and Coulombic terms) of the potential energy into three parts: interactions between atoms in the hydrate with other atoms in the hydrate (H-H), atoms in the hydrate with atoms in the polyelectrolyte (H-P) and atoms in the polyelectrolyte with other atoms in the polyelectrolyte (P-P). In Table 3.2., we report the difference in each of these contributions between the simulations at 330 K and those at 290 K. Note that the sum of the three components does not sum to the total because the three components included only non-bonded interactions, whereas the total includes both non-bonded and bonded interactions. We observe that the total potential system potential energy, which includes both bonded and non-bonded interactions, increases with temperature in the simulation using the Gromos potential.

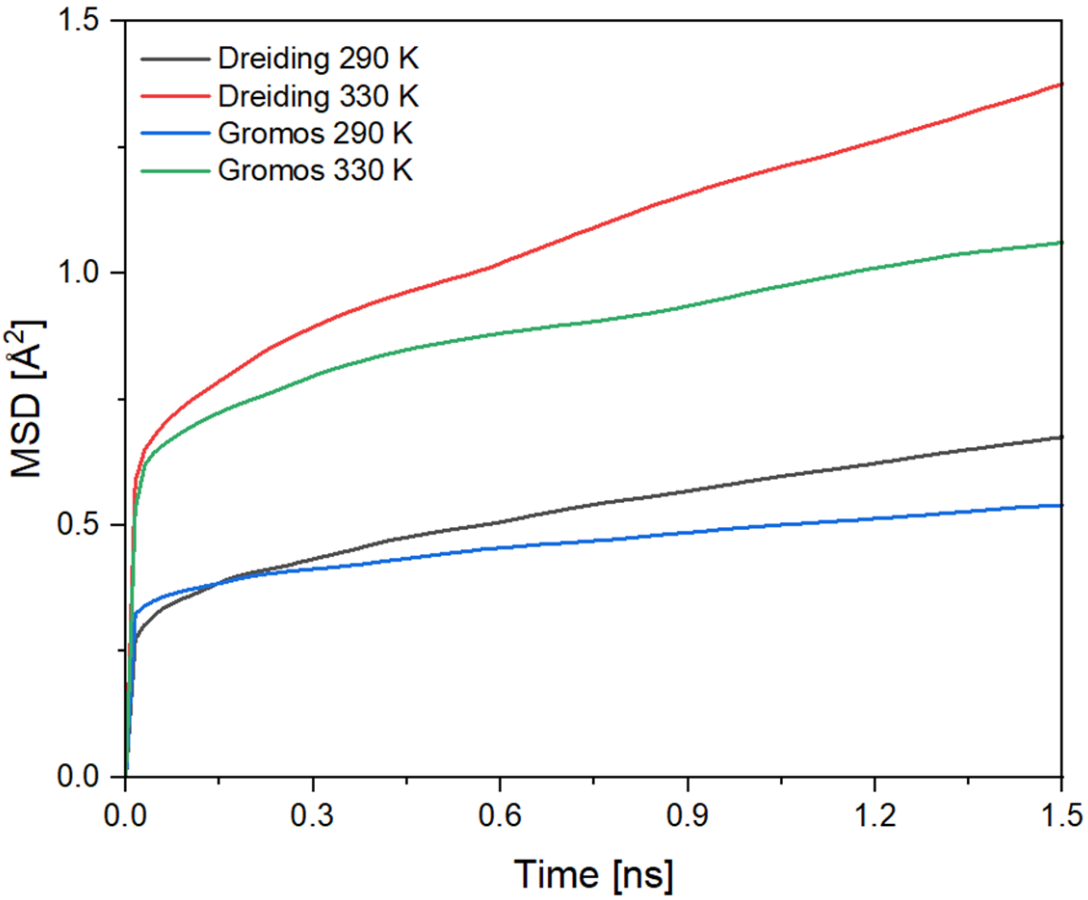


Figure 3.8. Comparison of Mean Square Displacement plots of the system at 290 K and 330 K for both the Dreiding and Gromos interaction potentials.

Table 3.2. Difference in interaction energy between the components at 290 K and 330 K

Interaction	Dreiding (kCal/mol)	Gromos (kCal/mol)
Hydrate – Polymer	-16300 ± 510	3700 ± 137
Polymer – Polymer	7000 ± 914	16000 ± 833
Hydrate - Hydrate	-7000 ± 582	1000 ± 828
Total Potential Energy	-7000 ± 442	20000 ± 809

From the PDFs above, we see that the there is substantial loss of crystallinity in the Gromos simulations with increasing temperature. Because melting is exothermic, the simulation with the more disordered hydrate at 330 K has a higher potential energy. We see this increase in all three non-bonded components (H-H, H-P, P-P) of the potential energy. In the simulations using the Dreiding potential, there is a net reduction in the total potential energy driven by a stabilization in the hydrate-polyelectrolyte interaction. As we observed in the PDFs and the density profile, in these more liquid-like simulations the water of hydration is able to aggregate around the sulfonic acid groups and form a stable local aqueous film at the interface.

3.4 Summary

In this work, it was discovered that the addition of polyelectrolyte dextran sulfate sodium to SSD keeps the water of hydration in close atomic proximity to the salt, preventing the longstanding issue of phase segregation in SSD. The water of hydration migrates to the interface between the hydrate and polyelectrolyte, aggregating around the sulfonic acid groups of the polyelectrolyte. The acid groups are spaced sufficiently close together, that a thin film of water forms. This interfacial film is sufficiently stable that the water is relatively immobile and does not penetrate further into the polyelectrolyte, at least on the time scale of these simulations. The thermodynamic driving force for this stabilization is found to be the interaction between the water of hydration and the polyelectrolyte.

Furthermore, this discovery was only possible through the combination of successful empirical investigation combined with the powerful atomic-scale techniques such as neutron scattering techniques and molecular dynamics simulation deployed in this thesis to provide an explanation for the empirically observed behavior. Total neutron scattering confirmed the presence of DSS did not alter the structural transformation. Molecular dynamics simulation provided a decomposition of the pair distribution function, density profiles, mean square displacements and potential energies. Simulations were performed with two interaction potentials, Dreiding and Gromos to better describe both phases of SSD. By revealing the atomic mechanism of the stabilization of SSD by DSS, this research can influence the selection and design of novel PCM composites with improved thermal characteristics for long-term use in buildings and other commercial heating and cooling applications.

CHAPTER 4

PERFORMANCE ENHANCEMENT METHODS FOR LOW-COST SALT HYDRATE PHASE CHANGE MATERIALS USING CELLULOSE AND CARBON MATERIALS

To enable the widespread adoption of low-cost PCMs such as $Na_2SO_4 \cdot 10H_2O$ and $CaCl_2 \cdot 6H_2O$, several issues related to them such as phase separation must be addressed. The preceding chapters have addressed phase separation problems in SSD. This section addresses the supercooling and thermal conductivity issues in low-cost salt hydrate PCMs using $CaCl_2 \cdot 6H_2O$ as the salt hydrate and strontium chloride hexahydrate as the nucleator to reduce supercooling, graphene nanoplatelet (GNP) as the thermal conductivity enhancer and cellulose nanofiber to disperse the GNP throughout the PCM composite. The development of stable low-cost PCM composites with enhanced thermal properties and performance will enable the widespread utilization of salt hydrate PCMs ion diverse applications and energy systems requiring the storage of thermal energy for later use. This Chapter is an article in preparation for submission to a journal.

Chapter Abstract

In recent years, thermal energy storage (TES) has gained attention for its role in promoting renewable energy solutions and sustainable energy consumption. The usage of strontium chloride hexahydrate (SCH), graphene nanoplatelet (GNP) and cellulose nanofibril (CNF) was investigated to enhance the TES performance of calcium chloride hexahydrate (CCH) by reducing supercooling, improving the thermal conductivity and energy storage capacity of CCH, respectively. Rheological characterizations demonstrated the addition of 1wt% of CNF into CCH produced optimum improvement in viscosity and boosted solid-like rheological behavior. Structural characterization reveals a physical mixing of the materials within the PCM composites. It also confirms the amphiphilicity of CNF which enables the surface attachment to GNP via hydrophobic interactions, for the effective dispersion of GNP throughout the PCM composite. The addition of nucleating agent, SCH decreased the degree of supercooling of CCH from ~20 °C to 3 °C. Thermal characterization showed the resulting PCM composite has high latent heat of melting of 186 J/g, phase change temperature of 32 °C, and stable thermal properties after being subjected to 70 melt-freeze cycles. Adding CNF and GNP to pure CCH increased its thermal conductivity by 114%. The high thermal performance of GNP and its effective dispersion by CNF are responsible for this enhancement. The study highlights the use of biodegradable nanocellulose for the preparation of PCM composites with improved performance. These composites have potential in the field of TES.

4.1 Introduction

In the bid to reduce the dependency on fossil fuels and their contribution to the greenhouse effect, numerous research efforts have been channeled towards the development and utilization of renewable and sustainable energy sources and energy storage systems [14]. However, this ecofriendly sources of energy suffer from intermittency, leading to unpredictability in energy generation. Hence, there is need for effective storage technologies to make energy available when needed. Utilizing latent heat thermal energy storage systems (LHTESS) is a suitable strategy for storing energy for use in later time, leading to increased energy efficiency and cost savings [117]. Phase change materials (PCMs), a notable class of LHTESS, have attracted the interest of several researchers due to their remarkable thermophysical properties [41]. These materials have a variety of uses, including buildings [118], cooling [119], desalination [120], and heat exchangers [121]. In building applications, phase change materials (PCMs) are utilized to minimize heat transfer between a building and its environment. PCMs store energy in both sensible and latent forms, allowing them to minimize heat transfer between a building and its environment [122]. Also, PCMs in built environment can reduce temperature fluctuations and shift peak loads, thereby leading to reduction in energy cost and increase in energy efficiency.

Inorganic PCMs based on salt hydrates for latent heat thermal energy storage are a prominent subset of PCMs that have attracted much study. This is due to their high volumetric energy storage capacity, availability across a broad range of acceptable melting temperatures, non-flammability, significant volumetric storage capacity, and cost-competitiveness relative to other PCM classes [123]. While pure salt hydrates like sodium sulfate decahydrate ($Na_2SO_4 \cdot 10H_2O$) and calcium chloride hexahydrate ($CaCl_2 \cdot 6H_2O$, CCH) are able to meet the temperature and energy storage capacity requirements for building applications, they also suffer from drawbacks like incongruent melting, phase separation, low thermal conductivity, and supercooling [124]. When phase separation occurs, there is high likelihood of precipitation of anhydrous salt or partial hydrates during melting of salt hydrates, attributed to the difference in solubility. The settling of the salt ultimately leads to drop in the energy storage capacity of the PCM after successive thermal cycles. Also, supercooling phenomenon results in the crystallizing at temperatures substantially below the freezing temperature due to the absence of adequate nucleation sites to trigger

crystallization. This impacts the release of heat by salt hydrates and causes a large temperature differential between melting and freezing. Therefore, to realize the promise of PCMs for widespread TES applications, these critical issues must be addressed.

To address the critical challenges in salt hydrate PCMs, several approaches are utilized including the use of additives such as thickeners, thermally conductive fillers, and nucleators to withstand numerous heat cycles, increase thermal conductivity and reduce supercooling effectively [119], [124]–[127]. For instance, Zhang et al. [128] fabricated composite PCM based on calcium chloride hexahydrate, diatomite, and paraffin. The enthalpies of fusion and freezing for the resultant composite are 108.2 and 98.5 J/g, respectively. The composite showed excellent stability up to 100 melt-freeze cycles. By combining urea, ammonium chloride, and SCH with sodium carboxymethyl cellulose as nucleators, Li et al [129] were able to adapt and optimize the characteristics of CCH. The final PCM composite has the following properties: 9.51 °C phase change temperature, 0.39 °C supercooling degree, 99.08 J/g melting enthalpy, and 0.330 W/m-K thermal conductivity. The PCM showed good thermal reliability and stability after 50 successive thermal cycles. In another work, Thakkar et al. [130] reported a CCH-based composite PCM with optimized thermal properties using 2 wt% of SCH to reduce supercooling from 12 °C to 0 °C. Furthermore, 5 wt% NaCl/KCl was utilized as stabilizer, preventing phase separation and incongruent melting. The prepared composite PCM had a melting enthalpy of 169 J/g after 25 melt-freeze cycles. The supercooling degree of CCH was found to be decreased from 22.06 °C to 3.89 °C when using 1 wt% boron nitride nanosheets, as reported by Zhang et al. [37]. The thermal conductivity also rose, from 0.3 to 3.918 W/m-K. During further investigation, it was found that after 20 cycles, the latent heat of melting was 144.19 J/g. In another study, Xu et al. [131] reported novel composite PCM using CCH with graphene oxide nano-sheets and SCH. The novel PCM significantly reduced supercooling degree in CCH by 99.2% and the reported melting enthalpy was 198.20 J/g after 250 cycles. While these aforementioned studies have shown enhancement in the properties of CCH salt hydrates using various additives, some additives require harsh conditions of increased temperature or acidic treatment during preparation and expensive materials cost, for example boron nitride nanosheets, and graphene oxide. Also, there is a sparse knowledge of the impact of the utilized thickeners and additives on the rheological properties of the salt hydrate. Thus, there is a need for the adoption of less harmful, environmentally friendly additives

to enhance the properties of salt hydrates. Further research on how these additives influence the rheological characteristics of salt hydrates is also necessary for efficient PCM design.

Nanocellulose based materials including cellulose nanofiber (CNF) are gaining research attention for the enhancement of salt hydrate PCMs in recent times. These materials are ubiquitous, inexpensive, biodegradable, and ecofriendly. Also, they have high moduli, and aspect ratio which enhances the formation of entangled networks with high gel strength, when dispersed in aqueous medium [132]. The gel strength is dependent on the concentration of CNF added to the mixture, as reflected by the storage and loss moduli values. When the critical concentration of CNF is reached, a three-dimensional gel-like structure emerges. These gel-like structures based on the entanglement of the nanofibrils and the hydrogen bonds among the adjacent nanofibrils can bind the salt hydrate together [80]. Also, there is increase in viscosity by physical thickening which limits the diffusion length of water and helps prevent phase separation or incongruent melting in salt hydrates. To enhance the thermal conductivity performance of salt hydrate, carbon-based materials including graphene, expanded graphite (EG), carbon nanotube (CNT), graphene oxide (GO), and graphene nanoplatelet (GNP) have been used extensively [133]–[136] . This is due to their high thermal conductivity values and heat transfer performance. These thermal conductivity enhancers are prone to aggregation due to the influence of van der waal interaction among the particles [80]. In composite systems, CNF has been demonstrated to effectively disperse these carbon-based components without affecting their characteristics [137]–[139]. Therefore, CNF can serve as an excellent dispersant in composite PCMs for the property enhancement of PCM materials.

In this work, biodegradable CNF, and CNF-based PCM composites were developed to enhance the thermal energy storage performance of CCH. Rheological experiments were used to examine the thickening impact and the optimum concentration of CNF that provides the best stability effect in CCH. Furthermore, the optimum concentration of the nucleating agent was analyzed to give the lowest degree of supercooling in CCH. To improve the thermal conductivity of CCH, GNP was used as an additive. The produced PCM composites were thoroughly analyzed to determine their structure, morphology, thermal properties, and thermal cycling stability. Also, the mechanism of enhancement of the PCM was explained. The amphiphilicity of CNF is a key factor in the dispersion of GNP in the PCM composite, leading to the formation of a compact and

stable PCM composites with enhanced thermal properties. The prepared PCM composites show promise for use in creating a robust and effective TES system, especially in residential building applications.

4.2 Materials and Methods

4.2.1 Materials

Calcium chloride hexahydrate ($CaCl_2 \cdot 6H_2O$, CCH), and strontium chloride hexahydrate ($SrCl_2 \cdot 6H_2O$, SCH) were obtained from Sigma-Aldrich, cellulose nanofibril (CNF) was from University of Maine Process Development center while XG Sciences Inc. supplied graphene nanoplatelets (GNP, Grade M) with a mean particle size of 5 nm. Materials were used as-is, without any further treatment.

4.2.2 Methods

4.2.2.1 Sample preparation

Using $CaCl_2 \cdot 6H_2O$ as the main component, the composite PCMs were prepared by the physical mixing of $CaCl_2 \cdot 6H_2O$ with various concentrations of SCH, CNF, and GNP. The PCM mixture is typically kept under magnetic stirring for 1hour in a 50 °C water bath to enable homogenous mixing and dispersion. Afterwards, the composite PCM is synthesized. The sample matrix of the various formulations of the CPCM is reported in Table 4.1.

4.2.2.2 Sample Characterization

The structure of the PCM samples was studied using X-ray diffraction (XRD). The XRD patterns of the PCM mixes were analyzed using a PANalytical Empyrean diffractometer to ascertain the crystal structure of the materials. The tube current was 40 mA, and the X-ray voltage was 45kV; the Cu anode had a Kα of 1.54Å. At a scan rate of 1°/min, XRD data were recorded across a 2θ range of 5° to 90°.

Attenuated total reflectance infrared spectroscopy (ATR-IR) spectra were obtained using a PerkinElmer Frontier FTIR/NIR spectrometer fitted with a diamond ATR attachment and a spectral resolution of 2 cm^{-1} in the 4000–600 cm^{-1} range to examine the chemical structure of the salt hydrate samples.

Table 4.1. The compositions of composite PCMs containing CCH, SCH, CNF, and GNP

Sample ID	wt% of SCH, CNF, and GNP added to 100wt% of $CaCl_2 \cdot 6H_2O$		
	SCH (wt%)	CNF (wt%)	GNP (wt%)
CCH-S_1	1	0	0
CCH-S_3	3	0	0
CCH-S_5	5	0	0
CCH-S_7	7	0	0
CCH-$C_{0.5}$	0	0.5	0
CCH-$C_{1.0}$	0	1.0	0
CCH-$C_{1.5}$	0	1.5	0
CCH-$C_{2.0}$	0	2.0	0
CCH-$SC_{0.5}$	3	0.5	0
CCH-$SC_{1.0}$	3	1.0	0
CCH-$SC_{1.5}$	3	1.5	0
CCH-$SC_{2.0}$	3	2.0	0
CCH-$SCG_{1.0}$	3	1.0	1.0
CCH-$SCG_{2.0}$	3	1.0	2.0

The thermophysical properties of the materials, such as phase change temperature and latent heat, were investigated utilizing differential scanning calorimeter (DSC 2500, TA Instruments) under a 50 mL/min nitrogen purge. Thermal cycling was performed on 10-20 mg of each sample at a ramp rate of 5 °C/min between -40 and 50 °C in an aluminum DSC pan that was hermetically sealed. Melting temperatures and phase transition enthalpies of PCM samples were determined using heating scans.

Due to the low sample utilization of DSC characterization, the thermal cycling stability of PCM samples across a broad range of temperatures was investigated using the Temperature-History (T-H) method. During the T-H test, 15-20 g of PCM samples were placed within a borosilicate glass tube (length ~190 mm, diameter ~10 mm). A 1/16-inch diameter hole for a T-type sheathed thermocouple insert was molded into the rubber plug that sealed the glass tube. A borosilicate glass tube was filled with water to serve as a reference medium. Glass tubes were subjected to thermal cycling at a ramp rate of 5 °C/min between 5 and 50 °C in an ambient temperature chamber (ESPEC SH-242). The chamber temperature was also measured using 1/16 "sheathed thermocouple of the T type. The temperature of the chamber, reference, and PCM samples were acquired using a National Instruments cDAQ 9214 data collecting system at a sampling rate of 1 second per sample. The temperature profile was used to examine the melting and freezing behavior of PCM samples. The phase change temperature, latent heat, and supercooling were analyzed in accordance with these earlier studies [140], [141].

Using field-emission scanning electron microscopy, the microstructure, and morphologies of the base materials and the composite PCMs were studied. Furthermore, optical microscopy was used to examine the structures of the CCH-based composites. The rheological characteristics of the PCM were examined using a rotating rheometer (ARES-G2; TA Instruments) with a 40 mm diameter parallel plate geometry. The PCM samples were sandwiched between the plates with a 1 mm separation. To prevent the evaporation of water from the samples, a solvent trap was used. At 40 °C, the viscosity was evaluated as a function of shear rates ranging from 0.1 to 100s^{-1}, and samples were tested in shear rate-controlled mode. The linear viscoelastic area was confirmed using an amplitude sweep test at a constant angular frequency (1 Hz) and a range of strain from 0.1% to 1000%. Oscillatory tests were performed on PCM samples by measuring the storage (G') and loss (G") moduli as a response to frequency (1-10 Hz) at a constant strain of 1%. To ensure

that the PCM stayed molten during the measurement, we kept the temperature at 50 °C. Also, nucleator, SCH was excluded from all the tested samples.

The Hot Disk technique [3][4] was used to determine the thermal conductivity of the PCM samples. This method gives the direct measurement of the samples thermal conductivity. A flexible sensor/heater with 2.0–7.5 mm radii and double-spiral nickel wire is inserted in the molten PCM bulk samples for about 5–20 s at 0.1–1.0 W power. Under constant power, the resistance of nickel heater is evaluated. Also, the temperature at the contact may be calculated using the known temperature coefficient of resistance of nickel. Through analysis of the recorded transient, the thermal conductivity of the material could be determined. This method is in accordance with ISO for measuring the thermal conductivity of materials [144].

4.3 Results and Discussion

4.3.1 Determination of the optimum amount of nucleating agent

A major challenge with the use of CCH in thermal energy storage applications is high degree of supercooling which causes unpredictable phase change and temperature swing in the material. As seen in the cooling curve of Figure 4.1 using the T-history method, CCH did not show freezing throughout the period under consideration, owing to high degree of supercooling (~20 °C) and the absence of adequate nucleation sites to enable crystallization or freezing. A recommended solution to this challenge is the use of nucleation agent with very similar crystal structure to CCH and are stable above the phase change temperature of CCH [145]. SCH, which is isostructural with CCH and a phase change temperature of 115 °C was selected and tested as the potential nucleation agent. The cooling curves of the CCH with different concentration of SCH (1 wt% ─ 7 wt%) are shown in Figure 4.1. The results showed that for 1 wt%, 3 wt%, 5 wt%, 7 wt% of SCH, the supercooling degree of the PCMs have drastically decreased to 2.76 °C, 2.34 °C, 2.63 °C, and 2.80 °C, respectively. This confirms the effectiveness of SCH in providing adequate nucleation sites and enabling the timely crystallization of CCH. This is explained by the similar crystal structure of SCH and CCH, which makes CCH to adhere to the surface of SCH for faster nucleation [131].

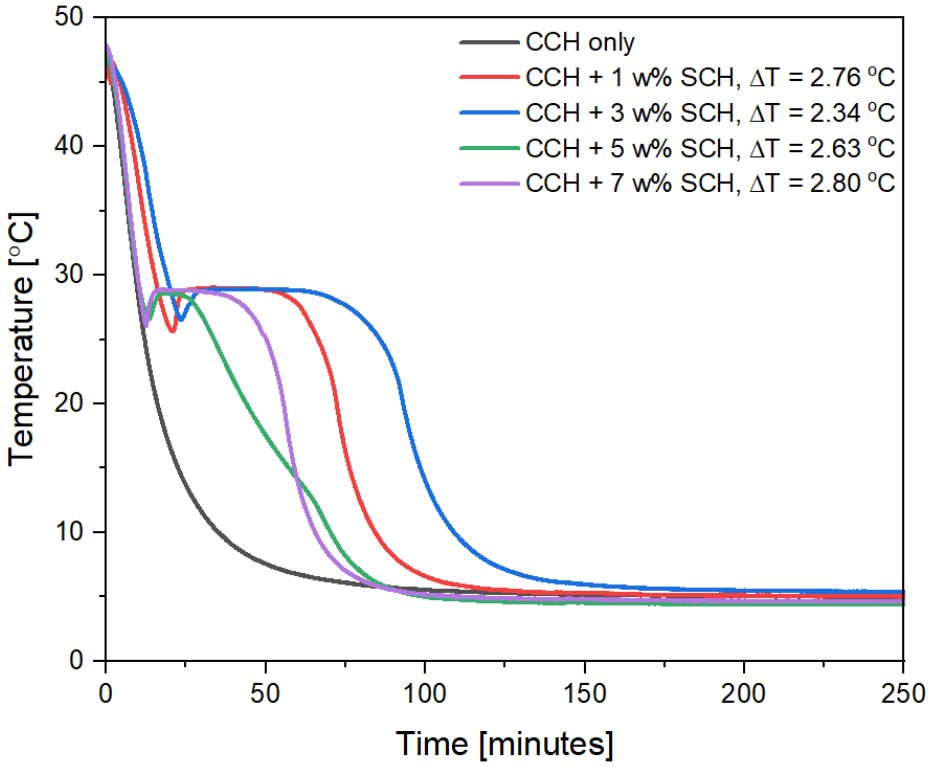


Figure 4.1. Cooling data showing the effect of the concentration of SCH on the supercooling of CCH

In determining optimum amount of SCH required for effective supercooling reduction, the test showed that as the concentration of SCH increased from 1wt% to 3wt%, there was a reduction in the supercooling degree. However, further increase in SCH led to an increase in the supercooling degree, which indicates the optimum concentration of SCH for effective supercooling reduction is around 3wt%. This agrees with the study by Li et al. in which 3wt% of SCH was reported as the ideal concentration for optimum reduction of supercooling [124]. Beyond this optimum concentration of SCH, there could be reduction in the calcium and chloride ion mobility, which ultimately leads to resistance in the nucleation process. Therefore, 3wt% dosage of nucleating agent, SCH was used for further testing throughout the study.

4.3.2 Utilization of CNF and GNP in the synthesis of PCM composites

A major limitation that has hindered the widespread of CCH in TES systems is low thermal conductivity. This impacts the charging and discharging rate of the salt hydrate thereby resulting in protracted thermal cycling duration, and ultimately lower thermal performance [37]. A major solution to this problem includes the use of low-cost, higher thermal conductivity materials as additives to enhance the property of CCH. Carbon-based materials find relevance in improving the heat-transfer properties and efficiency of PCMs due to their intriguing thermal characteristics [84]. Graphitic materials including graphene, compressed expanded natural graphite, and functionalized graphene oxides can be used to improve thermal conductivity. Although functionalized graphene oxides (GO) have shown to have superior self-dispersing capacity to graphite and graphene, the severe preparation conditions of these functionalized GO induce structural defects in these materials which significantly affects the superior thermal characteristics of GO [146].

Furthermore, the chemical modification and functionalization of graphene and graphite to enhance dispersion is also difficult, expensive, and detrimental to the environment [80]. By using an ecofriendly dispersion procedure with CNF, and GNP, we developed PCM composite with enhanced thermal properties based on CCH (salt hydrate), CNF (dispersant), GNP (thermal conductivity enhancer) and SCH (nucleator). It is proposed that the enhancement mechanism relies on CNF's entangled structure and amphiphilicity, which enable it to engage in a hydrophobic contact with GNP and bind to increase the dispersion of GNP in the composite system [147]. Also, CNF is able to induce hydrogen bonding in the system thereby controlling the release of water needed for crystallization and preventing incongruent melting of CCH (Figure 4.2). Shen et al.

[80] reported that GNP concentration above 2.5wt% did not show effective dispersion in PCM matrix, this is due to the aggregation of the nanomaterials in the PCM composite. Therefore, the concentration of GNP evaluated in this study is between 1wt% – 2wt% for optimum dispersion. To achieve maximum thermal performance of the PCM composite, it is also important to optimize the ratio of CNF added to the composite system. To this end, 3wt% of SCH nucleator, and several concentrations of CNF ranging from 0.5wt% to 2wt% were added to CCH and the energy storage capacity of the respective composites was tested after repeated thermal cycling.

As shown in Figure 4.3, sample with 0.5wt% CNF showed an energy storage capacity of 179 J/g after 10 cycles, while the sample with 1wt% CNF showed an increased energy storage capacity of 181 J/g. Further increase in the concentration of CNF above 1wt% led to a corresponding decrease in the latent heat energy of the composites. This indicate that the threshold concentration of CNF for optimum thermal performance is 1wt%. Also, the phase change temperatures of the composites are in the range of 32.66 °C – 32.93 °C (Figure 4.3b).

4.3.3 Microstructure Characterization of the PCM composites

Scanning electron microscopy (SEM) was used to examine at the microstructure and morphology of the base materials and PCM composites (Figure 4.4). First, Figure 4.4a illustrates the SEM micrograph of pure CCH with a coarse crystalline structure with the crystal size estimated to be within five microns. Furthermore, the micrograph of CNF is characterized with a high aspect ratio and entangled network structure as shown in Figure 4.4b. The SEM image of GNP showed a sheet-like structure with uneven multilayers and spaces between them in two dimensions. The introduction of SCH and CNF to CCH, the resulting composite showed a compact structure with smooth appearance throughout the cross section. This indicates the compatibility of the base materials forming a homogenous phase. The compact structure of the composite is related to the inducement of charge screening effect by the ions of the salt hydrate particles making the cellulose fibrils repel each other less strongly. The change in the colloidal contact coupled with the enhanced hydrogen bonding between the fibrils reinforce the fiber networks and cause the nanocellulose to be denser [147][63].

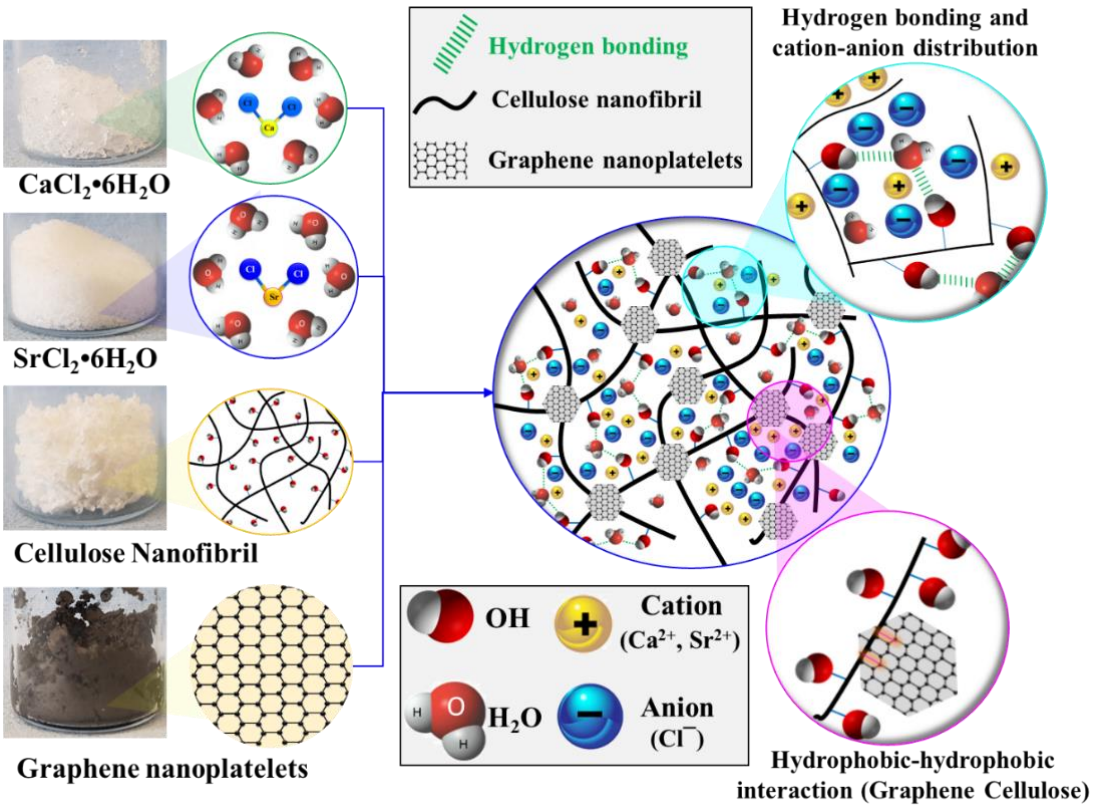


Figure 4.2. Schematic of the property enhancement mechanism of CNF and GNP on CCH phase change material

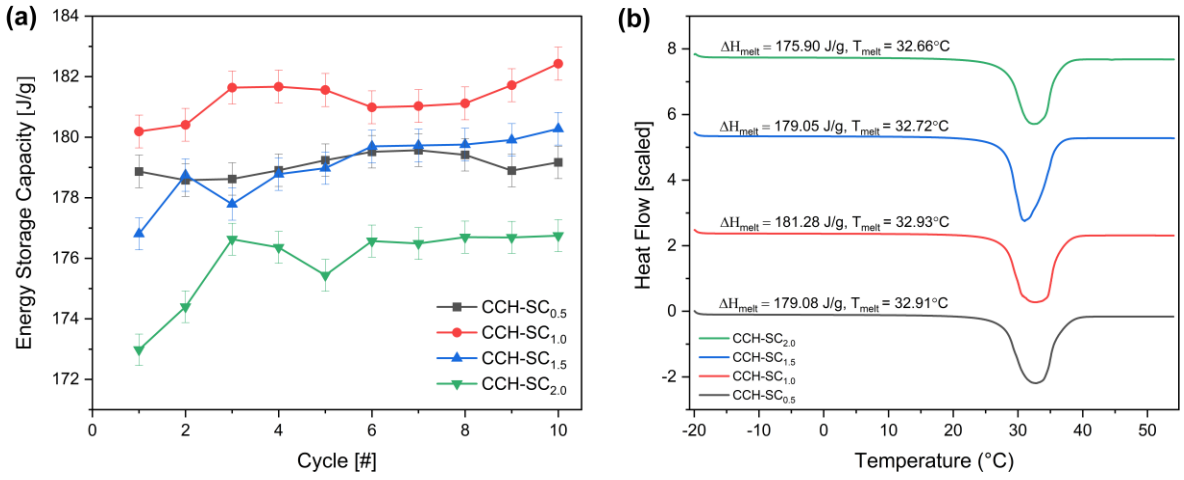


Figure 4.3. Thermal properties of CCH-based composite (a) Change in energy storage capacity of CCH-SC composites in 10 cycles (b) DSC curves of CCH-SC composites.

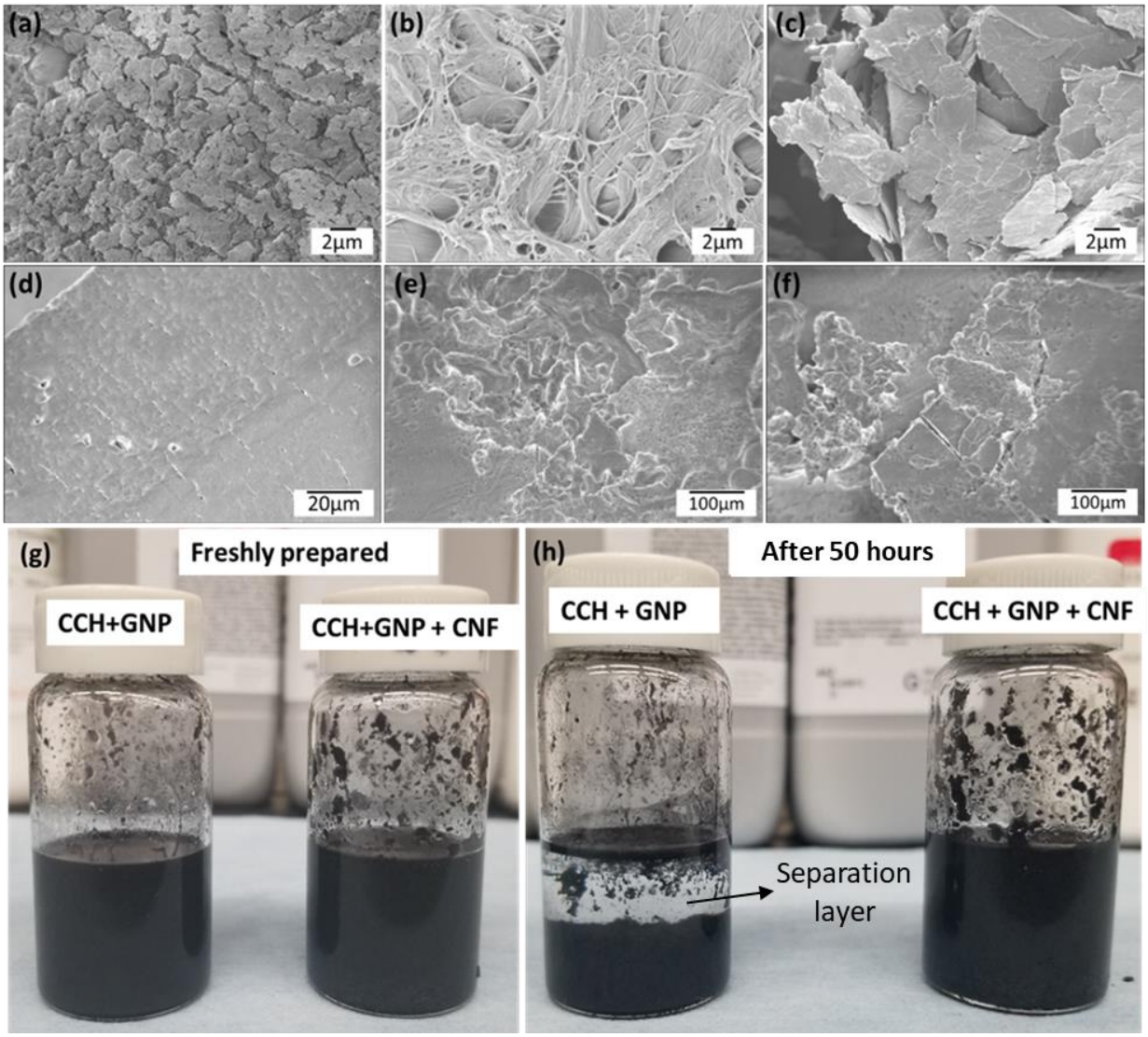


Figure 4.4. Microstructure characterization of additives and PCM composites (a) Pure CCH (b) CNF (c) GNP (d) CCH-$SC_{1.0}$ (e) CCH-$SCG_{1.0}$ (f) CCH-$SCG_{2.0.}$ Visual observation of PCM composites (g) freshly prepared sample (h) sample after 50 hours

As a consequence, the PCM composite becomes more viscous and uniform. Also, the micrograph of PCM composites containing 1wt% GNP and 2wt% GNP are displayed in Figure 4.4e and Figure 4.4f respectively. The composite showed a homogenous structure with the fibrillated network of CNF spreading uniformly to enhance the dispersion of GNP throughout the composite matrix. The effective dispersion of GNP is ascribed to the hydrophobic interactions between GNP and CNF in which the CNF is linked to the GNP sheets. The CNF stabilizes the dispersed GNP by sterically impeding its reaggregation [148]. Hence, the dispersive properties of CNF enabled the formation of PCM composites with homogenous structure. To confirm the dispersive abilities of CNF visually, two CCH and GNP based samples, with and without CNF were prepared as shown in Figure 4.4g. After 50 hours, changes in the samples were observed (Figure 4.4h). In the sample without CNF as the dispersant, GNP particles settled down and agglomerated showing a separation layer. However, the sample with CNF (1wt% CNF) maintained its homogeneity. This further confirms the efficacy of CNF as a promising dispersant aiding the uniform distribution of thermal conductivity additives in PCMs systems.

4.3.4 Rheology of the PCM composites

Rheological tests were conducted on CCH with varying concentrations of CNF (0.5wt%, 1wt%, 1.5wt%, and 2wt%) to evaluate the impact of the thickener on the rheological properties of CCH and to determine the critical concentration of the thickener for optimum PCM properties; the results of these tests are presented in Figure 4.5. First, the flow property of the PCMs, which is sensitive to the rate of change in viscosity with strain was evaluated using a flow sweep test as illustrated in Figure 4.5a. The pure CCH sample shows a relatively constant viscosity of 0.02 Pa s, as the strain rate increases, which is typically a Newtonian behavior. This behavior is expected since CCH contain a major quantity of water of crystallization and water also behaves as a Newtonian fluid, with constant viscosity irrespective of the applied strain rate. However, the introduction of CNF changes the flow properties of the PCM from Newtonian behavior to non-Newtonian behavior. In essence, the PCM composites containing CNF showed a shear thinning behavior in which the viscosity of the mixtures reduces as the applied shear rate increases. These viscosity values follow the well-established power law as shown below [76]:

$$\eta = K\gamma^{n-1} \quad (4.1)$$

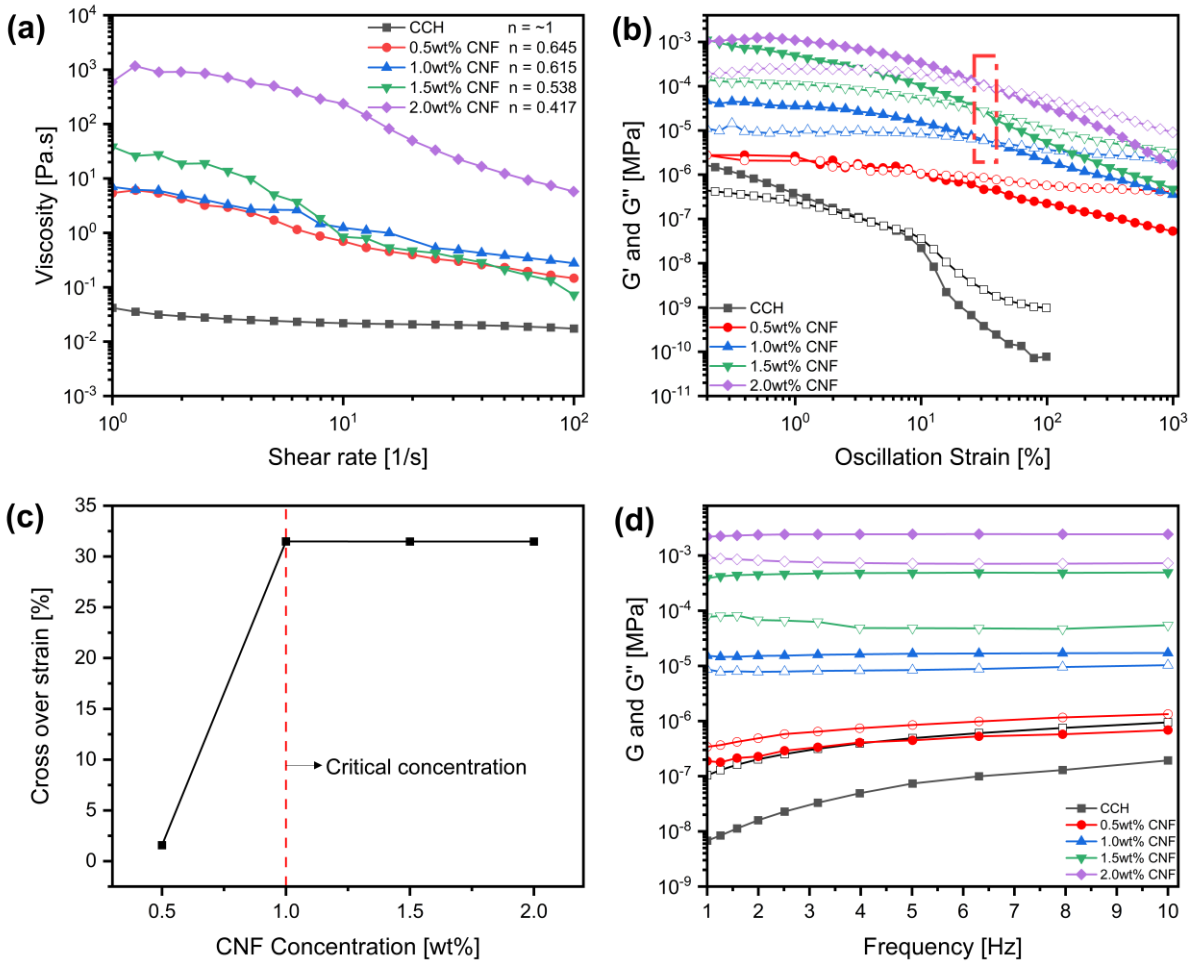


Figure 4.5. Rheology Characterization of CCH-based PCM mixtures (a) Flow test (b) Amplitude sweep test (c) Crossover strain as a function of CNF concentration (d) Frequency sweep test. Closed symbols in (b) and (d) represent storage modulus, G' while open symbols represent loss modulus, G".

The higher viscosity values of the PCM composites at low strain rate is attributed to the increase in the nanofibrils entanglement which forms a network structure resisting the shearing of the materials. These tangled networks, however, collapsed under a higher shear force when the shear rate was continuously increased, resulting in a greater drop in viscosity. The shear thinning effect is further associated with the thixotropic and pseudoplastic properties of CNF [132], which becomes more pronounced with the increase in the concentration of CNF in the suspensions. The power law index, $n < 1$ further confirms the shear thinning behavior of the CNF-based composites, and the reduction in the power law index with increased concentration of CNF signifies more deviation from the Newtonian behavior (n=1).

Storage (G') and loss modulus (G") measurements might provide light on the form stability of the PCM composites [79], which is essential since material stability of PCMs is a key design feature for certain thermal energy storage systems. In the amplitude sweep test shown in Figure 4.5b, G' and G" reflect the solid- and liquid-like behaviors, respectively. The cross-over strain is defined as the strain at which the material exhibits properties more typical of a liquid than a solid (G" > G'). As seen in the amplitude sweep test in Figure 4.5b. The entangled network of CNF causes the CCH/CNF composites to behave like solids, as shown by the G′ values being greater than the G" values for all CNF-containing samples. Due to an increase in CNF interactions, the G′ of CCH/CNF composites increased as the CNF concentration increased. The strength of the CNF network may be measured by the cross over strain, which is the transition point beyond which the G" > G' values (liquid-like behavior). The findings show that when the CNF concentration grew from 0 wt% to 1 wt%, the cross over strain increased constantly. Beyond this point, the cross over strain for CNF concentration of 1.5 wt% and 2 wt% did not increase beyond 31.5%, as seen in the marked area of Figure 4.5b and the plot in Figure 4.5c. This further shows that 1wt% CNF is a critical concentration which is enough to build robust entangled networks for the optimum performance of the PCM composite.

Figure 4.5d demonstrates that in the frequency sweep of pure CCH and sample with 0.5 wt% CNF, the loss modulus displays greater values than the storage modulus. This exemplifies a typical characteristic of liquids. Also, the frequency-dependent rise in the G' and G" values of pure CCH and sample with 0.5 wt% CNF is consistent with liquid-like relaxation characteristics in materials [79]. In contrast, the G' and G" values of samples with 1 wt%, 1.5 wt%, and 2 wt% CNF

concentration did not show significant variation with frequency, indicating linear viscoelasticity in the samples. Moreover, the G' values are larger than the corresponding G" values for these mixes within the test frequency range, indicating solid-like characteristics. This further confirms the formation of adequate entangled network by CNF in the PCM matrix leads to a frequency independent response.

4.3.5 Crystal Structure and chemical Structure characterization

The XRD diffractograms of CCH, SCH, GNP, and other PCM composites were analyzed to generate insight on the crystalline structure stability and the interactions of hydrated salts in composite as shown in Figure 4.6a. Standard X-ray diffraction powder patterns from the National Bureau of Standards' Institute of Material Research were used to compare the diffraction patterns CCCH with the reference data [149]. The XRD patterns strongly agrees with the reference data with obvious peaks at 13°, 22.7°, 26.1°, 32.1°, 34.8°, 39.8°, 41.8°, 45.8° which corresponds to (110), (210), (111), (211), (221), (330), (321) and (002) crystal plane respectively. Also, the diffractogram of SCH showed peak positions similar to CCH (but with lower intensity) at 13°, 22.7°, 26.1°, 34.8°, and 39.8°. This indicates that SCH and CCH have similar crystal structure, which is a major phenomenon used to trigger nucleation in CCH. Furthermore, the XRD diffractogram of CNF showed signature peak at 16.2° and 22.6°. These visible peaks are correlated to a cellulose type I structure, and they are located on the (110), and (200) crystal planes [64]. The (110) and (200) crystal planes also indicate the existence of both hydrophilic and hydrophobic regions in CNF [63]. The (002) crystal plane in carbon is responsible for the signature peak at 26.4° in GNP's diffraction pattern [150]. The diffraction pattern of the composite has the distinctive peaks of the constituent components without the introduction of additional peaks; therefore, this is suggestive of a physical mixing of the components without the generation of new compounds.

To further characterize the chemical structures of the PCM mixtures, FTIR measurement of the samples was conducted as shown in Figure 4.6b. For CCH, the characteristics peak at 1628 cm^{-1} is attributed to the O-H stretching, and the broad peak at 3354 cm^{-1} is ascribed to the hydroxyl stretching vibrations of water [124]. SCH also show similar signature peaks to CCH, confirming the present of hydroxyl functional group.

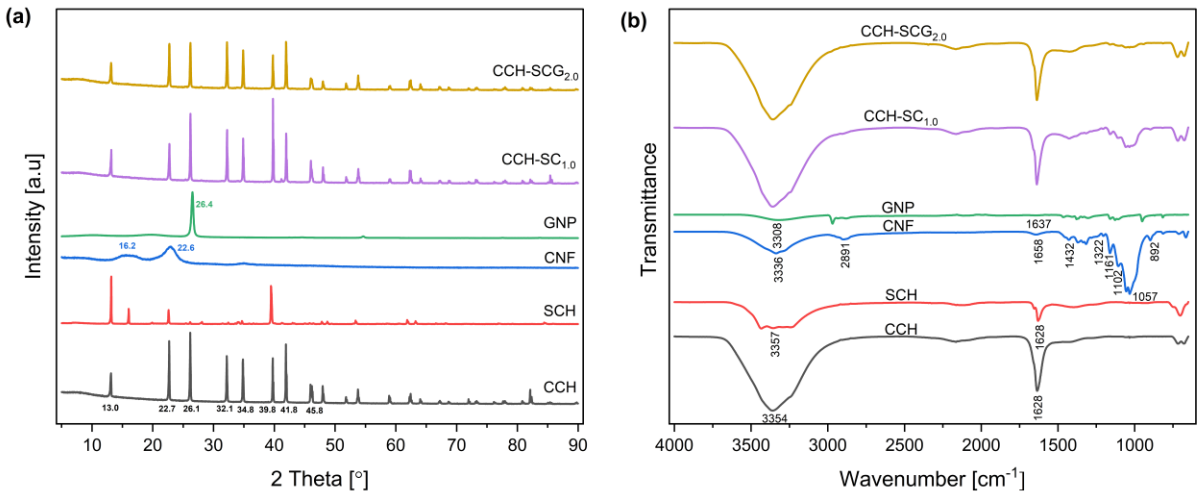


Figure 4.6. Crystal Structure and Chemical Structure characterization of PCM mixtures (a) XRD patterns of CCH-based PCM composites and their components (b) FTIR spectra of CCH-based PCM composites and their components

For CNF, the peak at 892 cm^{-1} indicates the glycosidic linkage in cellulose, while the signal at 1057 cm^{-1} is caused by the C─O─C pyranose ring skeleton [69]. The signal at 1102 cm^{-1} is due to the presence of glucose ring in cellulose, and the signal at 1161 cm^{-1} is due to asymmetric stretching in the C─O─C bond [70]. The maxima for CNF wagging symmetric bending and CH_2 asymmetric bending are 1432 cm^{-1} and 1322 cm^{-1}, respectively. The peak at 2891 cm^{-1} corresponds to the CH stretching vibration. The peaks at 1667 cm^{-1} and 3336 cm^{-1} also indicate the stretching of water [71]. The FTIR spectra of the PCM composites show characteristic peaks corresponding to each individual component, confirming the XRD results that the interaction between the components is not a chemical interaction since no new product is generated.

4.3.6 Thermal Cycling Stability Characterization of PCM composites

A major metric to consider in the adoption of PCMs for long-term energy storage application is the thermal reliability after repeated thermal cycles. Figure 4.7 shows the thermal cycling stability of both pure CCH and the synthesized composites. Firstly, as can be shown in Figure 4.7a, the average ESC of pure CCH is calculated to be 177 J/g based on a preliminary thermal cycling test up to 10 cycles in DSC. This agrees with the values reported by Zhang et al.[37]. With the introduction of CNF and SCH, the ESC of the resulting composite, CCH-$SC_{1.0}$ is evaluated as 181 J/g, which is a major enhancement compared to the ESC for pure CCH. The addition of GNP further increased the ESC of the composites. For instance, CCH-$SCG_{1.0}$ showed ESC of 185 J/g and the ESC of CCH-$SCG_{2.0}$ is estimated to be 182 J/g.

To evaluate the suitability of PCMs for industry-level application, larger quantities of the test samples are required for testing in the laboratory environment. DSC test uses smaller quantity of samples (10-15 mg), but this does not evaluate the supercooling degree effectively [21]. Hence, T-history measurements using few grams of samples (15-20g) was employed in the large-scale evaluation of the thermal cycling stability as shown in Figure 4.7b. After being subjected to 40 cycles, the ESC of pure CCH dropped from 176 J/g to 172 J/g. Also, there was a decline in the ESC of the composite samples during the first 10 cycles; this was ascribed to the initial interaction of the base materials, which led to effective dispersion and stability in the thermal cycling performance [113]. CCH-$SC_{1.0}$ showed a stable ESC of 178 J/g within 70 melt -freeze cycles.

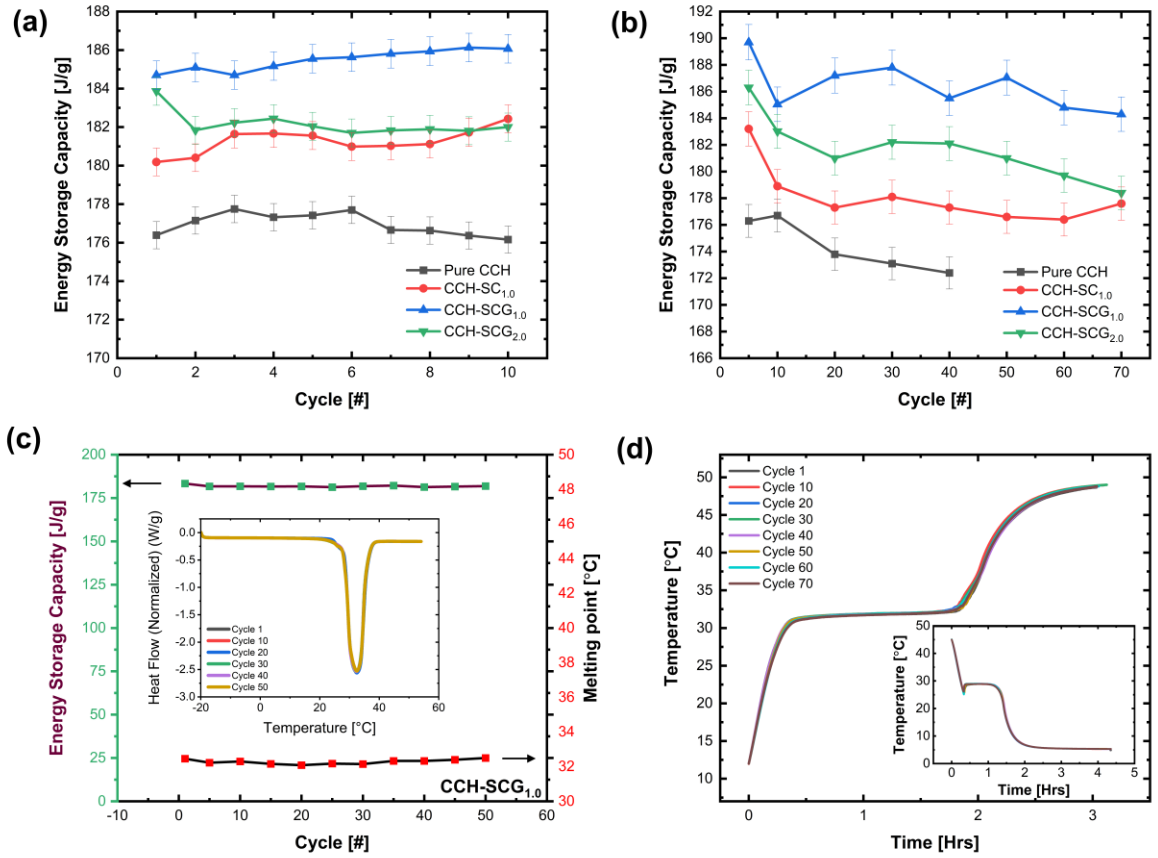


Figure 4.7. Thermal cycling measurement of PCM mixtures (a)Energy storage capacity of PCM in 10 cycles using DSC (b) Energy storage capacity of PCM in 70 cycles using T-History method (c)Line plot of energy storage capacity of CCH-SCG$_{1.0}$ in 50 cycles using DSC, inset shows the overlay of the DSC thermograms over 50cycles to show stability (d)Heating and cooling (inset) curve of CCH-SCG$_{1.0}$ in 70 cycles using T-History method.

Table 4.2. Thermal properties of pure Calcium Chloride Hexahydrate and its composite PCMs

Samples	Melting Enthalpy (DSC, J/g)	Melting temperature (DSC, °C)	Melting Enthalpy (T-history, J/g)	Melting temperature (T-history, °C)	Freezing temperature (T-history, °C)	Supercooling temperature (°C)
CCH	176.96	29.83	173.50	29.60	9.71	19.89
CCH-$SC_{1.0}$	181.28	32.93	178.18	32.03	28.86	3.17
CCH-$SCG_{1.0}$	185.35	32.63	186.42	32.12	28.88	3.24
CCH-$SCG_{2.0}$	182.15	32.63	181.71	32.14	28.71	3.43

Furthermore, CCH-$SCG_{1.0}$ showed enhanced thermal performance with stable ESC of 184.3 J/g after 70 thermal cycles, which is 97% stability when compared to the fifth cycle. The entangled network of CNF reduced incongruent melting in CCH and increased GNP dispersion inside the PCM matrix based on hydrophobic-hydrophobic interaction, improving thermal cycle stability. However, CCH-$SCG_{2.0}$ sample showed lower ESC value of 178.4 J/g and 96% stability in ESC after 70 melt-freeze cycles. This shows that increasing the dosage of GNP beyond certain concentration limit can lead to increase in aggregation of the GNP in the PCM matrix which could limit the heat transfer performance of the PCM composites.

The thermal properties of the most stable composite, CCH-$SCG_{1.0}$ was further confirmed with the DSC characterization over 50 cycles as reported in Figure 4.7c. The constant ESC value (181 J/g) and overlapping of the DSC melting plots over 50 cycles (inset plot) proves the excellent thermal stability of the material. Also, the T-history characterization results (Figure 4.7d) showed that the melting and cooling curves of successive thermal cycles overlap well, confirming the thermal stability of the materials. Also, the composite showed consistent supercooling degree, suggesting the distribution of GNP was even and did not interfere with the crystallization of CCH. As reported in Table 4.2, the additives further increased the melting point of pure CCH from 29.6 °C to 32 °C. Also, the freezing point of pure CCH is recorded as 9.71 °C, with high degree of supercooling at 19.89 °C. The degree of supercooling was lowered to 3 °C due to the presence of nucleator, SCH. SCH reduced the interfacial energy and enabled more nucleation sites in CCH, enhancing nucleation in the salt hydrate.

4.3.7 Thermal Conductivity Characterization of PCM composites

Figure 4.8 displays the thermal conductivity measurement of CCH and the respective composites at 32 °C. It was observed that pure CCH had a thermal conductivity of 0.502 W/m-K. This value is consistent with the report of Li et al. with thermal conductivity value 0.546 W/m-K.[129]. In addition, the thermal conductivity of pure CCH was found to be 0.529 W/m-K by Yuan et al.[151]. The thermal conductivity was slightly improved by adding 1 wt% CNF and 3 wt% SCH, increasing it to 0.575 W/m-K. Also, further increase in thermal conductivity to 0.811 W/m-K, was seen when 1wt% GNP was added to the corresponding composite. The thermal

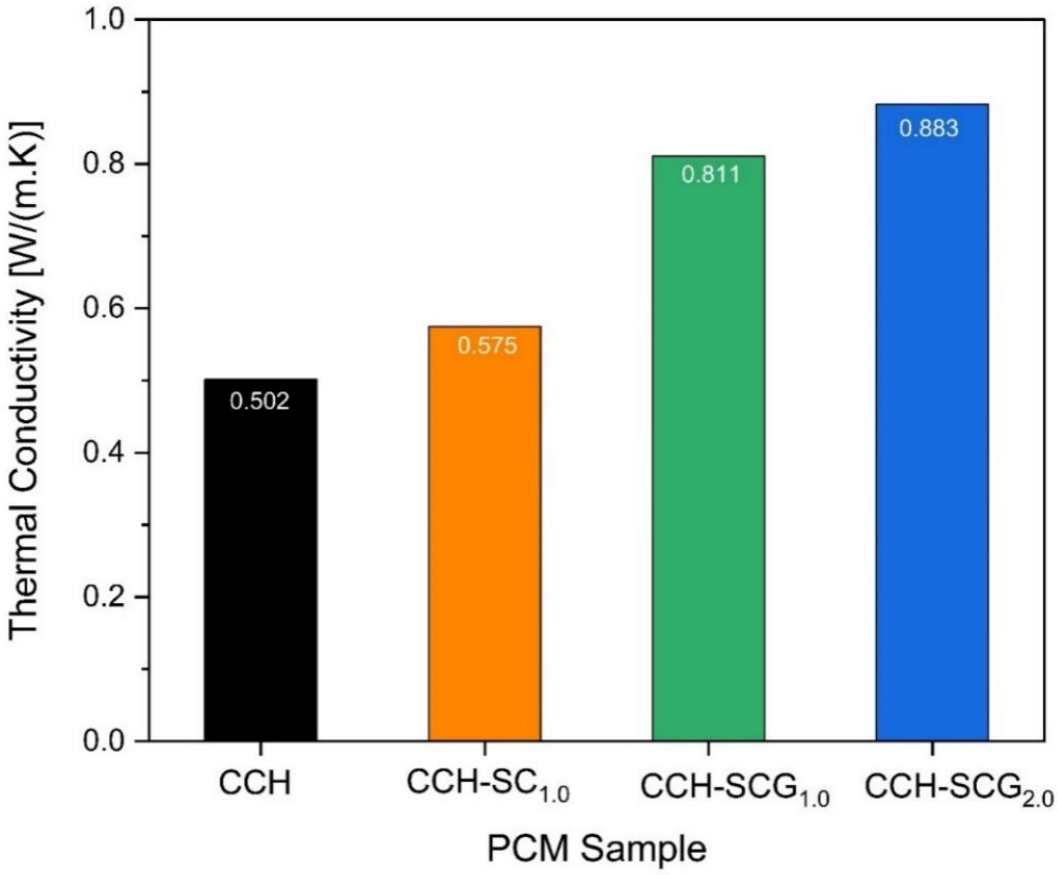


Figure 4.8. Thermal conductivity of CCH and CCH-based PCM composites: the influence of GNP concentrations

conductivity value of the composite was enhanced to 0.883 W/m-K upon increasing the dose of GNP to 2wt%, which is an increase of 114% when compared to the thermal conductivity of pure CCH. Study confirms that graphitic materials, such as GNP, may improve the thermal conductivity values of CCH leading to a corresponding improvement in charging and discharging rate of the PCMs in TES applications. GNP nanomaterial acts as the high thermal conductivity medium for the PCM composites, and its higher heat transfer ability is responsible for the increase in thermal conductivity values. Although, increased heat-transfer characteristics were observed in the produced PCM composite, the added 2wt% concentration of GNP may not be sufficient to deliver relatively high thermal conductivity. In the study by Yang et al. [152], thermal conductivity of the PCM after adding 5.3% GNP was reported to be 1.35 W/m-K. The major issues with the extra addition of GNP include increased materials cost and higher potential for GNP aggregation, affecting the optimum performance of the PCM composites. Therefore, the kind and concentration of carbon materials for thermal conductivity enhancement should be further considered in designing PCM composites with optimum thermal performance [80].

4.4 Summary

In this study, PCM composites with enhanced thermal characteristics for application in buildings system were successfully developed by combining $CaCl_2 \cdot 6H_2O$ with cellulose nanofibril, as thickening and dispersing agent, graphene nanoplatelet, as thermal conductivity enhancer, and $SrCl_2 \cdot 6H_2O$ as a nucleating agent. With the addition of 3wt% of $SrCl_2 \cdot 6H_2O$, degree of supercooling was significantly reduced to 3 °C. The utilization of 1wt% of CNF in the composite was environmentally friendly and effective in dispersing GNP throughout the PCM composites, thereby forming a compact structure. Structural characterization results confirm the physical mixing of the constituent materials in the PCM composites. Using T-history measurement, the resulting PCM composites including GNP dispersed with CNF demonstrated a high latent heat energy of 186 J/g, melting temperature of 32 °C, supercooling of 3 °C and an excellent thermal stability after 70 successive melt-freeze cycles. The produced PCM composites exhibited a maximum thermal conductivity of 0.883 W/m-K, 114% higher than that of pure CCH, as determined by thermal conductivity testing. The enhancement mechanism in these PCM composites is based on the entangled structure and amphiphilicity of CNF which allow it to make

hydrophobic contact with GNP, resulting in a greater dispersion of GNP throughout the composite system. Moreover, CNF is able to inhibit incongruent melting of CCH by inducing hydrogen bonding in the system, which regulates the release of water required for crystallization. This produces a salt hydrate PCM composite with enhanced thermal energy storage characteristics. This study sheds light on the potential use of environmentally friendly natural polymers like CNF in the rapidly developing area of thermal energy storage, especially in the building systems.

CHAPTER 5

TAILORING OF THERMAL PROPERTIES OF LOW-COST SALT HYDRATE PHASE CHANGE MATERIALS USING EUTECTIC MIXTURES

This section addresses the limited option of salt hydrate PCMs for near-ambient thermal energy storage applications. It discusses the development of new eutectic mixtures with lower phase change temperature in the near-ambient temperature regime with melting temperature ~25 °C with potential applications for human thermal comfort.

Chapter 5 includes a draft version of the published conference article presented at the 19th International Refrigeration and Air Conditioning Conference at Purdue, July 10 - 14, 2022 [153]. The latest version can be found in the Purdue e-Pubs Library (https://docs.lib.purdue.edu/iracc/2471) cited as:

Akamo, Damilola; Hirschey, Jason; Turnaoglu, Tugba; LaClair, Tim; Gluesenkamp, Kyle; Goswami, Monojoy; and Rios, Orlando, "Salt Hydrate Eutectic Mixtures for Near Ambient Thermal Energy Storage Applications" (2022). International Refrigeration and Air Conditioning Conference. Paper 2471.

Acknowledgement: This work was sponsored by the U. S. Department of Energy's Building Technologies Office under Contract No. DE-AC05-00OR22725 with UT-Battelle, LLC.

Chapter Abstract

This work reports the synthesis and characterization of $Na_2SO_4 \cdot 10H_2O$ – $Na_2CO_3 \cdot 10H_2O$ eutectic salt hydrate phase change material (PCM) using Differential Scanning Calorimetry (DSC), Attenuated total reflectance infrared spectroscopy (ATR-IR), and X-ray Diffraction (XRD) techniques. The eutectic point of the PCM mixture was predicted based on binary eutectic effect and ion exchange theory. The XRD and ATR-IR results indicate that the eutectic PCM mixture was formed based on only physical mixing without chemical interaction. Moreover, DSC results showed that the eutectic concentration is 50wt% $Na_2SO_4 \cdot 10H_2O$ – 50wt% $Na_2CO_3 \cdot 10H_2O$ with melting temperature of 25.18 °C and melting enthalpy of 187.46 J/g. Also, 78% of melting enthalpy was recoverable after 10 melt/freeze cycles. This shows that the eutectic mixture requires more enhancement approaches to stabilize and enhance its thermal properties for long-term thermal energy storage. Overall, this eutectic mixture has the potential to be used in building thermal comfort applications as a major heat storage and release medium due to its suitable phase change temperature and melting enthalpy.

5.1 Introduction

The growing popularity of renewable energy has boosted interested in energy storage systems. One of the prominent energy storage options is thermal energy storage (TES) in which systems store and release thermal energy for use in a wide range of applications [9]. TES systems prosper in applications involving temperatures close to the ambient temperature, such as building systems, refrigeration, space heating and cooling. Latent heat thermal energy storage (LHTES) is a highly effective technique for storing energy. LHTES involves the utilization of phase change materials (PCMs) in thermal systems and devices for energy storage and discharge [30]. PCMs have been demonstrated to have use in heat exchangers, and desalination in addition to energy storage. Where large temperature swings are unfavorable such as in thermally sensitive systems, they become useful. The implementation of LHTES enhances energy efficacy, flexibility, and load reduction [13].

Nevertheless, employing salt hydrate PCMs has substantial downsides, such as incongruent melting leading to phase separation, limited heat conductivity, corrosion, irregular supercooling, limited options for human thermal comfort. and high susceptibility to ambient condition [11][46]. The limitations of salt hydrate PCM have been investigated, and many approaches have been proposed to enhance its thermal performance. This includes thickeners [96], encapsulating materials [14] and nucleators [154]. Another effective approach for addressing the limited PCM options for building applications involves the concentration-dependent mixing of two or more salt hydrate PCMs to produce eutectic mixes with minimal supercooling, congruent melting, and tailorable phase change temperature for near-ambient applications.

The development and synthesis of eutectic salt hydrate combinations for usage between 25-30 °C has been the subject of a number of published works. Using 20 wt% $Na_2SO_4 \cdot 10H_2O$ and 80 wt% $Na_2HPO_4 \cdot 12H_2O$, Fang et al. [54] created a eutectic PCM composite. The nucleator, $Na_2SiO_3 \cdot 9H_2O$, and the shape stabilizer, SiO_2, were both added at concentrations of 2.5 wt% and 30 wt % respectively. The resultant PCM composite has a melting enthalpy of 142.9 J/g, a low phase transition temperature of 25.16 °C, and nearly no supercooling. Similarly, Xie et al. [155] characterized a PCM composite with a 60 wt% salt hydrate that was formed by filling expanded vermiculite with a 1:1 mass ratio of of $Na_2SO_4 \cdot 10H_2O$ and $Na_2CO_3 \cdot 10H_2O$. There was a latent heat of 110.3 J/g and a melting point of 23.98 °C in the PCM composite. Furthermore, eutectic

PCM combination created by Li et al. [57] consist of 75 wt% $CaCl_2 \cdot 6H_2O$ and 25 wt% $MgCl_2 \cdot 6H_2O$. Thickener was 0.5 wt% hydroxyethyl cellulose, and the nucleators were 3 wt% $SrCl_2$ and 1 wt% $SrCO_3$. The PCM mixture melts at 21.41 °C and a melting enthalpy of 102.3 J/g. The phase change temperature range for PCMs suggested by Li et al. [156] is 18-22 °C in the winter and 22-26 °C in the summer. The bulk of studies, however, discovered eutectic PCMs whose melting enthalpy or phase transition temperature fell below the range of acceptable interior temperatures for building. In addition, several sources report different eutectic concentrations for the identical PCM components. Therefore, authenticating the real eutectic concentration of PCM mixes is essential for improved materials design.

In this study, we used $Na_2SO_4 \cdot 10H_2O$ and $Na_2CO_3 \cdot 10H_2O$ to create a eutectic salt hydrate PCM combination. Through the use of differential scanning calorimetry (DSC), the thermal properties of PCM composites were analyzed. X-ray diffraction (XRD) and attenuated total reflectance infrared spectroscopy (ATR-IR) were used to investigate the crystal structure and chemical composition of the samples. This study is important because it creates a eutectic PCM mixture with ideal characteristics for uses like heat pump integration and human comfort cooling.

5.2 Materials and Methods

5.2.1 Materials synthesis

$Na_2SO_4 \cdot 10H_2O$ (SSD, purity>99 percent), and $Na_2CO_3 \cdot 10H_2O$ (SCD, purity>99 percent) were the inorganic salt hydrate PCMs used in this work. These reagents came directly from Sigma Aldrich and were utilized without any extra purification on the user's end. To prevent the loss of water from salt hydrates, the materials were handled exclusively in a humidity- and temperature-controlled glovebox. The Heat mixing method [157] was used to combine SSD and SCD to create the binary salt hydrates (BSH). First, SSD and SCD were each added to their own corresponding proportion in a borosilicate vial. As illustrated in Figure 5.1, it was then placed in a water bath heated to 60°C and agitated for an hour to guarantee full melting. The BSH mixtures were then obtained by leaving the PCM mixtures cool to room temperature naturally.

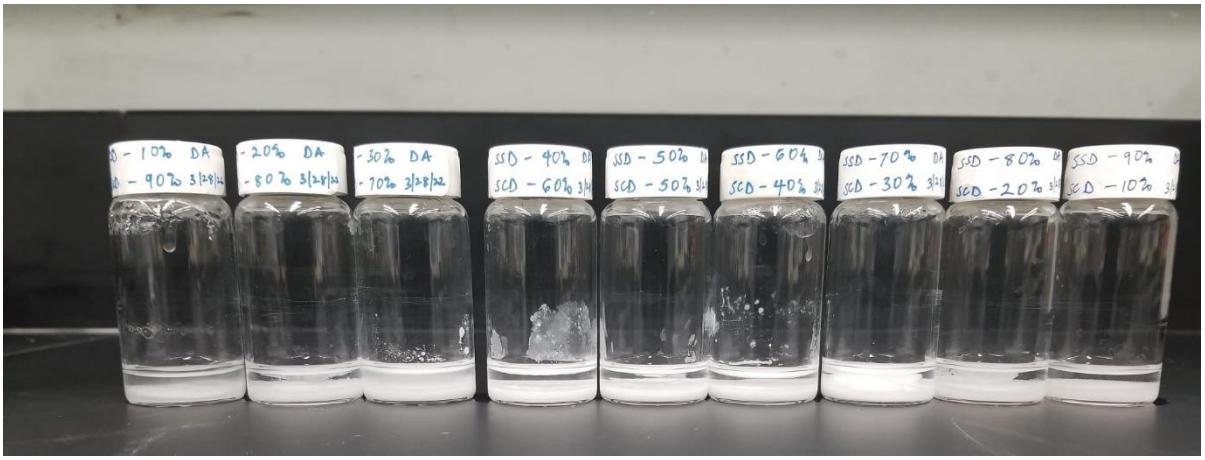


Figure 5.1. PCM composition of sodium sulfate decahydrate and sodium carbonate decahydrate in varying concentration in the melted state

5.2.2 Characterization

Phase transition temperature and melting enthalpy were measured by differential scanning calorimetry (TA Instruments, DSC 2500) between 5 and 45 °C with a scanning rate of 2 °C/min in nitrogen at a flow rate of 50 mL/min. In each study, we employed about 10–15 mg of the material. Hermetic DSC pan samples were weighed using an analytical balance (Mettler Toledo, Model) accurate to within 0.0001 mg for each experiment.

Salt hydrate samples were then put through a PANalytical Empyrean XRD diffractometer in order to determine their crystal structure by their X-ray diffraction patterns. For X-rays, a Cu anode with a K_α of 1.54 Å was used together with tube current and x-ray voltage of 40 mA and 45 kV, respectively. The scan was run at a rate of one per minute at a 2θ angle ranging from 5 to 90 degrees.

The attenuated total reflectance infrared (ATR-IR) spectra of the samples were obtained using a PerkinElmer Frontier spectrometer fitted with a diamond ATR connection with a spectral resolution of 2 cm^{-1} over the 4000-600 cm^{-1} range in order to characterize their chemical structure and surface chemistry.

5.3 Results and discussion

5.3.1 Determination of the eutectic point

DSC melting data of the formulations are displayed in Figure 5.2, which may be used to establish the appropriate concentration and thermal characteristics of the PCM blends. In most cases, two endothermic peaks may be seen in the graphs. This demonstrates the presence of distinct phases within the combinations. It's possible that melting of the mixtures is responsible for the peak at higher temperatures, while the second endothermic peak at lower temperatures is caused by the eutectic effect [158]. In these mixtures, a single peak appeared in the DSC melting curve only when 50% SCD (BSH5) was used as the mass proportion.

It is also worth noting that the DSC peaks at higher temperatures gradually migrate to lower temperatures as the mass fraction of SCD rises, resulting in a single peak at approximately melting temperature of 25.18 °C and a latent heat value of 187.46 J/g (Table 5.1). Because of its low melting point, the mixture is useful for heat-storage devices established close to ambient temperature [156].

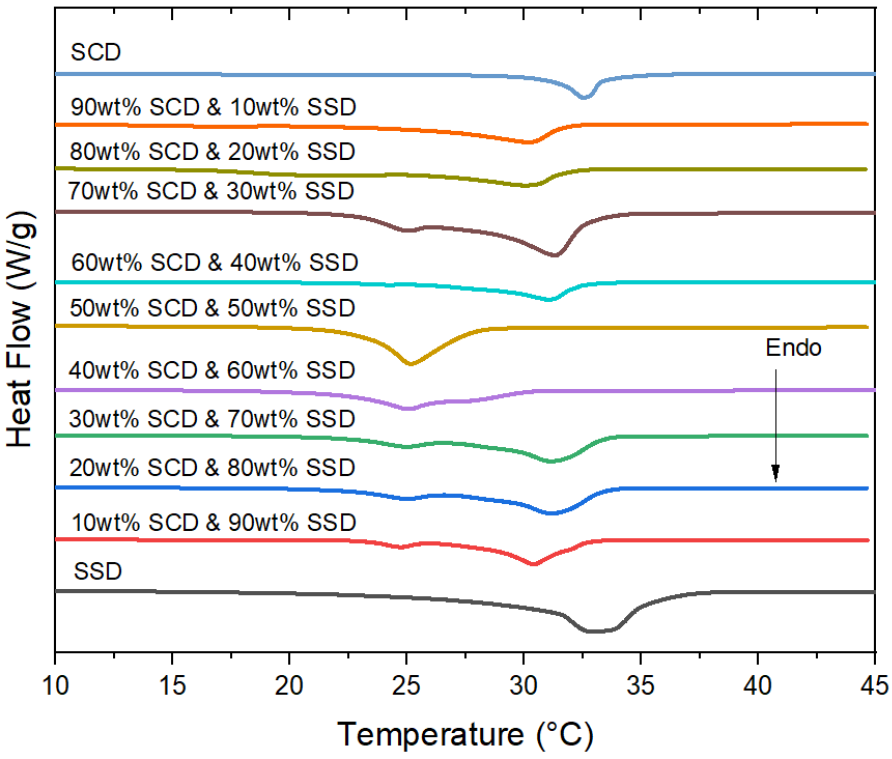


Figure 5.2. Diagrams of melting points determined by differential scanning calorimetry for $Na_2SO_4 \cdot 10H_2O$ (SSD), $Na_2CO_3 \cdot 10H_2O$ (SCD), and their combinations. A unique melting peak was seen for the 50wt% SCD (BSH5) sample, showing a distinct melting point.

Table 5.1. Table 1: Composition and thermal properties of the PCM mixtures

Sample	m_{SSD}: m_{SCD}	T_1 (°C)	T_2 (°C)	Melting Enthalpy (J/g)
SSD	100:0	-	32.94	145.87
BSH1	90:10	24.68	31.16	121.03
BSH2	80:20	24.87	30.41	181.88
BSH3	70:10	25.91	29.82	136.17
BSH4	60:10	25.20	27.82	126.23
BSH5	50:50	25.18	-	187.46
BSH6	40:60	25.12	27.17	142.36
BSH7	30:70	25.07	29.19	124.22
BSH8	20:80	24.29	30.47	170.71
BSH9	10:90	17.84	31.22	146.86
SCD	0:100	-	32.55	135.613

In addition, studies on the melting behavior of these PCM were conducted to better understand their thermal characteristics. Figure 5.3 shows the phase diagram of the PCM combination, which has the precise shape of a binary mixture with a eutectic point. It follows from the foregoing that when the amount of SCD in the combination becomes close to 50wt%, we get a eutectic. The eutectic output of the salt hydrate combination relies on an equal number of ionic exchanges between the various salts present in the solution [159]. As long as the participating ions keep their numerical connection constant, the salt hydrate will be stable at the eutectic concentration. Being a shared cation between the two salt hydrates, Na^+ is disregarded here. Therefore, the eutectic point can only be maintained if the anions, SO_4^{2-} and CO_3^{2-}, are in a 1:1 ratio. Extreme precipitation of the anhydrous salt ions from the mixture occurs outside of this ratio, resulting in a two- or three-phase mixture.

5.3.2 XRD Characterization

Figure 4 displays the XRD patterns of pure SSD and SCD, as well as the eutectic salt hydrate BSH5. At 2θ = 16.2°, 18.6°, 23.2°, 26.2°, 27.9°, 31.5°, 35.7°, and 43.1°, pure SSD displayed a series of strong peaks. There is agreement between these peak locations with the crystal structure that has been previously reported [61]. Also, the signature peak of SCD are at the positions with 2θ = 16.6°, 19.7°, 22.5°, 28.4°, 29.6°, 30.9°, 33°, 37.8°, and 41.1° [160]. In addition, the indexing revealed several overlapping peaks in the eutectic mixture BSH5, where the diffraction peaks of SSD and SCD were present. Since no new product was generated during the integration of SCD and SSD salt hydrates, this proves that the eutectic combination, BSH5, was formed by physical mixing or overlay.

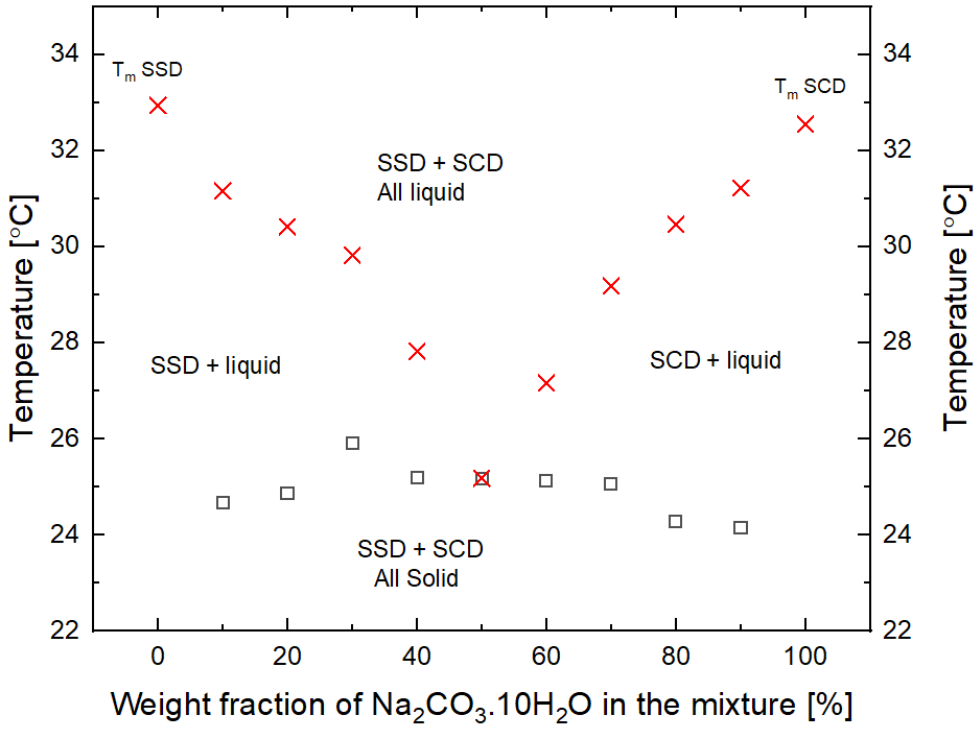


Figure 5.3. Phase Diagram of SCD+SSD, □ , eutectic temperature; x, melting temperature

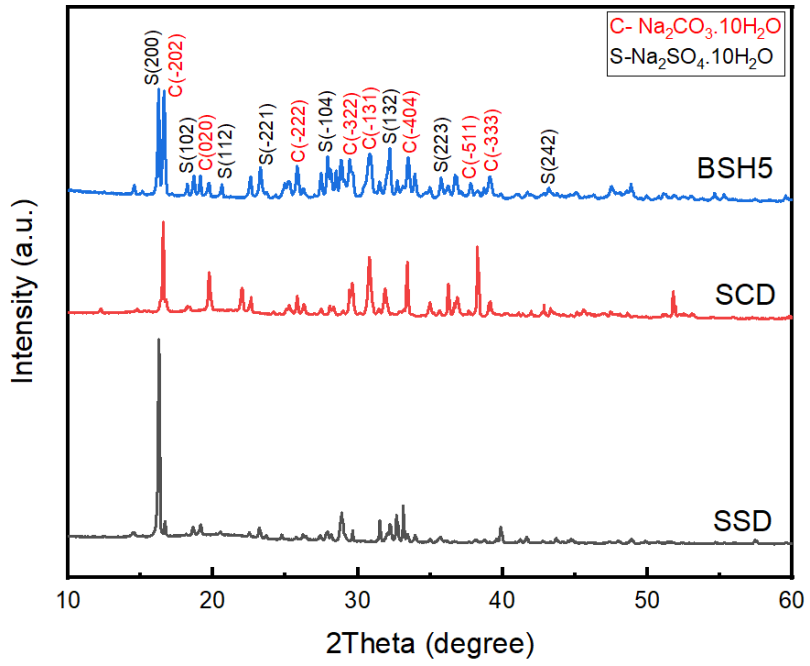


Figure 5.4. XRD patterns of pure SSD, SCD, and BSH5.

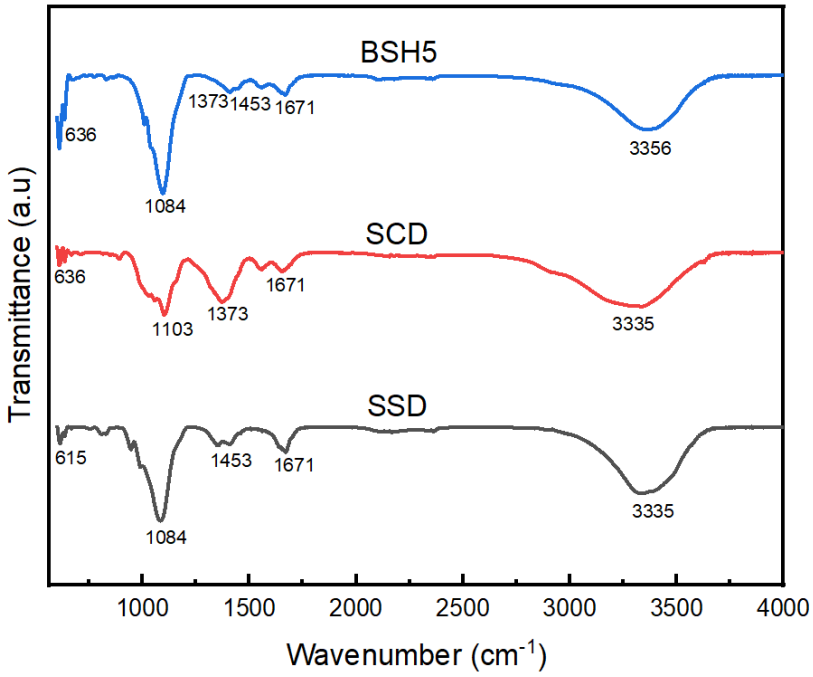


Figure 5.5. ATR-IR spectra of pure SSD, SCD, and BSH5.

5.3.3 Chemical Structure Characterization

Figure 5 shows the ATR-IR spectra of the samples. The spectra of pure SSD showed that the O-H stretching vibration was responsible for the peaks at 1671 cm^{-1} and 3335 cm^{-1}. The bending peak of S─O of SO_4^{2-} in SSD was assigned to the peak at 615 cm^{-1}, whereas the symmetric and asymmetric stretching vibrations of S=O in O─SO_2─O were at 1084 cm^{-1} and 1453 cm^{-1}, respectively. In SSD [66], this provides more evidence that SO_4^{2-} adopts a tetrahedral shape. The peaks at 636 and 1103 cm^{-1} in the spectrum of pure SCD represent the in-plane and out-of-plane bending vibrations of CO_3^{2-}. The CO_3^{2-} asymmetric vibration peak is located at 1373 cm^{-1} [157]. The distinctive 1671 cm^{-1} peak indicates a potentially unique vibration angle for O─H in H_2O. Additionally, the stretching vibration of O─H in H_2O is represented by the wide absorption peak at 3335 cm^{-1}. There may be a correlation between the hydrogen bonding in the crystallization water and the broadness of the peak between 3000 and 3600 cm^{-1}. Hydrogen bonding affects the infrared O─H spectra of materials by broadening the characteristic O─H stretching band at a lower frequency associated with the compound [161]. In addition, there was no new absorption peak in the BSH5 spectra, suggesting that the components of the eutectic mixes did not react chemically with one another. The aforementioned XRD findings were further supported by this.

5.3.4 Thermal Cyclic Stability of the Eutectic Mixture

For PCM mixes to be utilized for thermal energy storage, thermal stability is a crucial need. The PCM's thermophysical properties must hold up during repeated melting and freezing tests. In order to determine the melting enthalpy and phase change temperature of BSH5, a thermal cycling test was performed utilizing DSC analysis for 10 cycles. Figure 5.6 shows the BSH5 thermal cycling curves. As melting enthalpy was measured for BSH5, it was found to decrease with each cycle. Enthalpy loss percentage was determined to be 22% after 10 cycles, from an initial melting enthalpy of 189.42 J/g (Table 5.2), to a final melting enthalpy of 154.43 J/g. During the thermal cycling studies, a shift of 0.85 °C was also noted in the eutectic mixture's phase transition temperature. Due to its attractive melting point in the near-ambient temperature range after multiple temperature cycles, the eutectic combination BSH5 is well-suited for use in thermally sensitive systems and applications involving TES at near ambient temperature. Despite the suitability of the phase change temperature, the eutectic PCM is not thermally stable.

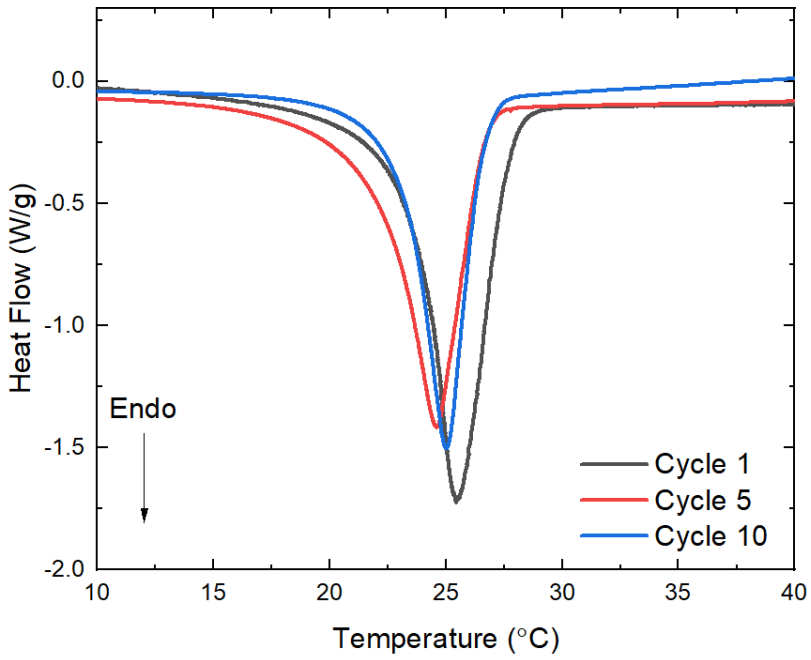


Figure 5.6. Melting enthalpy curves showing thermal cyclic stability test for BSH5

Table 5.2. Thermal cycling data for SSD-SCD Eutectic PCM mixture

Cycle	Onset of Melting (°C)	Melting Point (°C)	Melting Enthalpy (J/g)	Enthalpy loss percent (%)
1	23.38	25.45	189.42	-
5	21.93	24.59	162.52	14
10	22.92	25.02	154.43	22

Therefore, the thermal properties of the eutectic PCM mixes may be further enhanced by the application of a number of feasible solutions. The use of polymeric thickeners or polyelectrolyte stabilization [113] could assist stabilize PCM mixtures by providing electrostatic and stearic effects, and the use of polymeric or highly viscous components to construct a network structure or physically thicker mixture may help avoid phase separation [162].

5.4 Summary

In this research, we investigated the potential for adopting a new eutectic binary salt hydrate (BSH) PCM, a mixture of $Na_2CO_3 \cdot 10H_2O$ and $Na_2SO_4 \cdot 10H_2O$, to provide thermal comfort inside building systems. To make this combination, $Na_2CO_3 \cdot 10H_2O$ and $Na_2SO_4 \cdot 10H_2O$ are combined in ratio 1:1. The enthalpy of melting the resultant compound is 187.46 J/g, and its melting point is at 25.18 °C. In addition, after 10 cycles of melting and freezing, the eutectic mixture still had 78% of its latent heat recovered, suggesting that it needs effective additives to improve the stability of the melting enthalpy for repeated thermal cycles. The eutectic effect, characterized by a decreased melting point, is the consequence of a physical interaction between the salts $Na_2CO_3 \cdot 10H_2O$ and $Na_2SO_4 \cdot 10H_2O$ in the eutectic system, as demonstrated experimentally by ATR-IR and XRD. The eutectic PCM mixture has potential for use as energy storage material for temperature regulation systems and near-ambient TES systems.

CHAPTER 6
CONCLUSIONS AND RECOMMENDATIONS

6.1 Conclusions for each chapter

This section provides a detailed summary of the outcomes of the four research objectives pursued in this study towards the development of stable salt hydrate PCMs for thermal energy storage applications. The outcomes of each research objectives are highlighted below:

6.1.1 Empirical Approach to stabilize Low-Cost Salt Hydrate Phase Change Materials Using Polyelectrolyte Additives

Chapter 2 addresses the phase separation and stability problems in low-cost salt hydrate PCMs, especially SSD by investigating the effective stabilization mechanisms that could enable the adoption of low-cost phase change materials for thermal energy storage applications. In this work, eight different polymer additives were tested to address this concern. The eight additives are: sodium polyacrylate (SPA), potassium polyacrylate (PPA), carboxymethyl cellulose (CMC), hydroxyethyl cellulose (HEC), fumed silica, cellulose nanofiber (CNF), dextran sulfate sodium (DSS), and poly(sodium 4-styrenesulfonate) (PSS). The impact of these additives on phase stability, energy storage capacity, and rheology are extensively studied. Thermal cycling studies suggest mixtures containing SPA, PPA, and CNF degraded by at least 40% in energy storage capacity after 10 cycles, indicating that physical thickening alone is ineffective for improving SSD long-term performance. However, DSS-modified PCM mixtures demonstrated superior stability, even up to 150 melt/freeze cycles. The stabilization mechanism is tied to the electrostatic interaction between DSS polyelectrolyte and SSD which encapsulates salt particles and suspends them in a stable homogeneous solution, hindering phase separation. Therefore, DSS polyelectrolyte is the most effective additive for SSD, which highlights the significance of the electrostatic interaction compared to physical thickening alone. This study proposes an effective approach to improve the thermal stability of salt hydrate PCMs by utilizing polyelectrolyte-salt hydrate mixtures for energy storage applications in building systems.

6.1.2 Identification of Stabilization Mechanisms of Dextran Sulfate Sodium Polyelectrolyte in Salt Hydrate Systems using Atomic Scale Techniques

Chapter 3 examines the stabilizing effect and provides explanation of the mechanism of stabilization of sodium sulfate decahydrate PCM by dextran sulfate sodium polyelectrolyte using atomic scale techniques such as neutron scattering and molecular dynamics simulation. Total neutron scattering confirmed the structural transformation of SSD and SSD-DSS mixtures when heated to the phase transition temperature. It was confirmed that the SSD melted, and the presence of DSS had no effect on the structural transformation. A decomposition of the pair distribution function, density profiles, mean square displacements, and potential energies was provided by Molecular Dynamics simulation. Simulations were conducted with two interaction potentials, Dreiding and Gromos, in order to more accurately characterize both phases of SSD. The simulations collectively characterize a phase transition in which the water of hydration migrates to the hydrate-polyelectrolyte interface. The water congregates around the polyelectrolyte's sulfonic acid groups. Due to the close proximity of the acid groups, a thin layer of water forms. This interfacial film is adequately stable so that water is relatively immobile and does not permeate further into the polyelectrolyte, at least on the timescale of these simulations. The interaction between the water of hydration and the polyelectrolyte is identified as the thermodynamic driving force for this stabilization. This research can influence the selection and design of novel PCM composites with enhanced thermal properties for long-term use in buildings and other commercial heating and cooling applications by disclosing the atomic mechanism of SSD stabilization by DSS.

6.1.3 Performance Enhancement Methods for Low-Cost Salt Hydrate Phase Change Materials Using Cellulose and Carbon Materials Mixtures

This chapter addresses the supercooling, low thermal conductivity challenges, and thermal performance enhancement of low-cost salt hydrate PCMs. It focuses on the use of strontium chloride hexahydrate (SCH), graphene nanoplatelet (GNP), and cellulose nanofibril (CNF) was investigated to improve the thermal energy storage (TES) performance of calcium chloride hexahydrate (CCH) by decreasing supercooling, increasing thermal conductivity, and increasing energy storage capacity, respectively. According to rheological characterizations, the addition of 1% CNF to CCH maximized viscosity improvement and enhanced solid-like rheological behavior.

The structural characterization of PCM composites indicates a physical mixing of the constituent components. It also verifies the amphiphilicity of CNF, which facilitates the surface attachment of GNP through hydrophobic interactions, allowing for the efficient dispersion throughout the PCM composite. The addition of SCH, a nucleating agent, reduced the supercooling of CCH from 20 °C to 3 °C. After 70 melt-freeze cycles, thermal analysis revealed that the PCM composite had a high latent heat of melting of 186 J/g, a phase transition temperature of 32 °C, and stable thermal characteristics. When CNF and GNP were added to pure CCH, its thermal conductivity rose by 114%. This improvement is due to the superior thermal performance of CNF and its efficient dispersion by CNF. The research focuses on the utilization of biodegradable nanocellulose in the production of PCM composites with enhanced performance.

6.1.4 Tailoring Of Thermal Properties of Low-Cost Salt Hydrate Phase Change Materials Using Eutectic Mixtures

In this chapter, the limitation in PCM options for near ambient temperature applications was addressed. It explored the feasibility of using eutectic $Na_2CO_3{\cdot}10H_2O$ and $Na_2SO_4{\cdot}10H_2O$ PCM combinations for improved thermal comfort in building infrastructure. The melting point is 25.18 °C, and the melting enthalpy is 187.46 J/g; this combination is made by combining $Na_2CO_3 \cdot 10H_2O$ and $Na_2SO_4 \cdot 10H_2O$, with a mass ratio of 50:50. After going through 10 consecutive melt/freeze cycles, 78% of the latent heat had been recovered from the eutectic mixture. This indicates that further enhancement methods are required for the stabilization of this eutectic mixture. ATR-IR and XRD tests show that the eutectic system's salts, $Na_2CO_3 \cdot 10H_2O$ and $Na_2SO_4 \cdot 10H_2O$, interact physically, leading to the eutectic effect and a lower melting point. All things considered, the eutectic PCM mixture has strong potential as a storage medium for use in climate control and near-ambient thermal energy storage applications.

6.2 Impact and Significance of this thesis

The transition to renewable energy sources necessitates the development and adoption of energy storage technologies for use in varieties of energy systems. One of the viable energy storage solutions is the thermal energy storage solution involving the utilization of phase change processes to store and release thermal energy. A notable class of materials for TES solution are the salt

hydrate PCMs, due to low-cost, non-flammability, and attractive energy storage density. However, despite these benefits, they are still plagued by key technical barriers that have limited their deployment, especially phase separation, high supercooling degree, and low thermal conductivity. This study contributes to advancing thermal energy storage research by addressing the aforementioned challenges and enabling the adoption of salt hydrates for diverse applications. Particularly, this work addresses the critical problems in low-cost salt hydrate PCMs thereby enhancing their stability, reliability and thermal performance for widespread adoption and utilization in heating, cooling, and air conditioning applications. The impact of these thesis is extensively discussed below:

Stabilization of PCM using polyelectrolyte additives

This study proposes a new and more effective stabilization method to prevent phase separation and improve the energy storage capacity of sodium sulfate decahydrate using sulfonated polyelectrolyte stabilization, as opposed to the conventional method of physical thickening. Polyelectrolytes have been widely used in the field of nanotechnology and food sciences for the stabilization of nanoparticles, colloids, and emulsions. There are relatively no reports on the use of polyelectrolytes to stabilize salt hydrate PCMs. This study is among the early study that utilized polyelectrolytes in the stabilization of sodium sulfate decahydrate PCMs. Therefore, this work could serve as a basis for the selection of other relevant polyelectrolytes for the reduction of phase segregation and enabling stabilization of different salt hydrates PCMs. Furthermore, the new polyelectrolyte-based PCMs with good thermal stability developed in this study are promising for integration into variety of latent heat thermal energy storage systems. The findings from this study relating to the structure-property-processing relationship of the salt hydrate PCMs could guide the design, analysis, and scale-up of PCM integrated TES systems for potential industry applications.

Stabilization mechanism of PCMs using atomic-scale techniques

Several studies have been reported on the experimental approaches toward addressing critical problems with salt hydrate but there are sparse studies that provides insight into the atomic structure and behavior of these PCMs. Therefore, this work advances the state of the art through the provision of new insight into the structure-property-processing relationships of PCMs at the

atomic level. Specifically, it provides an explanation of stabilization mechanism in polyelectrolyte-salt hydrate PCM mixtures using atomic scale techniques such as neutron pair distribution function techniques and molecular dynamics simulation. The fundamental understanding provided by this work could serve as a theoretical basis for the design of new and high-performing PCM materials based on polyelectrolyte stabilization for relevant applications in thermal energy storage systems.

Development of PCM mixtures for near-ambient temperature TES applications

This study also addresses the challenge of limited options of PCMs for near ambient TES applications through tailoring of phase change temperature of low-cost PCMs using eutectic mixing approach. The mixing of two or more salt hydrate at specific concentration ratio can provide new PCMs with phase change temperature suitable for thermal comfort in buildings and commercial office spaces. Also, the developed eutectic PCMs have the potential to be integrated in heat pump systems for large-scale thermal energy storage applications, especially in residential cooling and human comfort. In general, this work contributes to the decarbonization efforts of the global building sector, reduction in greenhouse gas emissions and decrease in carbon footprint through the storage and deployment of renewable sources of energy. This would help alleviate the negative effect of global climate change.

6.3 Limitations of the study

Despite the substantial impact of this study on PCM development and property enhancement, there are still major areas of improvement and hurdles to be crosses for the scalability and transition from lab to the market for various applications. A major challenge is the phase separation leading to instability of the energy storage capacity of PCMs after successive melt and freeze cycles. This work provides a step forward in addressing this phase separation issue through the use of polyelectrolytes to stabilize sodium sulfate decahydrate PCM up to 150 cycles. However, to enable the adoption of salt hydrate PCMs for long-term energy storage, stability must be ensured up to ~5,000 melt/freeze cycles.

Furthermore, the study used molecular dynamics simulation to provide key insight into key phenomena like the stabilization mechanism of SSD using sulfonated polyelectrolytes. To implement MD algorithms for atomistic simulations, there is a need for accurate interatomic potentials that correctly predicts the interactions among the atoms in the system. In this case, none

of the interatomic potentials used for the atomistic simulations (Drieding, and Gromos potentials) was able to predict the behavior of SSD in both solid and liquid phase effectively. The Drieding potential gave the best prediction of SSD in the liquid phase while the Gromos potential provided a better prediction of the behavior of SSD in the solid state. To enrich our fundamental understanding of salt hydrates, there is need for the generation of versatile interatomic potentials to predict the behavior of salt hydrate PCMs over various phases and conditions.

Also, the study aimed to address supercooling and low thermal conductivity issues in low-cost salt hydrate PCMs, especially calcium chloride hexahydrate. This objective was achieved using nucleators, graphene nanoplatelet, and cellulose nanofiber in the development of composite PCM mixtures with enhanced thermal performance. As much as thermal conductivity increased using graphene nanoplatelet, the enhancement level might still be insufficient for high thermal conductivity applications requiring the fast charging and discharging of PCMs (> 1 W/m.K). The use of higher thermal conductivity carbon materials like compressed expanded national graphite could further boost the thermal conductivity of salt hydrate PCMs.

Moreover, this study aimed to address the limited options of salt hydrate PCMs for near-ambient thermal energy storage applications in buildings. The study successfully reported the development of a binary salt hydrate PCM using eutectic mixing approach. This material has a suitable phase change temperature ~25 °C, which makes it promising for near-ambient TES applications. However, it is still unstable. This work only focused on the development of the PCM mixture using eutectic mixing but the stabilization of the PCM mixture was not explored. It is critical to stabilize these materials using effective additives such as polymeric thickeners and relevant polyelectrolytes to prevent phase separation and enhance the reliability of eutectic salt hydrate PCMs for long-term TES applications.

6.4 Recommendation for Future work

The development of stable low-cost PCMs for thermal energy application is an active research area which enables the decarbonization of our building and energy infrastructure. Several notable advances have been made towards the adoption of PCMs for diverse applications. However, there are still significant opportunities for leading more innovations in the field. It is important to emphasize that salt hydrate PCMs are notoriously unstable due to phase separation

and incongruent melting. It is important to channel significant research effort into investigating and providing more effective stabilization methods for various classes of PCMs, leading to the development of more stable, reliable, and high-performing PCMs for thermal energy storage applications. This way, the promise of PCMs can be realized through market penetration at a competitive scale to the electric storage technologies.

Furthermore, there are still limited options of PCMs that could be selected for near-ambient (20 – 25 °C) thermal energy storage applications. This is because, most PCMs have higher phase change temperature at which they store and release heat energy. To meet the requirements of near-ambient thermal energy storage, it is a need to develop novel, low-cost PCMs with suitable phase change temperatures in the 20 – 25 °C range. A proven approach to consider in the design of these PCMs is the eutectic mixing approach in which two or more salt hydrates are mixed at an appropriate concentration to form a stable eutectic PCM mixture with lower phase change temperature. This class of materials have prospect in applications related to human thermal comfort. Hence, it is important to drive innovation by finding effective ways to stabilize these materials and improve their thermal performance when integrated into TES devices.

Despite the numerous and well-established experimental approaches employed in the study and development of new PCMs, simulation techniques are still lagging. The use of advanced simulation techniques has strong potential in providing key insight into the structure-property-processing relationships in salt hydrate PCMs which could be beneficial for our understanding of PCMs. Also, the lessons learnt from the MD simulations could guide the design and discovery of novel salt hydrate PCMs with extended stability. Therefore, salt hydrate PCM modelling, and simulation efforts should be intensified to accelerate the discovery of promising salt hydrate PCM mixtures for TES applications.

TES has witnessed major progress in the research and development of promising materials with suitable properties. However, to ensure tangible progress in the decarbonization efforts using TES, it is important to channel significant effort to demonstration and deployment of these high-performance PCMs in energy systems. This will include the integration of PCMs into large-scale devices like heat pumps, heat exchangers, among others. The demonstration and deployment efforts are critical to the widespread adoption and utilization of TES devices for a decarbonized energy systems and economy. In all, the research and development effort in addressing challenges

related to TES requires a holistic approach. This requires the synergy between fundamental and applied research with strong collaboration networks among key stakeholders including research institutions, government, and industry partners. This will accelerate the development and commercialization of TES as a renewable energy storage solution for decarbonization of the entire energy infrastructure. Looking at the big picture, there is no “one size fits all” approach to addressing the critical challenges and enhancing the advancement of this technology. The development of several viable approaches for the enhancing the adoption of TES is warranted. This dissertation provides a step forward in addressing some parts of the enormous challenges related to TES technology. Hopefully, this study will serve as a springboard for future studies that improves the efficiency, safety, dependability, and reliability of renewable energy sources thereby leading to energy security for humanity.

LIST OF REFERENCES

[1] J. Diefenderfer, M. assumptions Vipin Arora, and L. E. Singer, “International Energy Outlook 2016,” pp. 202–586, 2040, Accessed: Feb. 21, 2022. [Online]. Available: https://www.osti.gov/servlets/purl/1296780

[2] W. Li, J. J. Klemeš, Q. Wang, and M. Zeng, “Salt hydrate–based gas-solid thermochemical energy storage: Current progress, challenges, and perspectives,” *Renew. Sustain. Energy Rev.*, vol. 154, p. 111846, Feb. 2022, doi: 10.1016/J.RSER.2021.111846.

[3] S. Bennici, T. Polimann, M. Ondarts, E. Gonze, C. Vaulot, and N. Le Pierrès, “Long-term impact of air pollutants on thermochemical heat storage materials,” *Renew. Sustain. Energy Rev.*, vol. 117, Jan. 2020, doi: 10.1016/J.RSER.2019.109473.

[4] Z. Ding, W. Wu, and M. Leung, “Advanced/hybrid thermal energy storage technology: material, cycle, system and perspective,” *Renew. Sustain. Energy Rev.*, vol. 145, Jul. 2021, doi: 10.1016/J.RSER.2021.111088.

[5] N. I. Ibrahim, F. A. Al-Sulaiman, and F. N. Ani, “Solar absorption systems with integrated absorption energy storage–A review,” *Renew. Sustain. Energy Rev.*, vol. 82, pp. 1602–1610, Feb. 2018, doi: 10.1016/J.RSER.2017.07.005.

[6] A. Bilal, B. Jamil, N. U. Haque, and M. A. Ansari, “Investigating the effect of pumice stones sensible heat storage on the performance of a solar still,” *Groundw. Sustain. Dev.*, vol. 9, p. 100228, Oct. 2019, doi: 10.1016/j.gsd.2019.100228.

[7] S. Ayyappan, · K Mayilsamy, and · V V Sreenarayanan, “Performance improvement studies in a solar greenhouse drier using sensible heat storage materials,” *Heat Mass Transf.*, vol. 52, pp. 459–467, 2016, doi: 10.1007/s00231-015-1568-5.

[8] J. Sunku Prasad, P. Muthukumar, F. Desai, D. N. Basu, and M. M. Rahman, “A critical review of high-temperature reversible thermochemical energy storage systems,” *Appl. Energy*, vol. 254, p. 113733, Nov. 2019, doi: 10.1016/j.apenergy.2019.113733.

[9] Z. Khan, Z. Khan, and A. Ghafoor, “A review of performance enhancement of PCM based latent heat storage system within the context of materials, thermal stability and compatibility,” *Energy Convers. Manag.*, vol. 115, pp. 132–158, 2016, doi: 10.1016/j.enconman.2016.02.045.

[10] A. Dinker, M. Agarwal, and G. D. Agarwal, “Heat storage materials, geometry and

applications: A review," *J. Energy Inst.*, vol. 90, no. 1, pp. 1–11, Feb. 2017, doi: 10.1016/j.joei.2015.10.002.

[11] B. K. Purohit and V. S. Sistla, "Inorganic salt hydrate for thermal energy storage application: A review," *Energy Storage*, vol. 3, no. 2, pp. 1–26, 2021, doi: 10.1002/est2.212.

[12] T. Xu, E. N. Humire, J. N. W. Chiu, and S. Sawalha, "Numerical thermal performance investigation of a latent heat storage prototype toward effective use in residential heating systems," *Appl. Energy*, vol. 278, p. 115631, Nov. 2020, doi: 10.1016/J.APENERGY.2020.115631.

[13] N. Kumar, J. Hirschey, T. J. LaClair, K. R. Gluesenkamp, and S. Graham, "Review of stability and thermal conductivity enhancements for salt hydrates," *J. Energy Storage*, vol. 24, p. 100794, Aug. 2019, doi: 10.1016/j.est.2019.100794.

[14] H. Nazir *et al.*, "Recent developments in phase change materials for energy storage applications: A review," *Int. J. Heat Mass Transf.*, vol. 129, pp. 491–523, 2019, doi: 10.1016/j.ijheatmasstransfer.2018.09.126.

[15] B. P. Jelle and S. E. Kalnæs, "Phase Change Materials for Application in Energy-Efficient Buildings," *Cost-Effective Energy Effic. Build. Retrofit. Mater. Technol. Optim. Case Stud.*, pp. 57–118, Jan. 2017, doi: 10.1016/B978-0-08-101128-7.00003-4.

[16] B. Xie, C. Li, B. Zhang, L. Yang, G. Xiao, and J. Chen, "Evaluation of stearic acid/coconut shell charcoal composite phase change thermal energy storage materials for tankless solar water heater," *Energy Built Environ.*, vol. 1, no. 2, pp. 187–198, Apr. 2020, doi: 10.1016/J.ENBENV.2019.08.003.

[17] A. Najafian, F. Haghighat, and A. Moreau, "Integration of PCM in domestic hot water tanks: Optimization for shifting peak demand," *Energy Build.*, vol. 106, pp. 59–64, Nov. 2015, doi: 10.1016/J.ENBUILD.2015.05.036.

[18] A. Aljehani, S. A. K. Razack, L. Nitsche, and S. Al-Hallaj, "Design and optimization of a hybrid air conditioning system with thermal energy storage using phase change composite," *Energy Convers. Manag.*, vol. 169, pp. 404–418, Aug. 2018, doi: 10.1016/j.enconman.2018.05.040.

[19] X. J. Shi and P. Zhang, "Cold storage by tetra-n-butyl ammonium bromide clathrate

hydrate slurry generated with different storage approaches at 40 wt% initial aqueous solution concentration," *Int. J. Refrig.*, vol. 42, pp. 77–89, Jun. 2014, doi: 10.1016/j.ijrefrig.2014.02.002.

[20] S. Shi *et al.*, "Non-steady experimental investigation on an integrated thermal management system for power battery with phase change materials," *Energy Convers. Manag.*, vol. 138, pp. 84–96, Apr. 2017, doi: 10.1016/j.enconman.2017.01.069.

[21] J. Krishna, P. S. Kishore, and A. B. Solomon, "Heat pipe with nano enhanced-PCM for electronic cooling application," *Exp. Therm. Fluid Sci.*, vol. 81, pp. 84–92, Feb. 2017, doi: 10.1016/j.expthermflusci.2016.10.014.

[22] S. Xu, Lemington, R. Z. Wang, L. Wang, and J. Zhu, "A zeolite 13X/magnesium sulfate–water sorption thermal energy storage device for domestic heating," *Energy Convers. Manag.*, vol. 171, pp. 98–109, Sep. 2018, doi: 10.1016/j.enconman.2018.05.077.

[23] S. Singh, K. K. Gaikwad, and Y. S. Lee, "Phase change materials for advanced cooling packaging," *Environ. Chem. Lett.*, vol. 16, no. 3, pp. 845–859, Sep. 2018, doi: 10.1007/s10311-018-0726-7.

[24] L. Miró, J. Gasia, and L. F. Cabeza, "Thermal energy storage (TES) for industrial waste heat (IWH) recovery: A review," *Appl. Energy*, vol. 179, pp. 284–301, Oct. 2016, doi: 10.1016/j.apenergy.2016.06.147.

[25] H. Akeiber *et al.*, "A review on phase change material (PCM) for sustainable passive cooling in building envelopes," *Renew. Sustain. Energy Rev.*, vol. 60, pp. 1470–1497, Jul. 2016, doi: 10.1016/J.RSER.2016.03.036.

[26] S. S. Magendran *et al.*, "Synthesis of organic phase change materials (PCM) for energy storage applications: A review," *Nano-Structures & Nano-Objects*, vol. 20, p. 100399, 2019, doi: 10.1016/j.nanoso.2019.100399.

[27] A. Efimova, S. Pinnau, M. Mischke, C. Breitkopf, M. Ruck, and P. Schmidt, "Development of salt hydrate eutectics as latent heat storage for air conditioning and cooling," *Thermochim. Acta*, vol. 575, pp. 276–278, Jan. 2014, doi: 10.1016/J.TCA.2013.11.011.

[28] A. M. Khudhair and M. M. Farid, "A review on energy conservation in building applications with thermal storage by latent heat using phase change materials," *Energy*

Convers. Manag., vol. 45, no. 2, pp. 263–275, Jan. 2004, doi: 10.1016/S0196-8904(03)00131-6.

[29] C. Sunliang, "State of the art thermal energy storage solutions for high performance buildings," 2010.

[30] A. Sharma, V. V. Tyagi, C. R. Chen, and D. Buddhi, "Review on thermal energy storage with phase change materials and applications," *Renew. Sustain. Energy Rev.*, vol. 13, no. 2, pp. 318–345, Feb. 2009, doi: 10.1016/j.rser.2007.10.005.

[31] H. P. Garg, S. C. Mullick, and A. K. Bhargava, "Latent Heat or Phase Change Thermal Energy Storage," *Sol. Therm. Energy Storage*, pp. 154–291, 1985, doi: 10.1007/978-94-009-5301-7_3.

[32] G. Wang *et al.*, "Review on sodium acetate trihydrate in flexible thermal energy storages: Properties, challenges and applications," *J. Energy Storage*, vol. 40, no. June, 2021, doi: 10.1016/j.est.2021.102780.

[33] X. Dong, J. Mao, S. Geng, Y. Li, P. Hou, and H. Lian, "Study on performance optimization of sodium sulfate decahydrate phase change energy storage materials," *J. Therm. Anal. Calorim.*, vol. 143, no. 6, pp. 3923–3934, 2021, doi: 10.1007/s10973-020-09306-6.

[34] Y. Li *et al.*, "Stable salt hydrate-based thermal energy storage materials," *Compos. Part B Eng.*, vol. 233, p. 109621, Mar. 2022, doi: 10.1016/J.COMPOSITESB.2022.109621.

[35] Biswas DR, "Thermal energy storage using sodium sulfate decahydrate and water," 1977. Accessed: Apr. 14, 2022. [Online]. Available: https://escholarship.org/uc/item/59x1d2xv

[36] N. Beaupere, U. Soupremanien, and L. Zalewski, "Nucleation triggering methods in supercooled phase change materials (PCM), a review," *Thermochim. Acta*, vol. 670, pp. 184–201, Dec. 2018, doi: 10.1016/j.tca.2018.10.009.

[37] Q. Zhang, F. Ma, W. Tan, L. Liu, M. Jing, and T. Sun, "Enhanced heat storage performance of CaCl2·6H2O using BN nanosheet as an additive," *Heat Mass Transf. und Stoffuebertragung*, no. 0123456789, 2022, doi: 10.1007/s00231-022-03302-2.

[38] "BENEFIT_FY19_FOA_-_Amendment_000001.pdf."

[39] J. R. Hirschey *et al.*, "Review of Low-Cost Organic and Inorganic Phase Change Review of Low-Cost Organic and Inorganic Phase Change Materials with Phase Change

Temperature between 0°C and 65°C Materials with Phase Change Temperature between 0°C and 65°C Tugba Turnaoglu Oak Ridge National Lab ‘Review of Low-Cost Organic and Inorganic Phase Change Materials with Phase Change Temperature between 0°C and 65°C’ Review of Low-Cost Organic and Inorganic Phase Change Materials with Phase Change Temperature between 0°C and 65°C,” p. 2021, 2021, Accessed: Mar. 29, 2023. [Online]. Available: https://docs.lib.purdue.edu/ihpbc/389

[40] H. Nazir *et al.*, “International Journal of Heat and Mass Transfer Recent developments in phase change materials for energy storage applications : A review,” *Int. J. Heat Mass Transf.*, vol. 129, pp. 491–523, 2019, doi: 10.1016/j.ijheatmasstransfer.2018.09.126.

[41] N. Kumar, J. Hirschey, T. J. LaClair, K. R. Gluesenkamp, and S. Graham, “Review of stability and thermal conductivity enhancements for salt hydrates,” *J. Energy Storage*, vol. 24, p. 100794, Aug. 2019, doi: 10.1016/j.est.2019.100794.

[42] G. Gholamibozanjani and M. Farid, “A comparison between passive and active PCM systems applied to buildings,” *Renew. Energy*, vol. 162, pp. 112–123, 2020, doi: 10.1016/j.renene.2020.08.007.

[43] N. Choubineh, H. Jannesari, and A. Kasaeian, “Experimental study of the effect of using phase change materials on the performance of an air-cooled photovoltaic system,” *Renew. Sustain. Energy Rev.*, vol. 101, no. October 2018, pp. 103–111, Mar. 2019, doi: 10.1016/j.rser.2018.11.001.

[44] C. S. Herrick, “Melt-freeze-cycle life-testing of Glauber’s salt in a rolling cylinder heat store,” *Sol. Energy*, vol. 28, no. 2, pp. 99–104, 1982, doi: 10.1016/0038-092X(82)90288-2.

[45] H. W. Ryu, S. W. Woo, B. C. Shin, and S. D. Kim, “Prevention of supercooling and stabilization of inorganic salt hydrates as latent heat storage materials,” *Sol. Energy Mater. Sol. Cells*, vol. 27, no. 2, pp. 161–172, 1992, doi: 10.1016/0927-0248(92)90117-8.

[46] M. Goswami *et al.*, “Understanding supercooling mechanism in sodium sulfate decahydrate phase-change material,” *J. Appl. Phys.*, vol. 129, no. 24, p. 245109, Jun. 2021, doi: 10.1063/5.0049512.

[47] S. Marks, “An investigation of the thermal energy storage capacity of Glauber’s salt with respect to thermal cycling,” *Sol. Energy*, vol. 25, no. 3, pp. 255–258, 1980, doi:

10.1016/0038-092X(80)90332-1.

[48] Ö. Gök, M. Ö. Yilmaz, and H. Ö. Paksoy, “Stabilization of Glauber’s salt for latent heat storage,” pp. 1–10, 2004.

[49] C. Li, B. Zhang, B. Xie, X. Zhao, and J. Chen, “Tailored phase change behavior of Na2SO4·10H2O/expanded graphite composite for thermal energy storage,” *Energy Convers. Manag.*, vol. 208, p. 112586, Mar. 2020, doi: 10.1016/j.enconman.2020.112586.

[50] X. Dong, J. Mao, S. Geng, Y. Li, P. Hou, and H. Lian, “Study on performance optimization of sodium sulfate decahydrate phase change energy storage materials,” *J. Therm. Anal. Calorim.*, vol. 143, no. 6, pp. 3923–3934, Mar. 2021, doi: 10.1007/s10973-020-09306-6.

[51] C. Alkan *et al.*, “Polyvinyl Alcohol-salt Hydrate Mixtures as Passive Thermal Energy Storage Systems,” *Energy Procedia*, vol. 91, pp. 1012–1017, Jun. 2016, doi: 10.1016/j.egypro.2016.06.269.

[52] Z. Zhang, Y. Lian, X. Xu, X. Xu, G. Fang, and M. Gu, “Synthesis and characterization of microencapsulated sodium sulfate decahydrate as phase change energy storage materials,” *Appl. Energy*, vol. 255, p. 113830, Dec. 2019, doi: 10.1016/j.apenergy.2019.113830.

[53] F. Cheng, J. W. Betts, S. M. Kelly, J. Schaller, and T. Heinze, “Synthesis and antibacterial effects of aqueous colloidal solutions of silver nanoparticles using aminocellulose as a combined reducing and capping reagent,” *Green Chem.*, vol. 15, no. 4, pp. 989–998, 2013, doi: 10.1039/c3gc36831a.

[54] M. Fang, X. Zhang, J. Ji, W. Hua, Y. Zhao, and J. Liang, “Optimal selection of thickeners for the phase change material of Na2S2O3·5H2O–CH3COONa·3H2O,” *J. Therm. Anal. Calorim.*, no. 0123456789, 2021, doi: 10.1007/s10973-021-11113-6.

[55] K. Oh, S. Kwon, W. Xu, X. Wang, and M. Toivakka, “Effect of micro- and nanofibrillated cellulose on the phase stability of sodium sulfate decahydrate based phase change material,” *Cellulose*, vol. 27, no. 9, pp. 5003–5016, 2020, doi: 10.1007/s10570-020-03121-w.

[56] S. A. Vesnebolotskaya, N. G. Bel’Nikevich, and T. V. Budtova, “Influence of surface layer formation on swelling of polyelectrolytic hydrogels in aqueous salt solutions,” *Russ. J. Appl. Chem.*, vol. 83, no. 11, pp. 2006–2010, 2010, doi: 10.1134/S1070427210110212.

[57] G. Li, B. Zhang, X. Li, Y. Zhou, Q. Sun, and Q. Yun, “The preparation, characterization and modification of a new phase change material: CaCl2·6H2O-MgCl2· 6H2O eutectic hydrate salt,” *Sol. Energy Mater. Sol. Cells*, vol. 126, pp. 51–55, 2014, doi: 10.1016/j.solmat.2014.03.031.

[58] M. C. Ndukwu, L. Bennamoun, F. I. Abam, A. B. Eke, and D. Ukoha, “Energy and exergy analysis of a solar dryer integrated with sodium sulfate decahydrate and sodium chloride as thermal storage medium,” *Renew. Energy*, vol. 113, pp. 1182–1192, 2017, doi: 10.1016/j.renene.2017.06.097.

[59] S. Peng, J. Huang, T. Wang, and P. Zhu, “Effect of fumed silica additive on supercooling, thermal reliability and thermal stability of Na 2 HPO 4 ·12H 2 O as inorganic PCM,” *Thermochim. Acta*, vol. 675, no. July 2018, pp. 1–8, 2019, doi: 10.1016/j.tca.2019.02.013.

[60] X. Liu, L. Li, M. Ye, Y. Xue, and S. Chen, “Polyaniline:poly(sodium 4-styrenesulfonate)-stabilized gold nanoparticles as efficient, versatile catalysts,” *Nanoscale*, vol. 6, no. 10, pp. 5223–5229, 2014, doi: 10.1039/C4NR00328D.

[61] H. A. Levy and G. C. Lisensky, “Crystal structures of sodium sulfate decahydrate (Glauber’s salt) and sodium tetraborate decahydrate (borax). Redetermination by neutron diffraction,” *Acta Crystallogr. Sect. B Struct. Crystallogr. Cryst. Chem.*, vol. 34, no. 12, pp. 3502–3510, Dec. 1978, doi: 10.1107/S0567740878011504.

[62] Z. Zhang, Y. Lian, X. Xu, X. Xu, G. Fang, and M. Gu, “Synthesis and characterization of microencapsulated sodium sulfate decahydrate as phase change energy storage materials,” *Appl. Energy*, vol. 255, p. 113830, Dec. 2019, doi: 10.1016/j.apenergy.2019.113830.

[63] K. Oh, Z. Shen, S. Kwon, and M. Toivakka, “Thermal properties of graphite/salt hydrate phase change material stabilized by nanofibrillated cellulose,” *Cellulose*, vol. 28, no. 11, pp. 6845–6856, 2021, doi: 10.1007/s10570-021-03936-1.

[64] W. He, S. Jiang, Q. Zhang, and M. Pan, “Isolation and characterization of cellulose nanofibers from Bambusa rigida,” *BioResources*, vol. 8, no. 4, pp. 5678–5689, 2013, doi: 10.15376/biores.8.4.5678-5689.

[65] R. Baigorri, J. M. García-Mina, and G. González-Gaitano, “Supramolecular association induced by Fe(III) in low molecular weight sodium polyacrylate,” *Colloids Surfaces A Physicochem. Eng. Asp.*, vol. 292, no. 2–3, pp. 212–216, 2007, doi:

10.1016/j.colsurfa.2006.06.027.

[66] Y. Liu, K. Yu, X. Gao, M. Ren, M. Jia, and Y. Yang, “Enhanced thermal properties of hydrate salt/poly (acrylate sodium) copolymer hydrogel as form-stable phase change material via incorporation of hydroxyl carbon nanotubes,” *Sol. Energy Mater. Sol. Cells*, vol. 208, p. 110387, May 2020, doi: 10.1016/j.solmat.2019.110387.

[67] S. Li *et al.*, “Potassium Polyacrylate-Based Gel Polymer Electrolyte for Practical Zn-Ni Batteries,” *ACS Appl. Mater. Interfaces*, vol. 14, no. 20, pp. 22847–22857, 2022, doi: 10.1021/acsami.1c20999.

[68] W. Xie *et al.*, “A new intumescent insulation emergency material for thermal protection of storage tanks –potassium polyacrylate & organic modified hectorite & intumescent flame retardant,” *J. Loss Prev. Process Ind.*, vol. 76, no. December 2021, p. 104735, 2022, doi: 10.1016/j.jlp.2022.104735.

[69] A. Rani, S. Monga, M. Bansal, and A. Sharma, “Bionanocomposites reinforced with cellulose nanofibers derived from sugarcane bagasse,” *Polym. Compos.*, vol. 39, pp. E55–E64, 2018, doi: 10.1002/pc.24112.

[70] S. Ventura-Cruz and A. Tecante, “Extraction and characterization of cellulose nanofibers from Rose stems (Rosa spp.),” *Carbohydr. Polym.*, vol. 220, no. May, pp. 53–59, 2019, doi: 10.1016/j.carbpol.2019.05.053.

[71] Z. Khatri, R. A. Arain, A. W. Jatoi, G. Mayakrishnan, K. Wei, and I. S. Kim, “Dyeing and characterization of cellulose nanofibers to improve color yields by dual padding method,” *Cellulose*, vol. 20, no. 3, pp. 1469–1476, 2013, doi: 10.1007/s10570-013-9893-7.

[72] G. Wang, B. Wang, J. Park, Y. Wang, B. Sun, and J. Yao, “Highly efficient and large-scale synthesis of graphene by electrolytic exfoliation,” *Carbon N. Y.*, vol. 47, no. 14, pp. 3242–3246, Nov. 2009, doi: 10.1016/j.carbon.2009.07.040.

[73] L. Chen, C. Yuan, H. Dou, B. Gao, S. Chen, and X. Zhang, “Synthesis and electrochemical capacitance of core–shell poly (3,4-ethylenedioxythiophene)/poly (sodium 4-styrenesulfonate)-modified multiwalled carbon nanotube nanocomposites,” *Electrochim. Acta*, vol. 54, no. 8, pp. 2335–2341, Mar. 2009, doi: 10.1016/j.electacta.2008.10.071.

[74] W. Chen, Q. Feng, G. Zhang, Q. Yang, C. Zhang, and F. Xu, “The flotation separation of

scheelite from calcite and fluorite using dextran sulfate sodium as depressant," *Int. J. Miner. Process.*, vol. 169, pp. 53–59, 2017, doi: 10.1016/j.minpro.2017.10.005.

[75] D. S. Bodas and P. P. Ige, "Central composite rotatable design for optimization of budesonide-loaded cross-linked chitosan–dextran sulfate nanodispersion: characterization, in vitro diffusion and aerodynamic study," *Drug Dev. Ind. Pharm.*, vol. 45, no. 7, pp. 1193–1204, 2019, doi: 10.1080/03639045.2019.1606823.

[76] A. I. Koponen, "The effect of consistency on the shear rheology of aqueous suspensions of cellulose micro- and nanofibrils: a review," *Cellulose*, vol. 27, no. 4, pp. 1879–1897, 2020, doi: 10.1007/s10570-019-02908-w.

[77] J. Labanda, J. Sabaté, and J. Llorens, "Rheology changes of Laponite aqueous dispersions due to the addition of sodium polyacrylates of different molecular weights," *Physicochem. Eng. Asp.*, vol. 301, pp. 8–15, 2007, doi: 10.1016/j.colsurfa.2007.01.011.

[78] P. Rezayati Charani, M. Dehghani-Firouzabadi, E. Afra, and A. Shakeri, "Rheological characterization of high concentrated MFC gel from kenaf unbleached pulp," *Cellulose*, vol. 20, no. 2, pp. 727–740, Apr. 2013, doi: 10.1007/s10570-013-9862-1.

[79] G. Q. Qi *et al.*, "Polyethylene glycol based shape-stabilized phase change material for thermal energy storage with ultra-low content of graphene oxide," *Sol. Energy Mater. Sol. Cells*, vol. 123, pp. 171–177, 2014, doi: 10.1016/j.solmat.2014.01.024.

[80] Z. Shen, S. Kwon, H. L. Lee, M. Toivakka, and K. Oh, "Enhanced thermal energy storage performance of salt hydrate phase change material: Effect of cellulose nanofibril and graphene nanoplatelet," *Sol. Energy Mater. Sol. Cells*, vol. 225, no. February, p. 111028, Jun. 2021, doi: 10.1016/j.solmat.2021.111028.

[81] T. Wang, N. Wu, H. Li, Q.-L. Lu, and Y. Jiang, "Preparation and properties of a form-stable phase-change hydrogel for thermal energy storage," *J. Appl. Polym. Sci.*, vol. 133, no. 34, Sep. 2016, doi: 10.1002/app.43836.

[82] M. El Achaby, F. Z. Arrakhiz, S. Vaudreuil, E. M. Essassi, A. Qaiss, and M. Bousmina, "Preparation and characterization of melt-blended graphene nanosheets-poly(vinylidene fluoride) nanocomposites with enhanced properties," *J. Appl. Polym. Sci.*, vol. 127, no. 6, pp. 4697–4707, Mar. 2013, doi: 10.1002/APP.38081.

[83] G. Bahsi Kaya, Y. Kim, K. Callahan, and S. Kundu, "Microencapsulated phase change

material via Pickering emulsion stabilized by cellulose nanofibrils for thermal energy storage," *Carbohydr. Polym.*, vol. 276, p. 118745, Jan. 2022, doi: 10.1016/j.carbpol.2021.118745.

[84] J. Hirschey *et al.*, "Effect of expanded graphite on the thermal conductivity of sodium sulfate decahydrate (Na2SO4·10H2O) phase change composites," *J. Energy Storage*, vol. 52, no. PB, p. 104949, Aug. 2022, doi: 10.1016/j.est.2022.104949.

[85] C. Li, B. Zhang, B. Xie, X. Zhao, and J. Chen, "Tailored phase change behavior of Na2SO4·10H2O/expanded graphite composite for thermal energy storage," *Energy Convers. Manag.*, vol. 208, p. 112586, Mar. 2020, doi: 10.1016/j.enconman.2020.112586.

[86] B. Fais, N. Sabio, and N. Strachan, "The critical role of the industrial sector in reaching long-term emission reduction, energy efficiency and renewable targets," *Appl. Energy*, vol. 162, pp. 699–712, Jan. 2016, doi: 10.1016/J.APENERGY.2015.10.112.

[87] S. Chen, P. Liu, and Z. Li, "Low carbon transition pathway of power sector with high penetration of renewable energy," *Renew. Sustain. Energy Rev.*, vol. 130, p. 109985, 2020, doi: 10.1016/j.rser.2020.109985.

[88] J. Pereira da Cunha and P. Eames, "Thermal energy storage for low and medium temperature applications using phase change materials – A review," *Appl. Energy*, vol. 177, pp. 227–238, Sep. 2016, doi: 10.1016/j.apenergy.2016.05.097.

[89] R. Zeinelabdein, S. Omer, and G. Gan, "Critical review of latent heat storage systems for free cooling in buildings," *Renew. Sustain. Energy Rev.*, vol. 82, pp. 2843–2868, Feb. 2018, doi: 10.1016/J.RSER.2017.10.046.

[90] A. Raul, M. Jain, S. Gaikwad, and S. K. Saha, "Modelling and experimental study of latent heat thermal energy storage with encapsulated PCMs for solar thermal applications," *Appl. Therm. Eng.*, vol. 143, pp. 415–428, Oct. 2018, doi: 10.1016/J.APPLTHERMALENG.2018.07.123.

[91] H. Xu, A. Romagnoli, J. Y. Sze, and X. Py, "Application of material assessment methodology in latent heat thermal energy storage for waste heat recovery," *Appl. Energy*, vol. 187, pp. 281–290, Feb. 2017, doi: 10.1016/J.APENERGY.2016.11.070.

[92] C. Y. Zhao, Y. Ji, and Z. Xu, "Investigation of the Ca(NO 3) 2-NaNO 3 mixture for latent heat storage," 2015, doi: 10.1016/j.solmat.2015.04.005.

[93] S. Marks, “An investigation of the thermal energy storage capacity of Glauber’s salt with respect to thermal cycling,” *Sol. Energy*, vol. 25, no. 3, pp. 255–258, Jan. 1980, doi: 10.1016/0038-092X(80)90332-1.

[94] S. B. Marks, “The effect of crystal size on the thermal energy storage capacity of thickened Glauber’s Salt,” vol. 30, no. 1, pp. 45–49, 1983.

[95] E. Org, “Lawrence Berkeley National Laboratory Recent Work Title THERMAL ENERGY STORAGE USING SODIUM SULFATE DECAHYDRATE and WATER Publication Date,” 1975, Accessed: Mar. 31, 2023. [Online]. Available: https://escholarship.org/uc/item/59x1d2xv

[96] L. Cong, B. Zou, A. Palacios, M. E. Navarro, G. Qiao, and Y. Ding, “Thickening and gelling agents for formulation of thermal energy storage materials – A critical review,” *Renew. Sustain. Energy Rev.*, vol. 155, no. October 2021, 2022, doi: 10.1016/j.rser.2021.111906.

[97] L. Tiemei *et al.*, “Sodium Polyacrylate/Sodium Sulfate Decahydrate Phase Change Composites,” *J. Funct. Polym.*, vol. 33, no. 2, pp. 157–164, Apr. 2020, doi: 10.14133/J.CNKI.1008-9357.20190301002.

[98] L. F. Cabeza, G. Svensson, S. Hiebler, and H. Mehling, “Thermal performance of sodium acetate trihydrate thickened with different materials as phase change energy storage material,” *Appl. Therm. Eng.*, vol. 23, no. 13, pp. 1697–1704, Sep. 2003, doi: 10.1016/S1359-4311(03)00107-8.

[99] M. Riahinezhad, N. Kazemi, N. McManus, and A. Penlidis, “Effect of ionic strength on the reactivity ratios of acrylamide/acrylic acid (sodium acrylate) copolymerization,” *J. Appl. Polym. Sci.*, vol. 131, no. 20, Oct. 2014, doi: 10.1002/APP.40949.

[100] Y. E. Milián, A. Gutiérrez, M. Grágeda, and S. Ushak, “A review on encapsulation techniques for inorganic phase change materials and the influence on their thermophysical properties,” *Renew. Sustain. Energy Rev.*, vol. 73, no. January, pp. 983–999, 2017, doi: 10.1016/j.rser.2017.01.159.

[101] A. Sankar Deepa and A. Tewari, “Phase transition behaviour of hydrated Glauber’s salt based phase change materials and the effect of ionic salt additives: A molecular dynamics study,” *Comput. Mater. Sci.*, vol. 203, no. May 2021, pp. 1–8, 2022, doi:

10.1016/j.commatsci.2021.111112.

[102] J. Neuefeind, M. Feygenson, J. Carruth, R. Hoffmann, and K. K. Chipley, “The Nanoscale Ordered MAterials Diffractometer NOMAD at the Spallation Neutron Source SNS,” *Nucl. Instruments Methods Phys. Res. Sect. B Beam Interact. with Mater. Atoms*, vol. 287, pp. 68–75, Sep. 2012, doi: 10.1016/j.nimb.2012.05.037.

[103] N. W. Mcnutt, O. Rios, M. Feygenson, T. E. Proffen, and D. J. Keffer, “Structural analysis of lignin-derived carbon composite anodes,” *J. Appl. Cryst*, vol. 47, pp. 1577–1584, 2014, doi: 10.1107/S1600576714014666.

[104] S. Plimpton, “Fast Parallel Algorithms for Short-Range Molecular Dynamics for the United States Department of Energy under Contract DE.ACO4-76DPOO789,” *J. Comput. Phys.*, vol. 117, pp. 1–19, 1995.

[105] M. Yu, H. A. Every, W. Jiskoot, G. J. Witkamp, and W. Buijs, “Molecular structure of dextran sulphate sodium in aqueous environment,” *J. Mol. Struct.*, vol. 1156, pp. 320–329, 2018, doi: 10.1016/j.molstruc.2017.11.090.

[106] M. D. Hanwell, D. E. Curtis, D. C. Lonie, T. Vandermeersch, E. Zurek, and G. R. Hutchison, “Avogadro: an advanced semantic chemical editor, visualization, and analysis platform,” *J. Cheminformatics 2012 41*, vol. 4, no. 1, pp. 1–17, Aug. 2012, doi: 10.1186/1758-2946-4-17.

[107] S. L. Mayo, B. D. Olafson, and W. A. G. Iii, “DREIDING: A Generic Force Field for Molecular Simulations,” *J. Phys. Chem*, vol. 94, p. 91101, 1990, Accessed: Mar. 27, 2023. [Online]. Available: https://pubs.acs.org/sharingguidelines

[108] N. Schmid *et al.*, “Definition and testing of the GROMOS force-field versions 54A7 and 54B7,” *Eur. Biophys. J. 2011 407*, vol. 40, no. 7, pp. 843–856, Apr. 2011, doi: 10.1007/S00249-011-0700-9.

[109] H. J. C. Berendsen, J. R. Grigera, and T. P. Straatsma, “The Missing Term in Effective Pair Potentials1,” *J. Phys. Chem*, vol. 91, pp. 6269–6271, 1987, Accessed: Apr. 12, 2022. [Online]. Available: https://pubs.acs.org/sharingguidelines

[110] T. L. Christiansen, S. R. Cooper, and K. M. Ø. Jensen, “There’s no place like real-space: elucidating size-dependent atomic structure of nanomaterials using pair distribution function analysis,” 2020, doi: 10.1039/d0na00120a.

[111] S. J. L. Billinge, “The rise of the X-ray atomic pair distribution function method: a series of fortunate events.,” *Philos. Trans. A. Math. Phys. Eng. Sci.*, vol. 377, no. 2147, p. 20180413, Jun. 2019, doi: 10.1098/rsta.2018.0413.

[112] X. Wang, S. Tan, X.-Q. Yang, and E. Hu, “Pair distribution function analysis: Fundamentals and application to battery materials,” *Chinese Phys. B*, vol. 29, no. 2, p. 028802, Feb. 2020, doi: 10.1088/1674-1056/ab6656.

[113] Y. Li *et al.*, “Stable salt hydrate-based thermal energy storage materials,” *Compos. Part B Eng.*, vol. 233, no. January, p. 109621, Mar. 2022, doi: 10.1016/j.compositesb.2022.109621.

[114] S. S. Jang *et al.*, “Molecular dynamics study of a surfactant-mediated decane-water interface: Effect of molecular architecture of alkyl benzene sulfonate,” *J. Phys. Chem. B*, vol. 108, no. 32, pp. 12130–12140, 2004, doi: 10.1021/jp048773n.

[115] Z. Rao, S. Wang, and F. Peng, “Self diffusion and heat capacity of n-alkanes based phase change materials: A molecular dynamics study,” *Int. J. Heat Mass Transf.*, vol. 64, pp. 581–589, 2013, doi: 10.1016/j.ijheatmasstransfer.2013.05.017.

[116] M. Sun *et al.*, “Experimental and molecular dynamic simulation of supercooling phenomenon of sodium acetate trihydrate,” *J. Energy Storage*, vol. 62, no. December 2022, p. 106956, 2023, doi: 10.1016/j.est.2023.106956.

[117] S. Sikiru, T. L. Oladosu, T. I. Amosa, S. Y. Kolawole, and H. Soleimani, “Recent advances and impact of phase change materials on solar energy: A comprehensive review,” *J. Energy Storage*, vol. 53, Sep. 2022, doi: 10.1016/J.EST.2022.105200.

[118] X. Li *et al.*, “Advanced Nanocomposite Phase Change Material Based on Calcium Chloride Hexahydrate with Aluminum Oxide Nanoparticles for Thermal Energy Storage,” *Energy and Fuels*, vol. 31, no. 6, pp. 6560–6567, 2017, doi: 10.1021/acs.energyfuels.7b00851.

[119] T. Zou *et al.*, “Preparation and performance of modified calcium chloride hexahydrate composite phase change material for air-conditioning cold storage,” *Int. J. Refrig.*, vol. 95, pp. 175–181, 2018, doi: 10.1016/j.ijrefrig.2018.08.001.

[120] M. Al-harahsheh, M. Abu-Arabi, H. Mousa, and Z. Alzghoul, “Solar desalination using solar still enhanced by external solar collector and PCM,” *Appl. Therm. Eng.*, vol. 128, pp.

1030–1040, Jan. 2018, doi: 10.1016/J.APPLTHERMALENG.2017.09.073.

[121] L. Kalapala and J. K. Devanuri, “Influence of operational and design parameters on the performance of a PCM based heat exchanger for thermal energy storage – A review,” *J. Energy Storage*, vol. 20, pp. 497–519, Dec. 2018, doi: 10.1016/J.EST.2018.10.024.

[122] K. Faraj, M. Khaled, J. Faraj, F. Hachem, and C. Castelain, “Phase change material thermal energy storage systems for cooling applications in buildings: A review,” *Renew. Sustain. Energy Rev.*, vol. 119, Mar. 2020, doi: 10.1016/J.RSER.2019.109579.

[123] J. R. Hirschey *et al.*, “Review of Low-Cost Organic and Inorganic Phase Change Materials with Phase Change Temperature between 0°C and 65°C,” *Int. High Perform. Build. Conf.*, p. 10, 2021, [Online]. Available: https://docs.lib.purdue.edu/ihpbc/389

[124] X. Li *et al.*, “Phase change behavior of latent heat storage media based on calcium chloride hexahydrate composites containing strontium chloride hexahydrate and oxidation expandable graphite,” *Appl. Therm. Eng.*, vol. 102, pp. 38–44, 2016, doi: 10.1016/j.applthermaleng.2016.03.098.

[125] N. Xie, Z. Huang, Z. Luo, X. Gao, Y. Fang, and Z. Zhang, “Inorganic Salt Hydrate for Thermal Energy Storage,” *Appl. Sci. 2017, Vol. 7, Page 1317*, vol. 7, no. 12, p. 1317, Dec. 2017, doi: 10.3390/APP7121317.

[126] X. Xu, Z. Dong, S. A. Memon, X. Bao, and H. Cui, “Preparation and Supercooling Modification of Salt Hydrate Phase Change Materials Based on CaCl2·2H2O/CaCl2,” *Mater. 2017, Vol. 10, Page 691*, vol. 10, no. 7, p. 691, Jun. 2017, doi: 10.3390/MA10070691.

[127] X. Xu, Z. Dong, S. A. Memon, X. Bao, and H. Cui, “Preparation and supercooling modification of salt hydrate phase change materials based on CaCl2·2H2O/CaCl2,” *Materials (Basel).*, vol. 10, no. 7, 2017, doi: 10.3390/ma10070691.

[128] X. Zhang *et al.*, “Calcium Chloride Hexahydrate/Diatomite/Paraffin as Composite Shape-Stabilized Phase-Change Material for Thermal Energy Storage,” *Energy and Fuels*, vol. 32, no. 1, pp. 916–921, 2018, doi: 10.1021/acs.energyfuels.7b02866.

[129] C. Li, M. Li, and Y. Li, “Tailored calcium chloride hexahydrate as a composite phase change material for cold storage,” *J. Energy Storage*, vol. 56, no. July, 2022, doi: 10.1016/j.est.2022.105798.

[130] J. Thakkar, N. Bowen, A. C. Chang, P. Horwath, M. J. Sobkowicz, and J. Kośny, "Optimization of Preparation Method, Nucleating Agent, and Stabilizers for Synthesizing Calcium Chloride Hexahydrate (CaCl2.6H2O) Phase Change Material," *Buildings*, vol. 12, no. 10, 2022, doi: 10.3390/buildings12101762.

[131] X. Xu, H. Cui, S. A. Memon, H. Yang, and W. Tang, "Development of novel composite PCM for thermal energy storage using CaCl 2 ·6H 2 O with graphene oxide and SrCl 2 ·6H 2 O," *Energy Build.*, vol. 156, pp. 163–172, 2017, doi: 10.1016/j.enbuild.2017.09.081.

[132] M. Li, Q. Wu, K. Song, S. Lee, Y. Qing, and Y. Wu, "Cellulose Nanoparticles: Structure − Morphology − Rheology Relationships," 2015, doi: 10.1021/acssuschemeng.5b00144.

[133] A. Naghdbishi, M. E. Yazdi, and G. Akbari, "Experimental investigation of the effect of multi-wall carbon nanotube – Water/glycol based nanofluids on a PVT system integrated with PCM-covered collector," *Appl. Therm. Eng.*, vol. 178, Sep. 2020, doi: 10.1016/J.APPLTHERMALENG.2020.115556.

[134] K. Huang, J. Li, X. Luan, L. Liu, Z. Yang, and C. Wang, "Effect of Graphene Oxide on Phase Change Materials Based on Disodium Hydrogen Phosphate Dodecahydrate for Thermal Storage," *ACS Omega*, vol. 5, no. 25, pp. 15210–15217, 2020, doi: 10.1021/acsomega.0c01184.

[135] T. Zou *et al.*, "Hydrophilic modification of expanded graphite to develop form-stable composite phase change material based on modified CaCl2·6H2O," *Energy*, vol. 190, Jan. 2020, doi: 10.1016/J.ENERGY.2019.116473.

[136] H. Cui, P. Wang, H. Yang, and T. Xu, "Design and preparation of salt hydrate/ graphene oxide@SiO2/ SiC composites for efficient solar thermal utilization," *Sol. Energy Mater. Sol. Cells*, vol. 236, Mar. 2022, doi: 10.1016/J.SOLMAT.2021.111524.

[137] W. Yang *et al.*, "Strong and Highly Conductive Graphene Composite Film Based on the Nanocellulose-Assisted Dispersion of Expanded Graphite and Incorporation of Poly(ethylene oxide)," *ACS Sustain. Chem. Eng.*, vol. 7, no. 5, pp. 5045–5056, 2019, doi: 10.1021/acssuschemeng.8b05850.

[138] S. Xu, W. Yu, M. Jing, R. Huang, Q. Zhang, and Q. Fu, "Largely Enhanced Stretching Sensitivity of Polyurethane/Carbon Nanotube Nanocomposites via Incorporation of

Cellulose Nanofiber," *J. Phys. Chem. C*, vol. 121, no. 4, pp. 2108–2117, 2017, doi: 10.1021/acs.jpcc.6b11783.

[139] S. Xu, W. Yu, X. Yao, Q. Zhang, and Q. Fu, "Nanocellulose-assisted dispersion of graphene to fabricate poly(vinyl alcohol)/graphene nanocomposite for humidity sensing," *Compos. Sci. Technol.*, vol. 131, pp. 67–76, Aug. 2016, doi: 10.1016/J.COMPSCITECH.2016.05.014.

[140] N. Kumar and D. Banerjee, "Characterization of Phase Change Materials (PCM) using T-History method," 2016, Accessed: Jun. 16, 2022. [Online]. Available: http://asmedigitalcollection.asme.org/HT/proceedings-pdf/HT2016/50329/V001T01A014/2441694/v001t01a014-ht2016-7310.pdf

[141] M. Goswami *et al.*, "Understanding supercooling mechanism in sodium sulfate decahydrate phase-change material," *J. Appl. Phys.*, vol. 129, no. 24, 2021, doi: 10.1063/5.0049512.

[142] S. E. Gustafsson, "Transient plane source techniques for thermal conductivity and thermal diffusivity measurements of solid materials," *Rev. Sci. Instrum.*, vol. 62, no. 3, pp. 797–804, 1991, doi: 10.1063/1.1142087.

[143] D. Qian, D. Fang, and Y. Xu, "You may also like In-situ growth of high-density ultrafine Ag 3 PO 4 nanoparticles on 3D TiO 2 hierarchical spheres for enhanced photocatalytic degradation of organic pollutants," *J. Phys. D. Appl. Phys.*.

[144] "ISO - ISO 22007-2:2022 - Plastics — Determination of thermal conductivity and thermal diffusivity — Part 2: Transient plane heat source (hot disc) method." https://www.iso.org/standard/81836.html (accessed Mar. 20, 2023).

[145] H. Feilchenfeld and S. Sarig, "Calcium Chloride Hexahydrate: A Phase-Changing Material for Energy Storage," *Ind. Eng. Chem. Prod. Res. Dev.*, vol. 24, no. 1, pp. 130–133, 1985, doi: 10.1021/i300017a024.

[146] M. Tortello *et al.*, "Effect of thermal annealing on the heat transfer properties of reduced graphite oxide flakes: A nanoscale characterization via scanning thermal microscopy," *Carbon N. Y.*, vol. 109, pp. 390–401, Nov. 2016, doi: 10.1016/J.CARBON.2016.08.017.

[147] S. Xu, W. Yu, X. Yao, Q. Zhang, and Q. Fu, "Nanocellulose-assisted dispersion of graphene to fabricate poly(vinyl alcohol)/graphene nanocomposite for humidity sensing,"

Compos. Sci. Technol., vol. 131, pp. 67–76, 2016, doi: 10.1016/j.compscitech.2016.05.014.

[148] Y. Li *et al.*, "Nanocellulose as green dispersant for two-dimensional energy materials," *Nano Energy*, vol. 13, pp. 346–354, 2015, doi: 10.1016/j.nanoen.2015.02.015.

[149] M. C. Morris *et al.*, *Standard X-Ray Diffraction Powder Patterns.* US Department of Commerce, National Bureau of Standards, 1982. doi: 10.1524/zkri.1970.131.1-6.159.

[150] N. Kumar and V. C. Srivastava, "Simple Synthesis of Large Graphene Oxide Sheets via Electrochemical Method Coupled with Oxidation Process," *ACS Omega*, vol. 3, no. 8, pp. 10233–10242, 2018, doi: 10.1021/acsomega.8b01283.

[151] K. Yuan, Y. Zhou, W. Sun, X. Fang, and Z. Zhang, "A polymer-coated calcium chloride hexahydrate/expanded graphite composite phase change material with enhanced thermal reliability and good applicability," *Compos. Sci. Technol.*, vol. 156, pp. 78–86, Mar. 2018, doi: 10.1016/J.COMPSCITECH.2017.12.021.

[152] J. Yang, E. Zhang, X. Li, Y. Zhang, J. Qu, and Z.-Z. Yu, "Cellulose/graphene aerogel supported phase change composites with high thermal conductivity and good shape stability for thermal energy storage," *Carbon N. Y.*, vol. 98, pp. 50–57, Mar. 2016, doi: 10.1016/J.CARBON.2015.10.082.

[153] O. Akamo, Damilola; Hirschey, Jason; Turnaoglu, Tugba; LaClair, Tim; Gluesenkamp, Kyle; Goswami, Monojoy; and Rios, "Salt Hydrate Eutectic Mixtures for Near Ambient Thermal Energy Storage Applications," *Int. Refrig. Air Cond. Conf. Pap. 2471*, 2022.

[154] B. Kalidasan, A. K. Pandey, R. Saidur, M. Samykano, and V. V Tyagi, "Nano additive enhanced salt hydrate phase change materials for thermal energy storage," *Int. Mater. Rev.*, pp. 1–44, Mar. 2022, doi: 10.1080/09506608.2022.2053774.

[155] N. Xie *et al.*, "Salt hydrate/expanded vermiculite composite as a form-stable phase change material for building energy storage," *Sol. Energy Mater. Sol. Cells*, vol. 189, no. July 2018, pp. 33–42, 2019, doi: 10.1016/j.solmat.2018.09.016.

[156] M. Li, H. Kao, Z. Wu, and J. Tan, "Study on preparation and thermal property of binary fatty acid and the binary fatty acids/diatomite composite phase change materials," *Appl. Energy*, vol. 88, no. 5, pp. 1606–1612, 2011, doi: 10.1016/j.apenergy.2010.11.001.

[157] Z. Rao, T. Xu, C. Liu, Z. Zheng, L. Liang, and K. Hong, "Experimental study on thermal

properties and thermal performance of eutectic hydrated salts/expanded perlite form-stable phase change materials for passive solar energy utilization," *Sol. Energy Mater. Sol. Cells*, vol. 188, no. August, pp. 6–17, 2018, doi: 10.1016/j.solmat.2018.08.012.

[158] Y. Liu and Y. Yang, "Preparation and thermal properties of Na2CO3·10H2O-Na2HPO4·12H2O eutectic hydrate salt as a novel phase change material for energy storage," *Appl. Therm. Eng.*, vol. 112, pp. 606–609, 2017, doi: 10.1016/j.applthermaleng.2016.10.146.

[159] Y. Watanabe and I. Hirasawa, "Eutectic Composition of a Salt Hydrate Mixture of Sodium Carbonate and Disodium Hydrogen Phosphate," *KAGAKU KOGAKU RONBUNSHU*, vol. 44, no. 3, pp. 207–216, 2018, doi: 10.1252/kakoronbunshu.44.207.

[160] P. M. de Wolff, "Technisch Physische Dienst, Delft, The Netherlands," *ICDD Grant-in-Aid*, 1957.

[161] M. R. Yazdani, R. Ajdary, A. Kankkunen, O. J. Rojas, and A. Seppälä, "Cellulose Nanofibrils Endow Phase-Change Polyethylene Glycol with Form Control and Solid-to-gel Transition for Thermal Energy Storage," *ACS Appl. Mater. Interfaces*, vol. 13, no. 5, pp. 6188–6200, 2021, doi: 10.1021/acsami.0c18623.

[162] Y. Fang *et al.*, "Form-stable Na2SO4·10H2O-Na2HPO4·12H2O eutectic/hydrophilic fumed silica composite phase change material with low supercooling and low thermal conductivity for indoor thermal comfort improvement," *Int. J. Energy Res.*, vol. 44, no. 4, pp. 3171–3182, Mar. 2020, doi: 10.1002/ER.5178.

APPENDICES

A. SUPPLEMENTARY DATA FOR CHAPTER 2

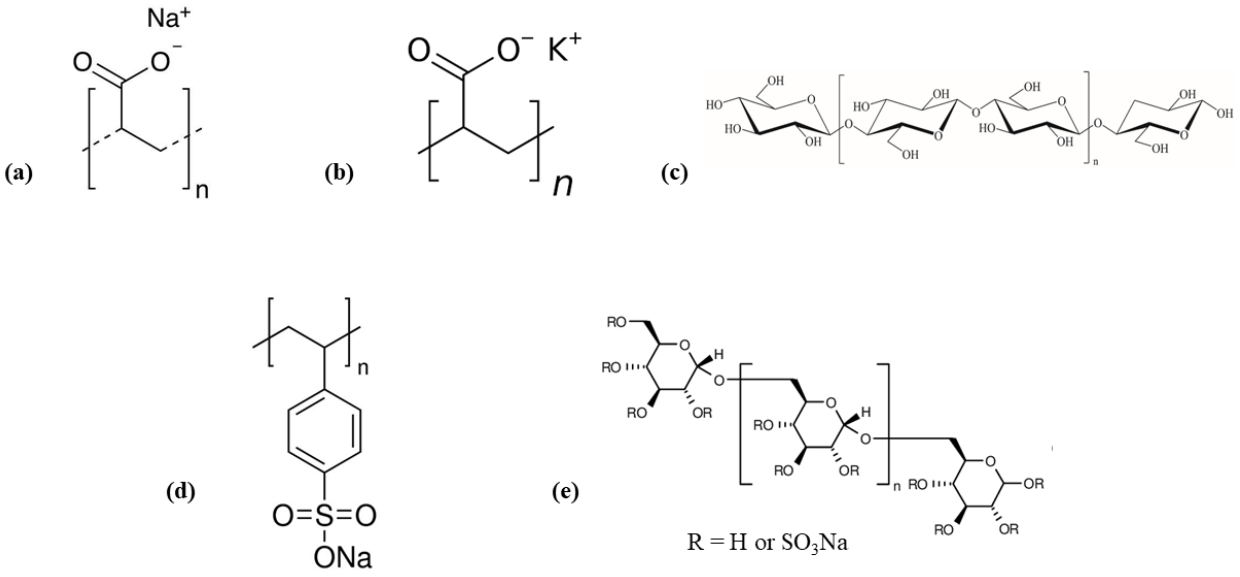


Figure A.1. Molecular structures of the additives used with SSD (a) Sodium polyacrylate (SPA) (b) Potassium polyacrylate (PPA) (c) Cellulose Nanofiber (CNF) (d) Poly(sodium 4-styrenesulfonate) (PSS) (e) Dextran sulfate sodium (DSS)

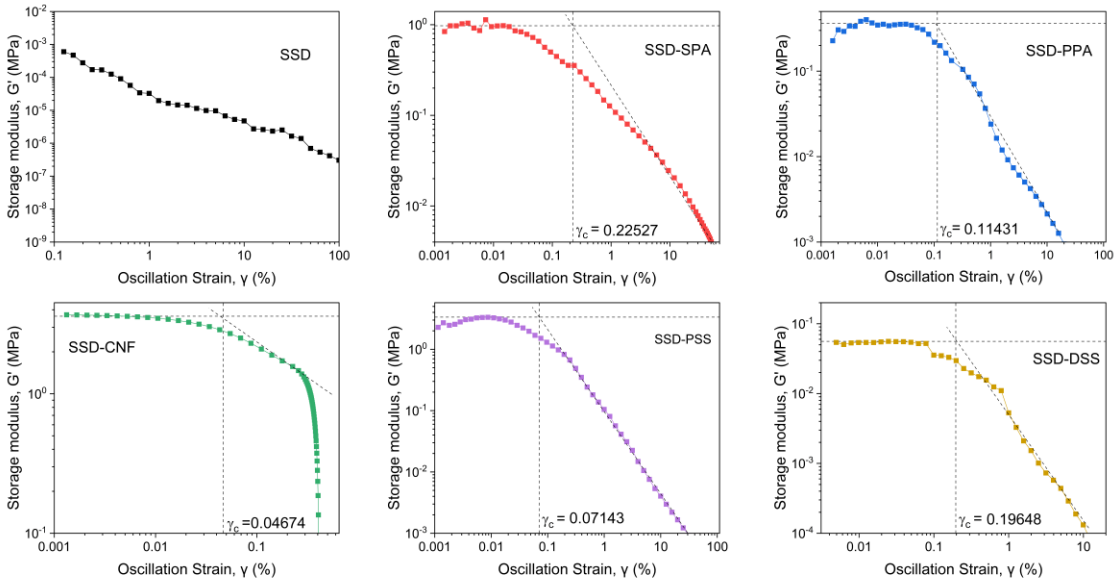


Figure A.2. Critical strain determination from the amplitude sweep data for pure SSD and SSD-based composites with various additives.

Table A.1. Flow test results of pure SSD, and SSD-based composites

Sample	Behavior	Flow Consistency Index, K ($Pa.s^{n-1}$)	Power law index, n
SSD	Newtonian	0.02	~1
SSD-SPA	Non-Newtonian	1120.60	0.607
SSD-PPA	Non-Newtonian	96.90	0.650
SSD-CNF	Non-Newtonian	1351.60	0.123
SSD-PSS	Non-Newtonian	79.49	0.790
SSD-DSS	Newtonian	1.10	~1

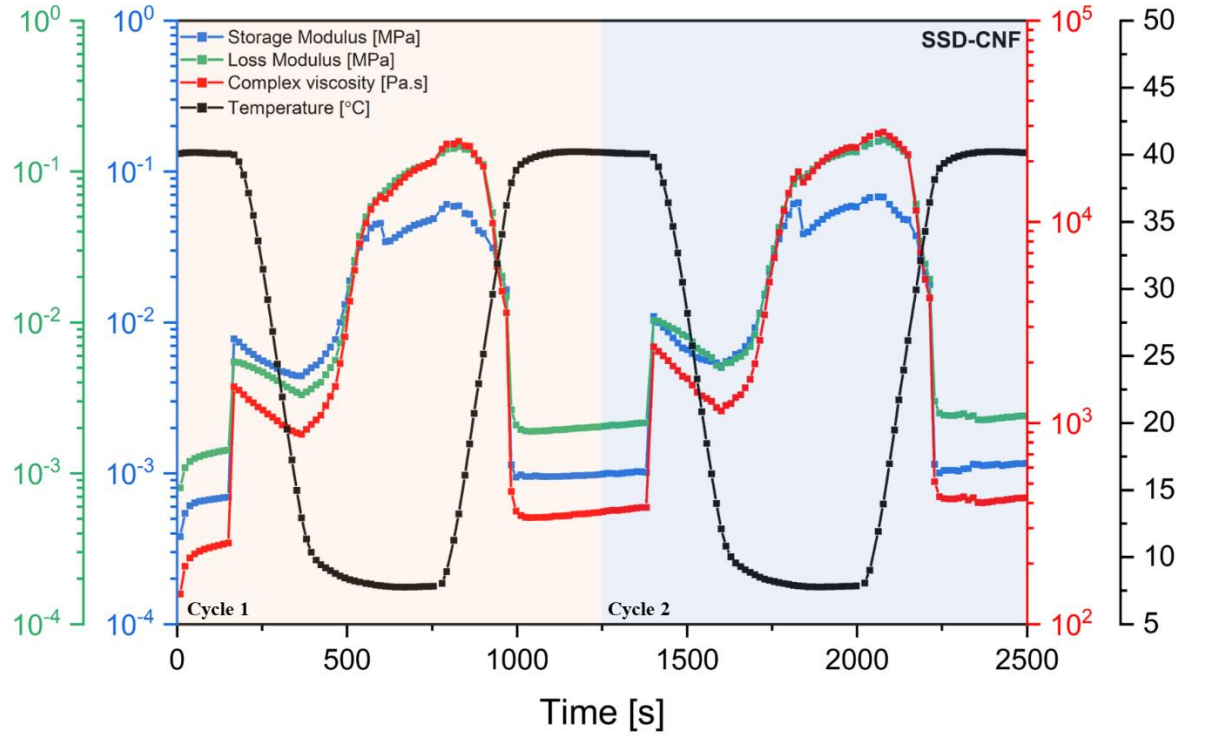


Figure A.3: Change in viscosity, storage, and loss moduli over the temperature range of 8─40 °C during 2 cycles for SSD-CNF.

B. SUPPLEMENTARY DATA FOR CHAPTER 3

B.1 Code for the rotational transformation of the DSS Molecules

```
% This code are used to do the rotational transformation for dextran sulfate sodium molecules
%
%x y z is the coordinates before rotation, and X Y Z represents the
%coordinates after rotation
%

%
%--http://en.wikipedia.org/wiki/Euler_angles
%--is the source I use to define the angles, i.e. alpha, beta, gamma
%

close all
clear all
alpha = random('uniform',0,360);
beta = random('uniform',0,360);
gamma = random('uniform',0,360);

alpha=alpha*pi/180;% alpha is the angle between the x-axis and the line of nodes.
beta=beta*pi/180; % beta is the angle between the z-axis and the Z-axis.
gamma=gamma*pi/180; % gama is the angle between the line of nodes and the X-axis.
%
% Az is the matrix represents the gamma rotation around the axis ' Z ' of the final reference frame
%
Az=[cos(gamma) sin(gamma) 0
   -sin(gamma) cos(gamma) 0
   0       0 1];
%
% Ax represents the beta rotation around an intermediate ' x ' axis which is the "line of nodes"
%
Ax=[1 0 0
   0 cos(beta) sin(beta)
   0 -sin(beta) cos(beta)];
%
%Ay the alpha rotation around the axis ' z ' of the original reference frame
%
Ay=[cos(alpha)  sin(alpha) 0
   -sin(alpha) cos(alpha) 0
   0 0 1];

[num,txt,raw]=xlsread('dextran1.xlsx');

[m,n]=size(num);
n=m;  % Number of data point

for i=1:n
xcoord  = num(i,1);
ycoord  = num(i,2);
zcoord  = num(i,3);
end
```

```
B = [num(:,1), num(:,2), num(:,3)];
ntot=351; % total number of atoms in 2nm-tetrahedron

%
%B is the matrix contains all the pt coordinates
%

% calculate average position
Bavg = zeros(3,1);
for i = 1:1:3
   for j = 1:1:ntot
   Bavg(i) = Bavg(i) + B(j,i);
   end
   Bavg(i) = Bavg(i)/ntot;
end

%Shift atoms by average position
Btemp = zeros(ntot,3);
for i = 1:1:3
   for j = 1:1:ntot
    Btemp(j,i) =  B(j,i) - Bavg(i);
   end
end

Btemp2 = zeros(ntot,3);
Btemp2=Az*Ax*Ay*Btemp'; %Euler transformation
% shift back
Btemp2 = Btemp2';
Bfinal = zeros(ntot,3);
for i = 1:1:3
   for j = 1:1:ntot
    Bfinal(j,i) =  Btemp2(j,i) + Bavg(i);
   end
end
C=Bfinal;
%
% write results
%
xlswrite('newdextran1.xlsx',C);

%fid = fopen('dextran1new.xlsx','w');
%fprintf(fid,'%6i \n \n',ntot);
%for i = 1:1:ntot
%   fprintf(1,'%2s %23.15e %23.15e %23.15e \n',cname,C(i,1:3))
  %fprintf(fid,'%2s %23.15f %23.15f %23.15f \n', C(i,1:3));
%end
%fclose(fid);
```

B.2 Code for the confirming the random configuration of the DSS Molecules

```
filename = 'dextranrandom755';
data = readmatrix([filename, '.xlsx']);
N = 351; I = 1:N;
Theta = zeros(175,1);
Phi = zeros(175, 1);
R = zeros(175,1);
for n = 1:175
   molecule = data(I + (n-1)*N, :);
   D = Distance(molecule, N);
   D = triu(D, 1); % to remove duplicates and distance between an atom and itself
   [R(n), indx] = max(D(:));
   [i, j] = ind2sub([N, N], indx);
   v = diff(molecule([i, j], :));
   Theta(n) = atan2(v(2), v(1));
   Phi(n) = atan2(v(3), hypot(v(2), v(1)));
end

subplot(1,3,1); hist(R, 20);
title('r distribution', 'fontsize',14)
xlabel('r', 'fontsize',14)
ylabel('Count', 'fontsize',14)

subplot(1,3,2); hist(Theta, 20);
title('\theta distribution', 'fontsize',14)
xlabel('\theta', 'fontsize',14)
ylabel('Count', 'fontsize',14)

subplot(1,3,3); hist(Phi, 20);
title('\phi distribution', 'fontsize',14)
xlabel('\phi', 'fontsize',14)
ylabel('Count', 'fontsize',14)

writematrix([R, Theta, Phi], [filename, 'Sphere.xlsx']);


function D = Distance(pts, N)
   D = zeros(N);
   for i = 1:N
      D(i, :) = arrayfun(@(j)norm(diff(pts([i, j], :))),1:N);
   end
end
```

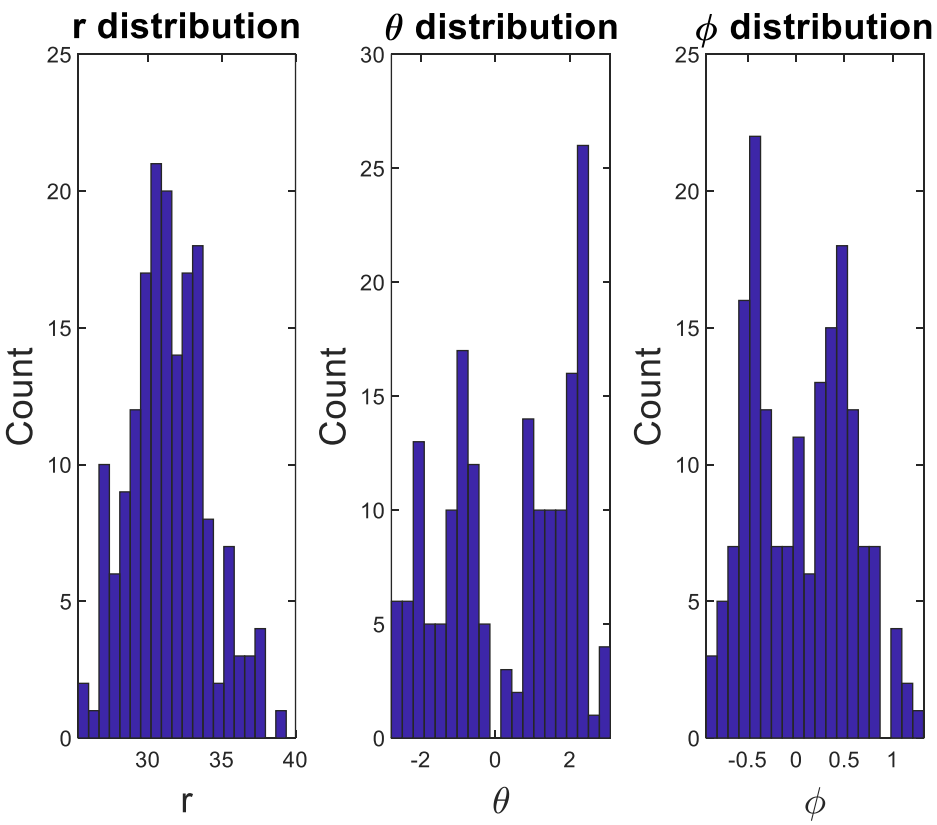


Figure B.1: Distribution of the position of DSS molecules in polar coordinate

B.3 Code for calculating interfacial thickness in the combined system

```
import numpy as np
import os
import matplotlib.pyplot as plt


#- Read lammp output file into numpy array

file = 'dump_composite.lammpstrj'
n_times = 1350 #Number of time steps saved
n_atoms = 137201 #Number of atom and header lines
offset = 137201 + 9 #Number of atom and header lines
# Load coordinates from simulation trajectory file (assumed to be in XYZ format)

with open(file, 'r') as f:
    lines = f.readlines()
    atoms = np.zeros((n_times, n_atoms, 5))
    for i in range(n_times):
        for j, line in enumerate(lines[(9 + (offset*i)):(n_atoms + 9 + (offset*i))]):
            atoms[i, j] = np.array([list(map(float, line.split()))])

print(atoms)

#- Extract oxygen atoms

atom_ID = 9
oxygen = np.zeros((n_times, atoms[0, atoms[0, :, 1] == atom_ID, :].shape[0], 5))
for i in range(n_times):
    oxygen[i] = atoms[i, atoms[i, :, 1] == atom_ID, :]

#- Extract coordinates for oxygen atoms

x_width = 88.6776
y_width = 94.0445
z_width = 202.567

coords = oxygen[:, :, 2:] #-Extract atom coordinates
#- Scale x, y, z coordinates
coords[:, :, 0] = coords[:, :, 0]*x_width
coords[:, :, 1] = coords[:, :, 1]*y_width
coords[:, :, 2] = coords[:, :, 2]*z_width
```

```
# Define the region of interest (ROI) for interfacial analysis
x_min, x_max = 0, 88.6776  # ROI slab width along x-axis
y_min, y_max = 0, 94.0445  # ROI slab width along y-axis
z_min, z_max = 0, 202.567  # ROI slab width along z-axis

# Extract coordinates of atoms within the ROI

roi_coords = []
for i, snapshot in enumerate(coords):
    x, y, z = snapshot[:, 0], snapshot[:, 1], snapshot[:, 2]
    mask = np.logical_and(np.logical_and(x >= x_min, x <= x_max), np.logical_and(y >= y_min,
y <= y_max), np.logical_and(z >= z_min, z <= z_max))
    roi_coords.append(snapshot[mask])

# Calculate the density profile along z-axis for each snapshot in the ROI
def calculate_density_profile(n_bin, density=True):
    bin_edges = np.linspace(0, (z_max - z_min), n_bin + 1)
    bin_centers = (bin_edges[1:] + bin_edges[:-1]) / 2
    densities = np.zeros((len(roi_coords), n_bin))
    for i, snapshot in enumerate(roi_coords):
        z = snapshot[:, 2]
        densities[i], _ = np.histogram(z, bins=bin_edges, density=density)


    # Calculate the mean density profile and interfacial width
    mean_density = np.mean(densities, axis=0)
    threshold = 0.5*(np.max(mean_density) + np.min(mean_density))  # Define threshold for
interface
    interface_edges = bin_centers[mean_density >= threshold]
    interfacial_width = interface_edges[-1] - interface_edges[0]

    print(f"Interfacial width (bin: {n_bin}) = {interfacial_width:.2f} Angstroms")

    return(bin_centers, densities)


n_bin = 100
bin_centers, densities = calculate_density_profile(n_bin) #For # of bins = 50
plt.plot(bin_centers, densities.mean(axis=0), '-o')
plt.title(f'# of bins = {n_bin}')
plt.xlabel('Position (z direction)')
plt.ylabel('Density')
plt.show()
```

```
from scipy.optimize import curve_fit
n_bin = 100
bin_centers, densities = calculate_density_profile(n_bin, density=False)

frequency = densities.mean(axis=0)
position = bin_centers
def func(x, rho, z0, d): return rho*(1 - np.tanh(2*(x - z0)/d))
res = curve_fit(func, position, frequency, bounds=([0, 0, 0], [1000, z_width, z_width]))
popt = res[0]
frequency_hat = func(position, popt[0], popt[1], popt[2])
print(f'The density, rho = {popt[0]}\n' +
    f'The position of the Gibbs dividing surface, Z0 = {popt[1]}\n' +
    f'The the adjustable parameter related to the interfacial thickness, d = {popt[2]}')

plt.plot(position, frequency, 'o')
plt.plot(position, frequency_hat, '-', c='red')
plt.xlabel('Position (z direction)')
plt.ylabel('Frequency')
plt.show()
print(position)
print(frequency)
print(frequency_hat)

from scipy.optimize import curve_fit

n_bin = 100
bin_centers, densities = calculate_density_profile(n_bin)

density = densities.mean(axis=0)
position = bin_centers
def func(x, rho, z0, d): return rho*(1 - np.tanh(2*(x - z0)/d))
res = curve_fit(func, position, density, bounds=([0, 0, 0], [1000, z_width, z_width]))

popt = res[0]
density_hat = func(position, popt[0], popt[1], popt[2])
print(f'The density, rho = {popt[0]}\n' +
    f'the position of the Gibbs dividing surface, Z0 = {popt[1]}\n' +
    f'The adjustable parameter related to the interfacial thickness, d = {popt[2]}')

plt.plot(position, density, 'o')
plt.plot(position, density_hat, '-', c='green')
plt.xlabel('Position (z direction)')
plt.ylabel('Density')
plt.show()
print(density)
```

```
if False: #Do not run every time
    n_bins = (20, 50, 100, 200, 500, 1000)    # Number of bins for density profile
    for n_bin in n_bins:
        bin_centers, densities = calculate_density_profile(n_bin)

        plt.plot(bin_centers, densities.mean(axis=0), '-o')
        plt.title(f'# of bins = {n_bin:04d}')
        plt.xlim(0, 80)
        plt.xticks(np.linspace(0, 80, 5))
        plt.xlabel('Position (z direction)')
        plt.ylabel('Density')
        plt.ylim(0, 0.03)
        plt.yticks(np.linspace(0, 0.03, 5))
        plt.savefig(f'{n_bin:03d}.png')
        plt.close()
```

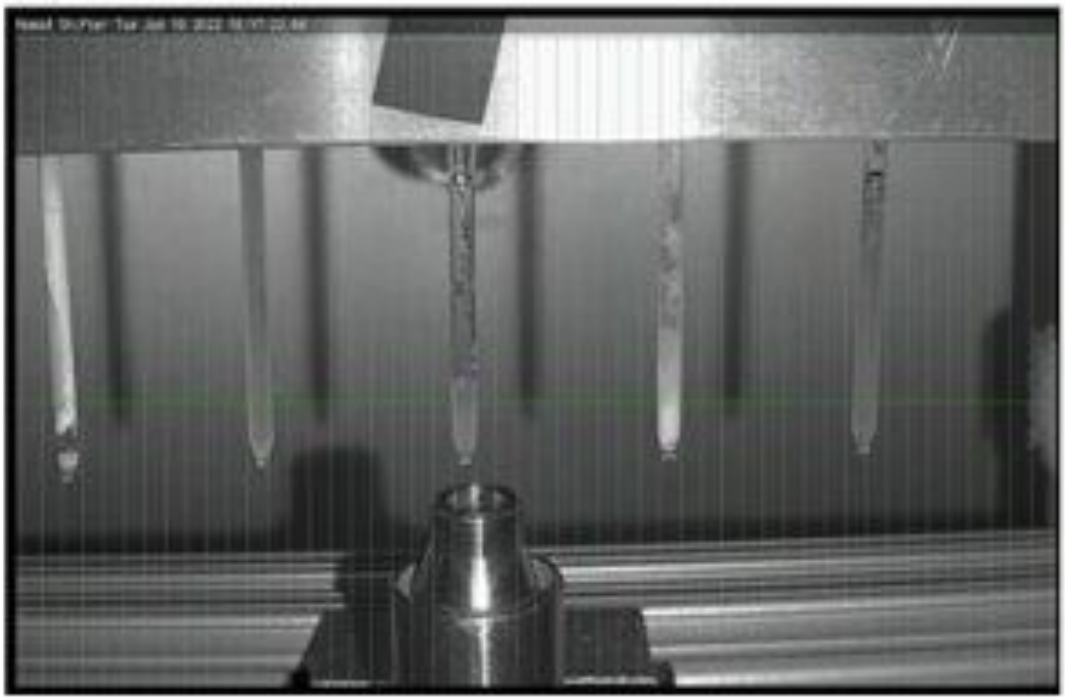


Figure B.2: PCM samples under neutron scan for acquisition of PDF data. Green beam is the neutron line that passes through the samples.

AUTHOR'S LIST OF PUBLICATIONS

1. Li, Y; Kumar, N.; Hirschey, J.; **Akamo, DO**.; Li, K.; Turnaoglu, T.; Goswami M.; Rios O.; LaClair, TJ.; Graham, S.; Gluesenkamp, KR. (2022). Stable Salt Hydrate-based Thermal Energy Storage Materials. Composites Part B: Engineering. https://doi.org/10.1016/j.compositesb.2022.109621
2. Goswami, M.; Kumar, N. Li, Y.; Hirschey, J.; LaClair, TJ; **Akamo, DO**.; Sultan, S.; Rios, O.; Gluesenkamp, KR.; Graham, S. (2021). Understanding supercooling mechanism in sodium sulfate decahydrate phase-change material. Journal of Applied Physics, 129(24), 245109. https://doi.org/10.1063/5.0049512
3. Goswami, M.; Kumar, N.; Li, Y.; Rios, O.; **Akamo, DO**.; Hirschey, J.; LaClair, TJ; Gluesenkamp, KR. (2021). Comparison of water nanodroplet properties on different graphite-based substrates. AIP Advances 11, 035009. https://doi.org/10.1063/5.0042414
4. **Akamo, DO**.; Ijaola, A.O.; George, T.T.; Page,K.; Keffer,D.J.; Li, Y.; Goswami, M.; LaClair, T.J.; Gluesenkamp, K.; Rios, O. (2022). Bibliometric review and recent advances in total scattering pair distribution function analysis: 21years in retrospect, European Journal of Materials, https://doi.org/10.1080/26889277.2022.2150897
5. Hirschey, J.; Goswami, M.; **Akamo, DO**.; Kumar, N.; Li, Y.; LaClair, T.J.; Gluesenkamp, K.R.; Graham, S. Effect of expanded graphite on the thermal conductivity of sodium sulfate decahydrate (Na2SO4·10H2O) phase change composites, Journal of Energy Storage, Volume 52, Part B,2022,104949., https://doi.org/10.1016/j.est.2022.104949.
6. Ijaola, A.O.; **Akamo, DO.**; Damiri, F.; Akisin, C.J.; Bamidele, E.A.; Ajiboye, E.G.; Berrada, M.; Onyenokwe, V.O.; Yang, S.; Asmatulu, E. (2022). Polymeric biomaterials for wound healing applications: a comprehensive review, Journal of Biomaterials Science, Polymer Edition, 33:15, 1998-2050,
7. **Akamo, DO**.; Hirschey, J.; Turnaoglu, T.; LaClair, T.; Gluesenkamp, KR.; Goswami, M.; Rios, O.; Salt Hydrate Eutectic Mixtures for Near-ambient Thermal Energy Storage Applications. 19th International Refrigeration and Air Conditioning Conference at Purdue, July 10 - 14, 2022

8. Ijaola, AO.; **Akamo, DO.**; Damiri, F.; Akisin, CJ.; Bamidele, EA.; Ajiboye, EG.; Berrada, M.; Onyenokwe, VO.; Yang, S.; Asmatulu, E. Polymeric Biomaterials for Wound-Healing Applications: A Comprehensive Review. Journal of biomaterials science:polymer
9. George T.; Obilana, A.; Oyenihi, A.; Obilana, A.; **Akamo, DO.**; Awika, J.; Trends and progress in sorghum research over two decades, and implications for global food security, South African Journal of Botany, Volume 151, Part A, 2022, Pages 960-969. https://doi.org/10.1016/j.sajb.2022.11.025.
10. Sultan, S.; Turnaoglu, T.; **Akamo, DO.**; Hirschey, J.; Laclair, T.J.; Liu, X.; Gluesenkamp, K.R., "PCM Material Selection for Heat Pump Integrated with Thermal Energy Storage for Demand Response in Residential Buildings" (2022). International High Performance Buildings Conference. Paper 427. https://docs.lib.purdue.edu/ihpbc/427
11. Damiri, F.; Andra, S.; Kommineni, N.; Balu, S.K.; Bulusu, R.; Boseila, A.A.; **Akamo, DO.**; Ahmad, Z.; Khan, F.S.; Rahman, M.H.; Berrada, M.; Cavalu, S. Recent Advances in Adsorptive Nanocomposite Membranes for Heavy Metals Ion Removal from Contaminated Water: A Comprehensive Review. Materials 2022, 15, 5392. https://doi.org/10.3390/ma15155392
12. Ayodele, DT., Ogunbiyi, OD., **Akamo, DO**., Otun, KO., Akinpelu,DA., Adegoke, JA., Fapojuwo, DP., Oladoye, PO. Factors affecting biohydrogen production: Overview and perspectives, International Journal of Hydrogen Energy, 2023, https://doi.org/10.1016/j.ijhydene.2023.04.001.

VITA

Damilola Akamo was born in Lagos, Nigeria. He pursued and earned a B.S. in Mechanical Engineering from Obafemi Awolowo University, Ile Ife Nigeria, and a M.S. in Material Science and Engineering from the University of Tennessee. He is currently pursuing a Ph.D. in Energy Science and Engineering at the Bredesen Center, University of Tennessee where he is working on computational materials science for thermal energy storage. He was awarded the Chancellor's citation for extraordinary professional promise in 2020.

Damilola's research interests focus on the understanding of the processing-structure-property-performance relationships of materials relevant to the generation, conversion, and storage of renewable energy. He currently works with the Building Technologies Research and Integration Center at Oak Ridge National Laboratory to develop a stable, low-cost, high thermal conductivity phase change material (PCM) for thermal energy storage. The work comprises synthesis and advanced material characterization techniques such as neutron scattering and molecular dynamics simulation to explore PCMs structure-property-performance relationships and their use in energy systems.